Modeling the Electrical Stimulation of Peripheral Vestibular Nerves

by

Ketul M. Parikh

S.B. Electrical Engineering and Computer Science, June 2005

Submitted to the Department of Electrical
Engineering and Computer Science
in partial fulfillment of the requirements for the degree of

Master of Engineering
in Electrical Engineering and Computer Science
at the
MASSACHUSETTS INSTITUTE OF TECHNOLOGY
September 2006

Author .....
Department of Electrical Engineering and Computer Science
August 22, 2006

Certified by .....
Marc S. Weinberg, PhD.
Laboratory Technical Staff, Charles Stark Draper Laboratory, Inc.
Thesis Supervisor

Certified by .....
Dennis M. Freeman, PhD.
Associate Professor of Electrical Engineering
Thesis Supervisor

Accepted by .....
Arthur C. Smith, PhD.
Chairman, Department Committee on Graduate Students

Modeling the Electrical Stimulation of Peripheral Vestibular Nerves

by

Ketul M. Parikh

Submitted to the Department of Electrical
Engineering and Computer Science
on August 22, 2006, in partial fulfillment of the
requirements for the degree of

Master of Engineering
in Electrical Engineering and Computer Science

Abstract

The research conducted for this thesis investigated the theoretical placement of electrodes for a proposed implantable vestibular prosthesis to aid patients suffering from balance related disorders. The most likely sites of stimulation for the first-generation of such a device are the peripheral nerves responsible for transmitting rotational information to the brain. Although stimulation of such nerves has been performed in human and animal patients, little is known about the mechanisms responsible for the eliciting nerve responses.

Models of the inferior and superior divisions of peripheral vestibular nerve were created to characterize the stimulus threshold behavior across the parameters of fiber diameter and location within the nerve. Current-distance relations were derived for nerve fibers excited by six commonly used electrode configurations. The threshold relations were used as a guide to determine the electrode configuration and location best-suited to stimulate the inferior vestibular nerve and selectively stimulate the branches of the superior vestibular nerve. The criteria used determine optimal placement included minimum current thresholds, configuration simplicity, and distance to the electrode. For the inferior nerve case, a cathodal stimulus located at a distance of $100\,\mu m$ or $200\,\mu m$ from the nerve and driven with a stimulus current of $56\,\mu A$ or $76\,\mu A$ was recommended.

For the superior vestibular nerve case we were interested in selectively stimulating each branch, imposing a further criteria to maximize the threshold ratio between stimulation of the respective branches. A transverse dipole electrode configurations was suggested that allowed selective stimulation of either branch. The configuration included a cathode located 300m from Branch 1 and an anode centrally located between both branches. When driven with a cathodal stimulus of strength $51\,\mu A$, only Branch I was excited, while driving both electrodes with a magnitude of $106\,\mu A$ excited only Branch II. The proximity to the facial nerve was considered in the choices

of configuration and placement, however it was inconclusive whether or not the facial nerve would fire with the suggested electrode configurations and stimuli.

Thesis Supervisor: Marc S. Weinberg, PhD.
Title: Laboratory Technical Staff, Charles Stark Draper Laboratory, Inc.

Thesis Supervisor: Dennis M. Freeman, PhD.
Title: Associate Professor of Electrical Engineering

Acknowledgment I

I would first like to thank my thesis advisor, Marc Weinberg, for giving me the opportunity to work on such an exciting project. Marc took me on as a Draper Fellow without a predefined thesis project and gave me the opportunity to define the scope and direction of my research. He gave me room to grow as an engineer, but was always there to offer help at the right time. Marc's warm and friendly personality made the project very rewarding and enjoyable, and I am thankful to have had the opportunity to work with him.

I would also like to thank Denny Freeman for his guidance and advice over the past year. He took an interest in my project and was always available to discuss ideas and offer insightful comments. It was Denny's class that first introduced me to this area of research, and I thank him for sparking my interest in the field.

This thesis marks the end of a wonderful academic experience from which I have matured intellectually, professionally, and personally. I am sincerely grateful to the teachers, professors, and mentors that have enriched my experiences and broadened my view of the world.

Most importantly, I would like to thank my parents and brother for their endless love and support. They instilled in me the drive to work hard and be successful in all my endeavors. My achievements would not have been possible without their encouragement and the grace of God.

Acknowledgment II

This thesis was prepared at The Charles Stark Draper Laboratory, Inc., under a grant from the National Institutes of Health (NIH NIDCD R01 DC6201).

Publication of this thesis does not constitute approval by Draper or the sponsoring agency of the findings or conclusions contained herein. It is published for the exchange and stimulation of ideas.

_____

(Author, Ketul M. Parikh)

For My Parents

THIS PAGE INTENTIONALLY LEFT BLANK

Contents

THIS PAGE INTENTIONALLY LEFT BLANK

List of Figures

THIS PAGE INTENTIONALLY LEFT BLANK

List of Tables

THIS PAGE INTENTIONALLY LEFT BLANK

Chapter 1

Introduction

The inner-ear's vestibular system controls the body's sense of movement and balance by providing motion cues for visual stabilization, standing and walking. Each inner-ear senses angular motion and linear acceleration summed with gravity in three dimensions, allowing the central nervous system (CNS) to estimate motion in six degrees of freedom [1]. Disease, injury, or age may lead to malfunction in the inner-ear or part of the CNS responsible for estimating motion, resulting in partial or total loss of self-motion information. People suffering from vestibular disorders are forced to rely on alternate motion cues from vision or proprioception.[1] However, the reduction of motion cues can produce symptoms that reduce a person's ability to walk or stand, such as blurred vision and dizziness. These symptoms greatly increase one's probability of falling, especially in elderly patients [2], and may in turn lead to death or serious bodily injury such as hip fracture. In fact, 25% of elederly patients who undergo a hip replacement after a fall die within 6 months of the surgery; of those who survive, 50% lose their ability to walk [3]. A balance prosthesis may be effective in the prevention of falls.

Forty percent of the American population (90 million people) will seek medical attention for dizziness at least once in their lifetime, and an estimated two million Americans currently suffer from balance related disorders and dizziness induced im-

[1]Proprioception is sense of position and motion through stimuli originating from receptors in joints, tendons, and muscles.

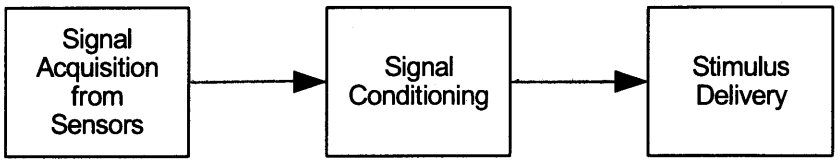

Figure 1-1: Vestibular Prosthesis Modules

pairments [3]. There exists a clear need for a prosthesis to aid the balance impaired, targeted at improving postural stability. Such a device could serve as a temporary aid for patients recovering from ablative inner-ear surgery, or a permanent prosthesis for the elderly and patients diagnosed with unilateral or bilateral vestibulopathies [2, 4].

1.1 Problem Domain

The basic functions of a vestibular prosthesis can be summarized in Figure 1-1. Position and motion information gathered by sensors mounted on or embedded within the body must be appropriately conditioned before a stimulus can be delivered to the body. The engineering considerations for each module are dictated by the approach taken to design the prosthesis [2]. Current investigations into vestibular prostheses are centered on two fronts: noninvasive prostheses based upon sensory substitution [2, 5, 6, 7] and implantable prostheses that directly stimulate vestibular nerves in animals [8, 9, 10]. While prostheses based upon sensory substitution have the advantage of being noninvasive, they suffer from limited bandwidth that only allows for the transmission of body tilt (position and magnitude) information. A vestibular prosthesis that most resembles the human vestibular system will likely directly stimulate vestibular nerves; the higher bandwidth available will likely allow the transmission of motion and position information in all six degrees-of-freedom.

The research conducted for this thesis is concerned with implantable vestibular prostheses. It is conceivable that a vestibular prosthesis could conceptually resemble a similar neural prosthesis, namely the cochlear implant. The vestibular prosthesis

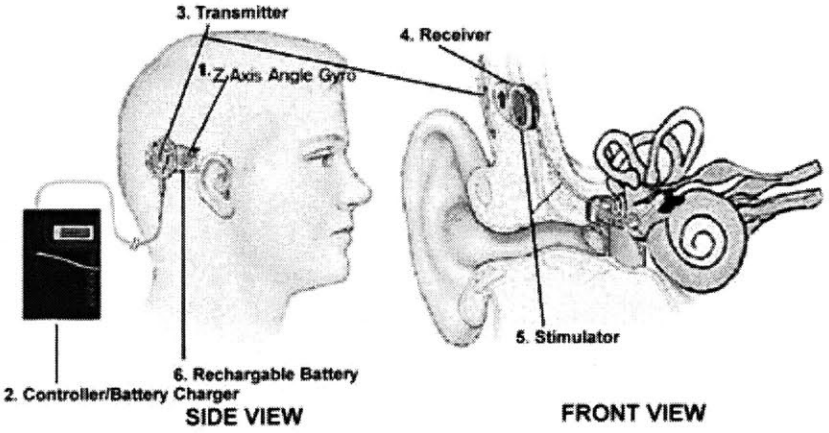

Figure 1-2: Rendition of a Single Degree-of-Freedom Vestibular Implant [11], Adapted: Shown is a yaw-rate gyroscope **(1)** attached externally to the temporal bone. The sensor is connected to an external pack **(2)** responsible for powering the sensor and conditioning the rate signal into a stimulus waveform. The stimulus waveform is delivered through a transcutaneous link (transmitter **(3)** and implanted receiver **(4)**) and applied to the nerves via a current stimulator **(5)**.

would acquire and process signals of motion and position rather than auditory signals. The conditioned signals would then be used as stimuli to electrically excite the nerves of the vestibular system. A rendition of a single degree-of-freedom prosthesis is shown in Figure 1-2.

The engineering and biomedical issues related to vestibular prosthesis design have been the focus of recent investigations. Wall *et al* approach the topic in the form of a white paper [2], theoretically addressing issues ranging from hardware design to stimulus coding strategies. Shkel and his collaborators focus on component miniaturization and hardware integration [11, 12, 13], while Merfeld *et al* have been conducting tests with vestibular prostheses that directly stimulate animal vestibular nerves [8, 9, 10].

The key question of electrode placement has, to date, been left unanswered. The research conducted as part of this thesis aims to quantitatively address the question of *in vivo* placement of implanted electrodes for a proposed human vestibular prosthesis. In particular, the study focuses on the theoretical placement of electrodes near the peripheral vestibular nerves responsible for transmitting rotational motion

information to the brain. The techniques used for simulation are well established and have been adapted from electrode placement research conducted for cochlear implants and functional electrical stimulation (FES) devices. Work on electrode placement in the vestibular domain is novel and not present in literature.

1.2 Thesis Goals

The research conducted as part of this thesis takes a theoretical approach, using modeling and simulation to address the electrical stimulation of vestibular nerves. We wish to create a model representing the peripheral vestibular nerves as they exist *in vivo* to analyze their excitation behavior. In particular, we seek to model the inferior and superior divisions of the peripheral vestibular nerve, prior to innervation of the sensory end-organs. These are the likely stimulation sites for first attempts at a human vestibular prosthesis.

Using the model, we wish to characterize the threshold relations of the nerve fibers when stimulated extracellularly from different electrode configurations. Based upon these relations we wish to suggest an ideal, or best-case, electrode configuration and placement location for each division of the vestibular nerve. Our primary metric for choosing this configuration will be electrode effectiveness, that is a configuration able to excite the nerve with a *minimum* amount of stimulus current. We also seek a configuration capable of selectively stimulating one of the branches of the superior vestibular nerve while not stimulating the other.

1.3 Thesis Overview

The body of the thesis is organized into five chapters. Chapter 2 describes relevant background of the vestibular system, particularly highlighting the structure and function of the peripheral vestibular nerves. Chapter 3 describes the theory and methods used in the simulation studies and focuses on the volume conductor and biophysical models employed. The simulation results are presented and discussed in Chapter 4,

and concluding remarks as well as recommendations for future work are presented in Chapter 5.

THIS PAGE INTENTIONALLY LEFT BLANK

Chapter 2

Background

2.1 The Vestibular System

The vestibular system detects position and motion of the head in space by integrating information from peripheral sensors located in the inner ear. Unlike our other senses (taste, smell, hearing, sight, or touch), the information gathered by the vestibular system is not prominent in our active consciousness. Although we are not normally aware of the sensory information, it is essential to coordination of motor reflexes, stabilizing eye movements, and maintaining posture. Awareness of the vestibular system often occurs when the system fails, producing sensations of dizziness and nausea that are quite perceptible [14].

2.1.1 Anatomy

Sense Organs

The peripheral vestibular organs are located in the inner ear on either side of the head as seen in Figure 2-1. The inner ear is comprised of two principal parts, namely the bony labyrinth and membranous labyrinth. The bony labyrinth consists of a series of cavities in the temporal bone that house the vestibular and auditory sense organs of the membranous labyrinth. The vestibular division of the membranous labyrinth includes the paired sensory organs of the semicircular canals and the otolith

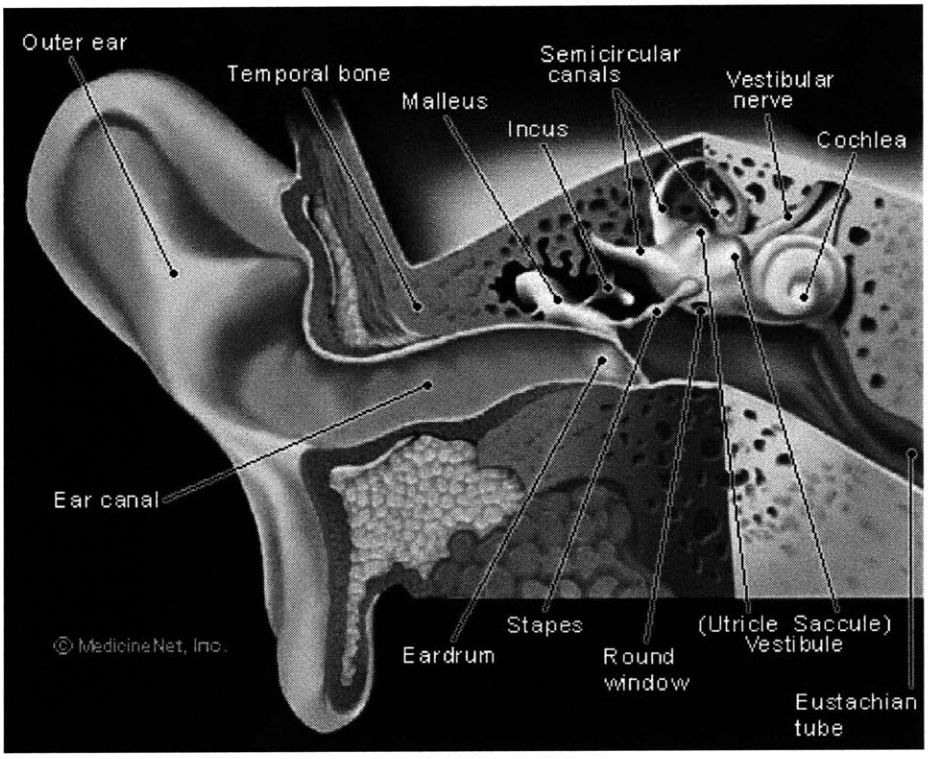

Figure 2-1: Cross-Section of the Temporal Bone

organs. The receptor cells in each of these organs respond to different aspects of head acceleration to detect both motion and a sense of position. Acceleration is perceived through the inertial displacement of a fluid termed endolymph that fills the membranous labyrinth. The endolymphatic fluid, with a high potassium and low sodium ion concentration, resembles intracellular fluid. Perilymph, a fluid resembling extracellular fluids, surrounds the membranous labyrinth and provides a barrier to the bony labyrinth [14, 15, 16].

The semicircular canals (SCCs) are a set of three directionally sensitive and nearly orthogonal ducts that detect angular acceleration (Figure 2-2). As a consequence of their mutually perpendicular orientation in three-dimensional space, they detect angular acceleration of the head in three different planes. The ampullated portion of the membranous labyrinth of each canal houses a crista, an end-organ containing specialized hair cells that transduce mechanical sheering forces from the endolymph into neural impulses. As seen in Figure 2-3, the hair cells of the ampullary nerve

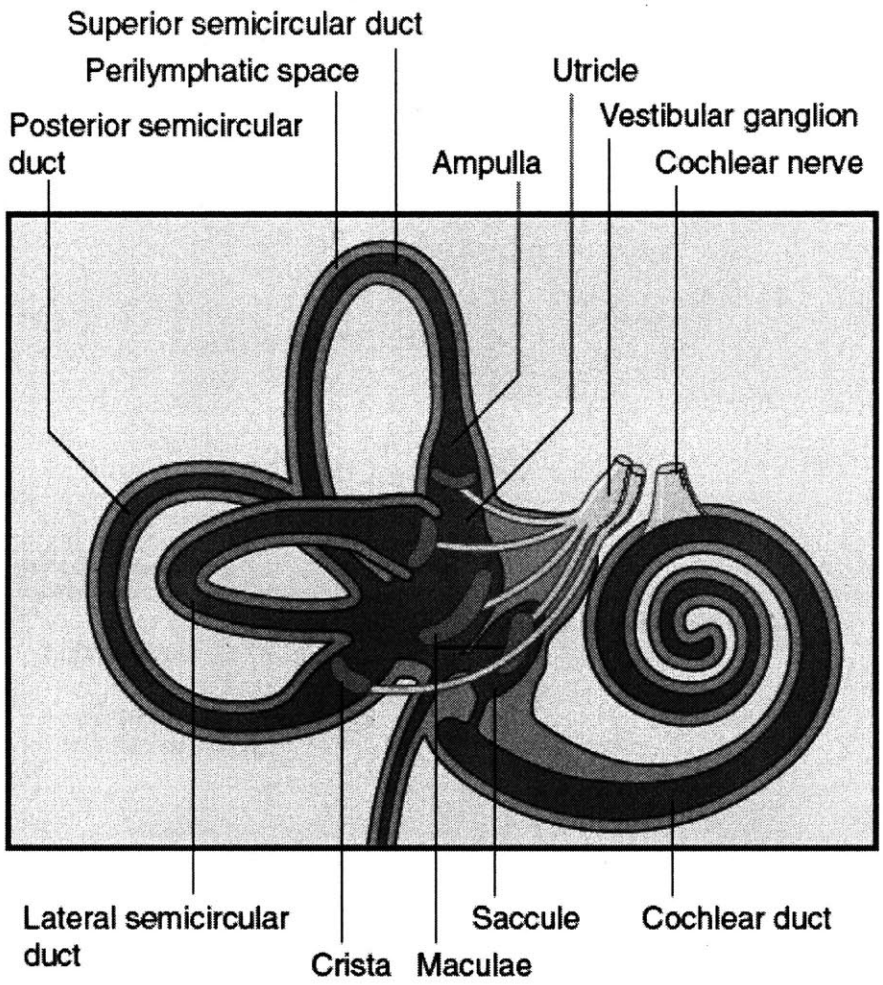

Figure 2-2: Vestibular End-organs [16]

extend their cilia into a gelatinous matrix called the cupula. The three cristae form the kinetic or dynamic labyrinth and are the end-organs responsible for detecting angular head movements.

The otolith organs are a pair of sac-like structures, called the utricle and saccule, that perceive linear acceleration (Figure 2-2). The utricle and saccule each contain an end-organ termed the macula, that together form the static labyrinth responsible for detecting head position. Similar to the cristae of the SCCs, hair cells in the macula also project their cilia into a gelatinous matrix. As seen in Figure 2-4, the matrix differs from the cupula in that it is flat rather than rounded and is blanketed with

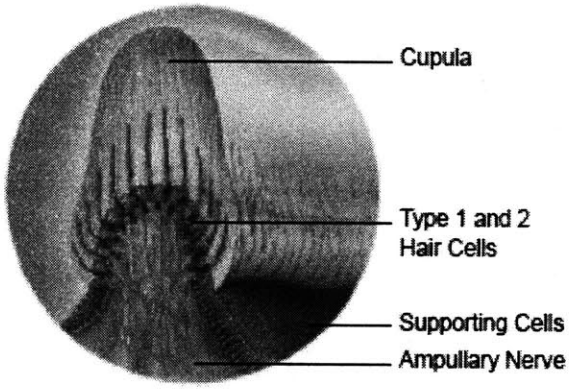

Figure 2-3: Ampullary Crista [15]

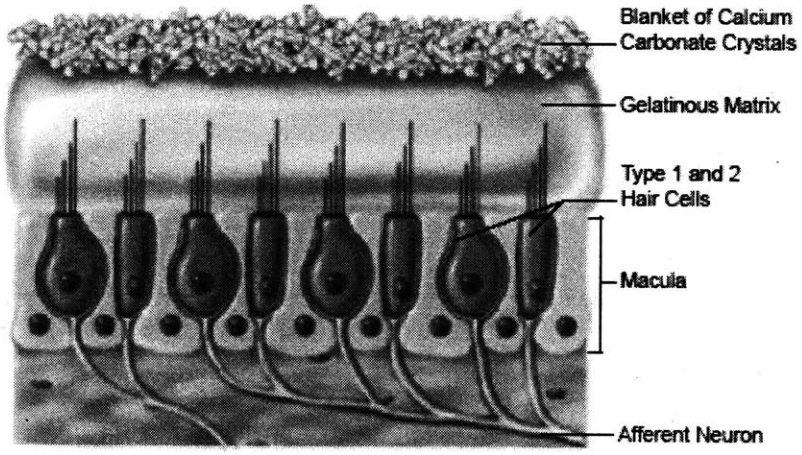

Figure 2-4: Macula of the Otolith Organs [15]

a layer of calcium carbonate crystals.[1] The orientation of the utricular macula is nearly horizontal and senses lateral acceleration, while the orientation of the saccular macula is nearly vertical and senses acceleration due to gravity. The otolith organs detect head position and acceleration in three linear degrees of freedom.

Hair Cells

The fundamental vestibular unit on the microscopic level consists of broadly classified type I and type II hair cells located in the sensory epithelium of the cristae in the SCCs

[1]The term otolith refers to these calcareous particles (*lithos*, Greek for stone) and serves as the origin for the term, *otolith organs*.

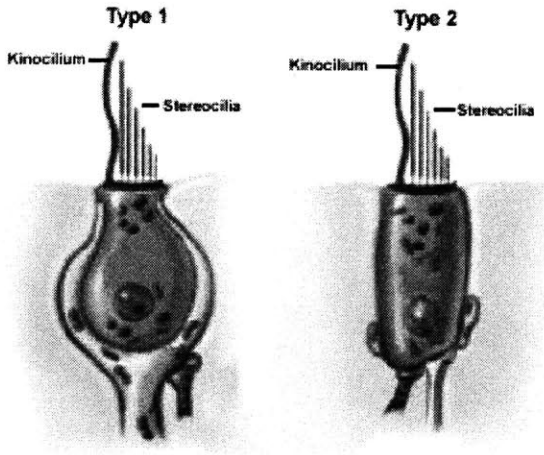

Figure 2-5: Vestibular Hair Cells [15], Modified

and the macula of the otolith organs (Figure 2-5). The hair cells are a mechanical to electrical transduction mechanism responsible for converting accelerations of the head to electrical stimuli sent to the brain. The two types of hair cells are differentiated by shape and afferent nerve termination. Flask-shaped type I cells are terminated by a single calyx-like afferent fiber, while cylindrical type II cells are terminated by multiple bouton afferent endings.

The surface of each hair cell is covered with a series of approximately 50-100 stereocilia embedded into the gelatinous matrix of the cupula in the SCCs and the macula in the otolith organs. The stereocilia (commonly referred to as the *hair bundle*) increase in length with proximity to a single kinocilium, giving each hair cell a characteristic morphological axis of polarity. The polarity plays a crucial role in the physiological mechanism of the hair cell; deflections of the hair bundle toward the kinocilium depolarize the hair cell, while deflections away from the kinocilium hyperpolarize the cell.

Nerves

The vestibulocochlear nerve (cranial nerve VIII) relays auditory and vestibular sensory information from the epilthelia in the inner ear to the brainstem where the fibers separate to their central connections. Information from the vestibular end-organs is

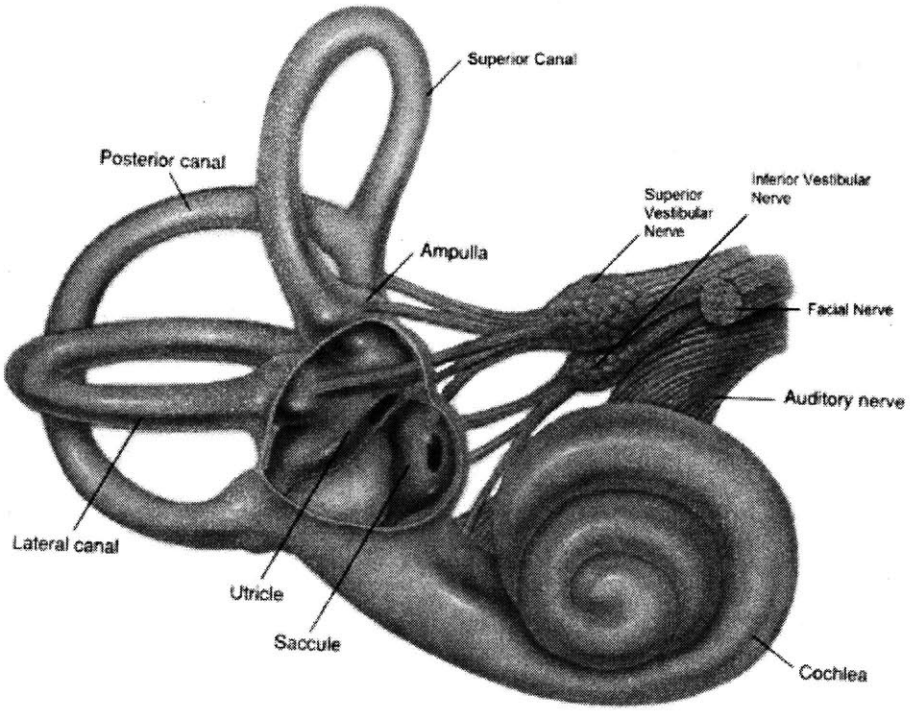

Figure 2-6: Superior and Inferior Branches of the Vestibular Nerve

transmitted along the vestibular portion of the eighth nerve. The nerve is composed of bipolar neurons whose ganglia are located within the internal auditory meatus in a structure known as Scarpa's ganglion [14, 15, 16, 17, 18].

The vestibular nerve branches as it exits the auditory meatus into superior and inferior divisions, as seen in Figure 2-6. The superior division relays information originating from the superior and horizontal SCCs as well as the utricle, while the inferior division relays information originating from the posterior SCC and saccule. Although the primary function of the nerve is to transmit afferent information from the end-organs to the brainstem, an efferent system does exist that most likely serves to modify end-organ activity [15].

The myelinated fibers of the vestibular nerve range in diameter from 1 μm to 10 μm and are broadly classified based on size. As seen in Figure 2-7, medium sized fibers (3–5 μm) constitute over half of the fibers innervating the ampullary crista, while small (<3 μm) and large (>5 μm) fibers roughly constitute a quarter of the total fiber count, respectively [19]. A similar distribution can be seen for nerves

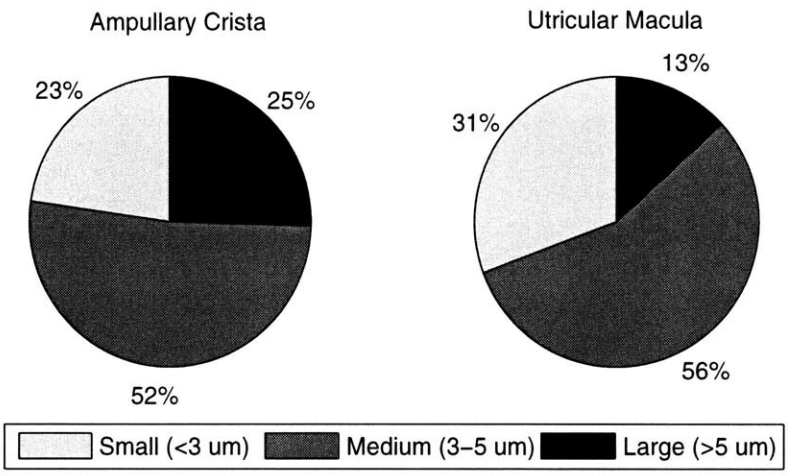

Figure 2-7: Size Distribution of Fibers Innervating the Ampullary Crista and Utricular Macula [19]

innervating the macula of the utricle (Figure 2-7). The spatial distribution of fibers varies over the cross-section of the nerve close to the ganglion; however, at more distal locations the large fibers tend to be centrally located while the medium- to small-sized fibers occupy the nerve periphery. Upon innervating the sensory epithelium, the fibers lose their myelin sheath. To first order, the larger fibers preferentially innervate type I hair cells (Figure 2-5) in a single chalice while medium- to small-sized fibers terminate on type II fibers with multiple bouton endings (Figure 2-5) [1, 18, 20].

2.1.2 Physiology

The basic physiology of the vestibular end-organs can be described in terms of a three-link transduction chain. First, forces due to acceleration displace the seismic elements of the vestibular system, namely the cupula in the SSCs and the macula in the otolith organs. Inertia from the endolymph fluid in the SSCs forces the displacement of hair cells embedded in the cupula for angular head movements. Similarly, linear head movements and gravity are detected from the displacement of the gelatinous matrix located within the macula of the otolith organs. The hair cells embedded within the seismic elements are forced to deflect, as seen for the otolith case in Figure 2-8.

Depending on the orientation of the hair cell in relation to the displacement, the hair bundle is either pushed toward or away from the cell's single kinocilium.

As mentioned in Section 2.1.1, the hair cells behave as mechanical to electrical transducers. Deflections of the stereocilia of the hair cells influence the calcium influx mechanisms near the cell causing the release or reduction of neurotransmitters at the synapse of the afferent neurons; modulation of neurotransmitters effectively modulates the firing activity of the afferent neuron, as seen in Figure 2-9. Deflections of the hair bundle toward the kinocilium increase the firing rate of neurons innvervating the cell (depolarization) relative to rest, while deflections away from the kinocilium decrease the firing rate (hyperpolarization) [14, 15]. Type I hair cells transmit the phasic (quickly changing) component of the response, while type II hair cells transmit the tonic (slow changing) component of the response.

The hair cells in each SSC are arranged such that they all share the same axis of polarity. For a given rotational movement, all of the cells are either depolarized or hyperpolarized in a particular canal. For this reason, the SSCs are said to behave as lumped systems. Unlike the SSCs, the hair cells in the otolith organs do not all share the same axis of polarity. Instead, the hair cells in the macula point toward a single landmark termed the *striola*, as seen in Figure 2-10. Therefore afferent fibers innervating the macula are simultaneously depolarized or hyperpolarized depending on the orientation of the hair cells with relation to head tilt. The otolith organs are thus referred to as distributed systems [14].

2.2 Implantable Vestibular Prostheses

Current investigations on implantable vestibular prostheses are being conducted on two fronts: design of miniaturized components for proposed prostheses [11, 12, 13] and animal studies with externally mounted prosthesis hardware [8, 9, 10]. Investigations on both fronts are currently concerned with stimulating the lumped system of the SSCs, as the signal processing strategies are simpler than for the distributed system of the otolith organs.

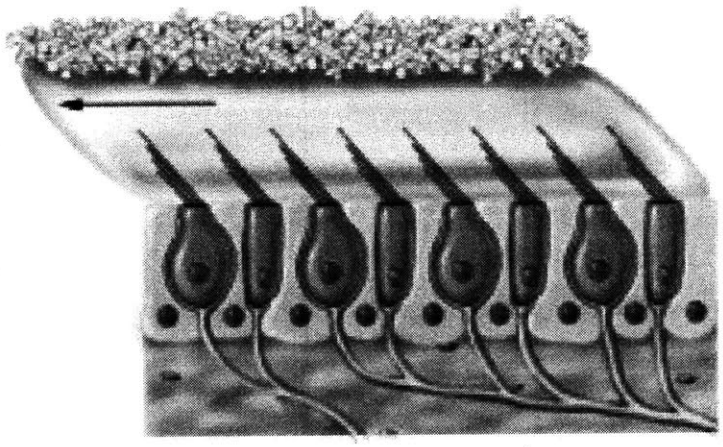

Figure 2-8: Displacement of Hair Cells in the Otolith [15]

Component Miniaturization

Andrei Shkel and his collaborators at UC Irvine are investigating implantable vestibular prostheses using MEMS sensors [11, 12, 13]. They have created a prototype implantable prosthesis using a commercially available yaw rate gyroscope; rotational cues from the sensor are modified with a transfer function to mimic signals recorded from squirrel monkeys during yaw head rotation. The transfer function output is passed through a voltage-to-frequency converter and converted to biphasic current pulses. Preliminary studies with the prosthesis on a rate table indicate the device's output matches the average firing rate of vestibular neurons of animal experiments reported in literature.

Figure 2-11 shows a rendition of a proposed single-axis vestibular prosthesis as envisioned by Shkel and conceptually similar to a cochlear implant. Instead of auditory cues sent to the cochlea, the rate of head yaw rotation as measured with a MEMS gyroscope is sent to the lateral SSC. As an extension of that idea, his group is investigating a MEMS-based sensor capable of sensing motion in all six degrees of freedom (Figure 2-12).

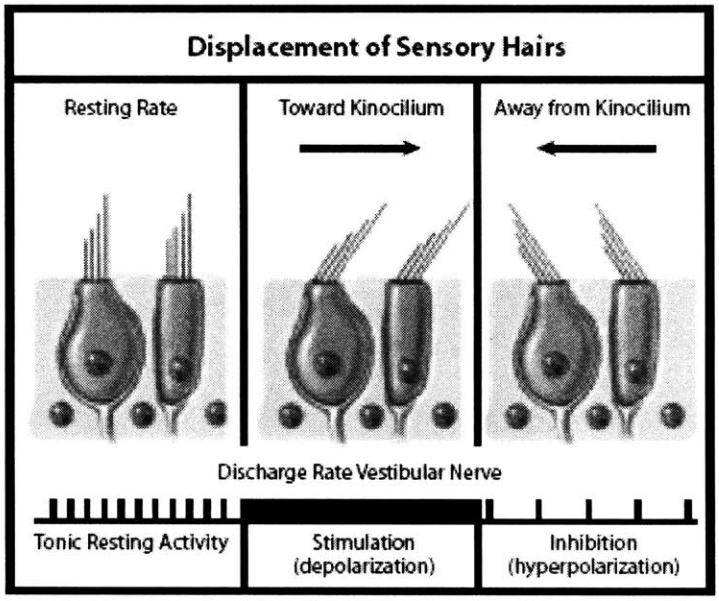

Figure 2-9: Physiology of Hair Cell Displacement [15]

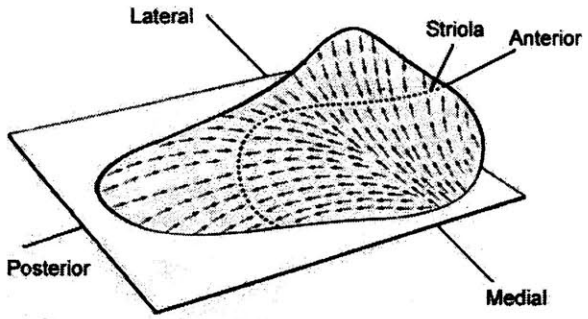

Figure 2-10: Polarization of Hair Cells in Utricular Macula [14]

Animal Studies

Daniel Merfeld and his group have conducted pilot studies on laboratory animals using a prototype neural prosthesis. The prosthesis consists of a single degree of freedom rotation sensor that unilaterally stimulates the semicircular canal of the animal with implanted electrodes. A casing housing the sensors, accompanying circuitry, and power source is firmly attached to the animals head [8, 9, 10].

Gong and Merfeld have demonstrated a prototype semicircular canal prosthesis and concluded that it can provide rotational cues to the nervous system of guinea pigs

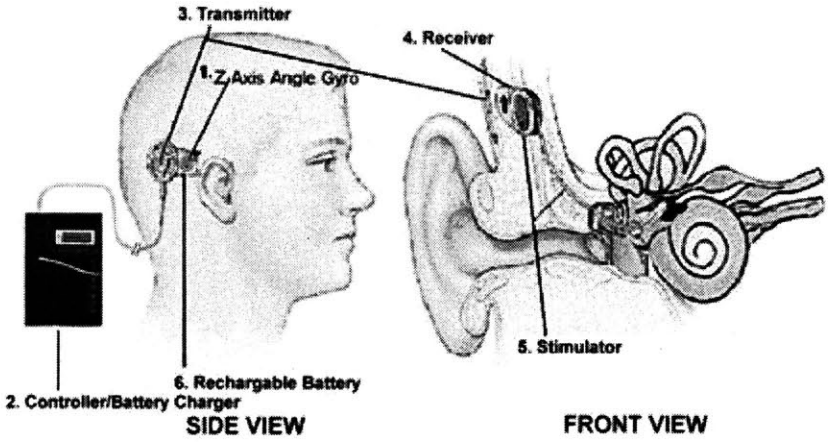

Figure 2-11: Conceptual Rendition of Vestibular Prosthesis [11], Modified

[8, 9]. The prosthetic system was tested on guinea pigs with surgically plugged lateral semicircular canals sensitive to yaw rotation of the head. The animal was presented with a baseline pulse frequency of 150 Hz, higher than the 60 Hz firing rate of normal guinea pigs. The pulse rate was modulated with an angular velocity sensor relative to the baseline frequency (higher rate for rotation in one direction, lower rate for rotation in the opposite direction). After one day of the new stimulation, the animal responded to yaw rotation as measured by the vestibulo-ocular reflex (VOR).[2]

In similar tests, Lewis *et al* demonstrated vestibular adaptation of rotational cues in squirrel monkeys [10]. Stimulation of the horizontal semicircular canal with the prosthesis generated a small measurable gain in the horizontal VOR during yaw rotation of the animal's head. More surprisingly, stimulation of the posterior semicircular canal (sensitive to pitch rotation) with yaw rotational cues from the prosthesis gradually shifted the VOR to the yaw axis. The results demonstrate the plasticity of the VOR in response to motion stimulation and suggest that more studies related to CNS adaptation are needed.

[2]The VOR is a reflexive movement of the eyes triggered by the vestibular system.

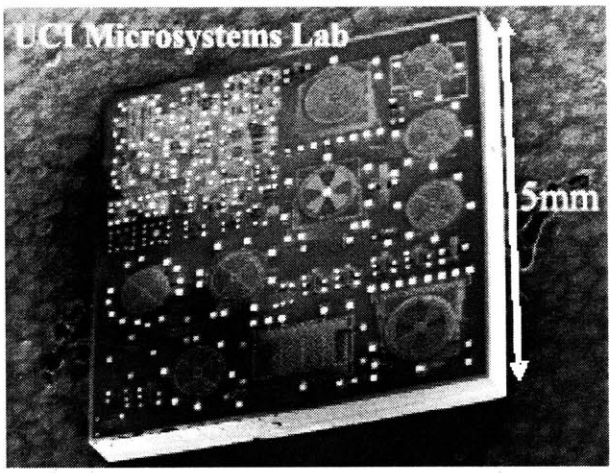

Figure 2-12: MEMS Based Prototype Multi-Sensor Unit [11]

2.3 Peripheral Vestibular Nerves

The evolution of current electrical prostheses is largely driven by combination of experiment and theory. We hope to add to the general knowledge of future implant design by guiding placement of electrodes *in vivo*. In this section, we take a deeper look at the peripheral vestibular nervous system to explain the nerve model described in the following chapter.

As described in Section 2.1.1, the vestibulocochlear nerve (cranial nerve VIII) relays information originating from sense organs in the temporal bone to the brainstem approximately 20 mm proximal [17]. As seen in Figure 2-13, the vestibular portion of the nerve leaves the internal auditory meatus and splits into two characteristic branches, namely the superior vestibular nerve (SVN) and the inferior vestibular nerve (IVN). The nerve fibers[3] in the SVN innervate the ampullae of the superior and lateral semicircular canals, the macula of the utricle and part of the saccule. The fibers in the IVN innervate the posterior semicircular canal and the macula of the saccule. At distal locations near the end-organs, both branches of the vestibular nerve are single-fascicled and therefore contain only a single bundle of fibers. As shown in Figure 2-7, these fibers range in diameter from 1–10 μm.

[3]The terms *nerve fiber* and *axon* are used interchangeably. This work assumes stimulation of peripheral nerve fibers and abstracts away other parts of the vestibular cells including the soma,

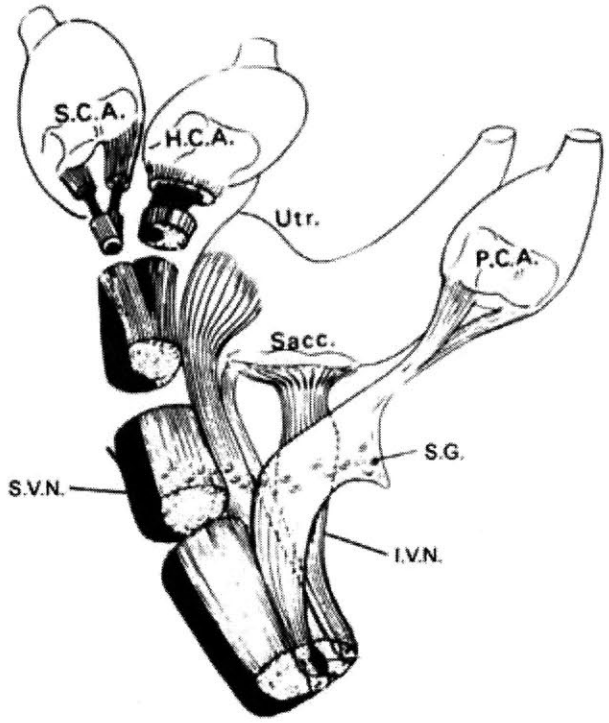

Figure 2-13: Vestibular Nerve Innervating Sense Organs [18], Modified: **S.C.A.**, Superior Canal Ampulla; **H.C.A.**, Horizontal (Lateral) Canal Ampulla; **P.C.A.**, Posterior Canal Ampulla; **Utr.**, Utricle; **Sacc.**, Saccule; **S.G.**, Scarpa's Ganglion; **S.V.N**, Superior Vestibular Nerve; **I.V.N.**, Inferior Vestibular Nerve

For a first attempt at an implantable vestibular prosthesis, we are interested in modeling the electrical activation of peripheral nerves linked to the lumped system of the semicircular canals. Therefore our focus will be on modeling the portion of the IVN that innervates the posterior SSC and the portion of the SVN that innervates the superior and lateral SSCs. Furthermore, our focus will be on stimulating the nerves prior to innervation of their respective ampullae to remain as non-invasive as possible.

The potential candidates for an implantable vestibular prosthesis are likely elderly patients or individuals suffering from various vestibulopathies. A crucial assumption for an implantable prosthesis targeted at stimulating peripheral nerve fibers is that a sufficient number of non-degenerate fibers are present in those individuals. Although the vestibular fiber count in humans does decrease with age [20], a sufficient number

dendrites, and synaptic junctions.

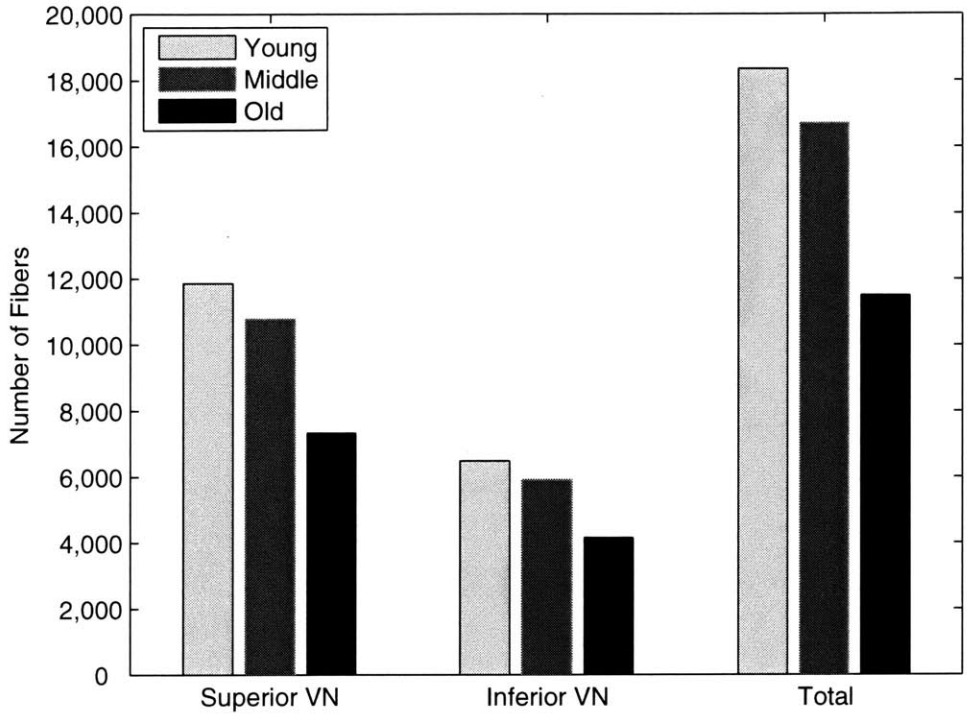

Figure 2-14: Number of Myelinated Fibers in Humans by Age [20]. Fiber count is an average across individuals in each age group: **Young**, 1 day, 6 weeks, 22 years, and 35 years old; **Middle**, 49 and 53 years old; **Old**, 5 cases, 75-85 years old.

of excitable fibers remain to be activated as shown in Figure 2-14. Furthermore, it has been shown that the hair cell density of type I cells does not appreciably decrease in individuals diagnosed with Meniere's disease [21], which alludes to the survival of the nerve fibers attached to those cells.

Chapter 3

Methods

The proposed vestibular implant will excite peripheral vestibular nerves using electrical current delivered through implanted electrodes in the temporal bone. For reasons of practicality, the electrodes will not penetrate the neurons being excited (*intracellular stimulation*). Instead, fields generated by extracellular electrodes will drive currents applied to the neuron to elicit excitation by means of *extracellular stimulation.* The following chapter describes the theory of extracellular nerve stimulation and details the methods used for simulation.

3.1 Analysis of Extracellular Stimulation of Myelinated Peripheral Nerves

The analysis of nerve excitation via extracellular stimulation is based on the pioneering work of McNeal [22] who evaluated the response of a myelinated nerve fiber to an electric field arising from a point current source. Prior to McNeal, all theoretical models assumed excitation was initiated by currents applied directly to a node ([23], for example). The assumption is only valid for intracellular stimulation where localized currents can be applied directly to nodes. Currents produced by extracellular stimuli are not localized and affect multiple nodes simultaneously. Furthermore, McNeal's model improved on previous models by allowing arbitrary stimulus duration

and electrode configurations.[1]

3.1.1 Method of McNeal

The McNeal method involves a two-step approach to analyze the extracellular stimulation of a nerve fiber. In the first step, the electric potentials created in the extracellular space by a specified electrode configuration are calculated. For ease of calculation, the extracellular space is modeled as a volume conductor of simplified geometry and is usually considered to be a linear, homogeneous, and isotropic medium of infinite extent. Analytical solutions exist for relatively simple electrode geometries (e.g. monopoles, dipoles, n-poles), while the potentials generated from more complex electrode geometries in inhomogeneous and/or anisotropic media must be found using numerical techniques.[2]

The second step of the McNeal method involves applying the known extracellular potentials to a model of the nerve fiber. The nerve fiber model is based on classic core-conductor theory [23, 26]. The single fiber or axon model is chosen based on the anatomy of interest and the desired level of precision. McNeal chose to analyze a Frankenhauser-Huxley nerve model excited in a homogeneous, isotropic medium by a point source of current [22]. The choice of axon model and media complexity is based on the specific problem of interest; nevertheless, the methodology remains the same.

3.1.2 McNeal Nerve Model

To first order, the myelinated nerve fibers of interest are modeled by an equivalent linear electric network model as seen in Figure 3-1. Each nerve segment represents a single node of Ranvier with width l, and an internodal spacing L that is proportional to the fiber diameter D and axon diameter d. The membrane at a node of Ranvier is modeled with a resting potential V_r, lumped ionic conductance G_m, and capacitance C_m. The axoplasmic conductance is represented by G_a and the myelin sheath is

[1] Previous theoretical studies assumed infinite duration pulses and researchers relied on experimentally derived strength-duration curves for arbitrary pulse durations. Also, only limited electrode geometry was considered, such as bipolar electrodes in direct contact with the nerve ([24], [25], *etc.*).

[2] See sections 3.2.2 Volume Conductor (page 48) and 3.2.3 Source-Field Models (page 50).

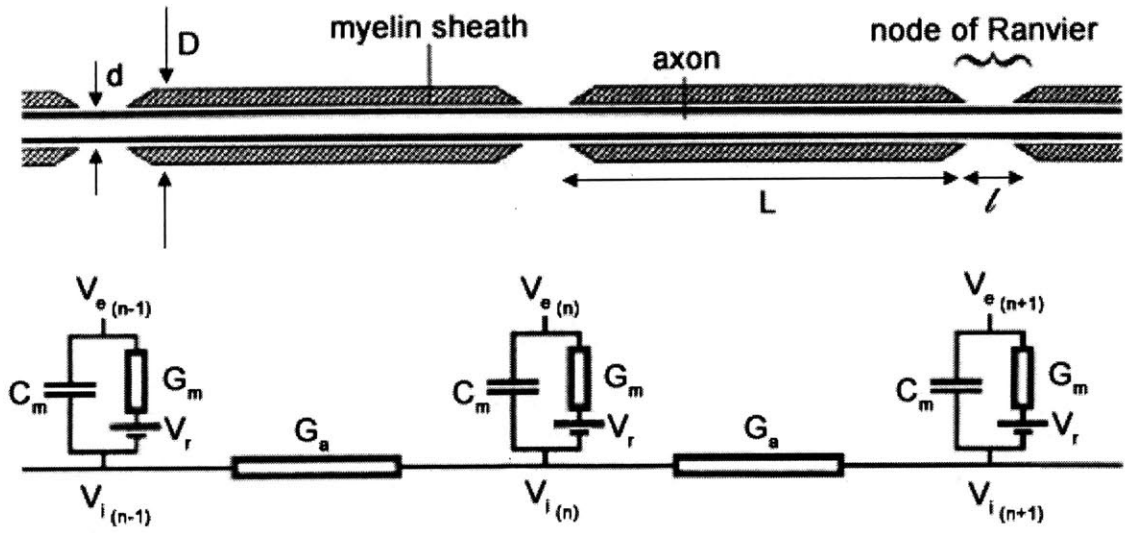

Figure 3-1: Linear Circuit Model of the Nerve [28], Modified: **d**, Axon Diameter; **D**, Fiber Diameter; l, Node of Ranvier Length; **L**, Internodal Length; $\mathbf{V_r}$, Membrane Rest Potential; $\mathbf{G_m}$, Lumped Ionic Membrane Conductance; $\mathbf{C_m}$, Membrane Capacitance; $\mathbf{G_a}$, Axoplasmic Conductance; $\mathbf{V_{e_{(n)}}}$, Extracellular Potential; $\mathbf{V_{i_{(n)}}}$, Intracellular Potential; All Potentials are Referenced to a Far-Field Ground.

modeled as perfectly insulating.[3] $V_{e_{(n)}}$ and $V_{i_{(n)}}$ are the extracellular and intracellular potentials at a node, respectively. $V_{m_{(n)}}$, the transmembrane potential, denotes the deviation of the membrane potential from rest, namely $V_{m_{(n)}} = V_{i_{(n)}} - V_{e_{(n)}} - V_r$.

Application of Kirchhoff's current law to the electrical network for node n states we must have conservation of capacitive, ionic, and axial currents

$$I_{cap_{(n)}} + I_{ion_{(n)}} = I_{axial_{(n)}} \tag{3.1}$$

Expansion of the currents in terms of the transmembrane voltage V_m yields a set of differential equations discrete in space and continuous in time known as the cable

[3]This is a common assumption in nerve simulation studies ([22], [27], [28], *etc.*) The equations for a more detailed model can readily be obtained by compartmentalization of the myelin. Richardson *et. al.* [29] compared models with perfectly insulating myelin and myelin modeled as a finite impedance cable and found both strength-duration and current-distance relationships to be within experimental ranges.

equations. For the n^{th} node, we have[4]

$$\begin{aligned} C_m \frac{dV_{m_{(n)}}}{dt} + G_m V_{m_{(n)}} &= G_a(V_{i_{(n-1)}} - V_{i_{(n)}}) + G_a(V_{i_{(n+1)}} - V_{i_{(n)}}) \\ &= G_a(V_{i_{(n-1)}} - 2V_{i_{(n)}} + V_{i_{(n+1)}}) \\ &= G_a(V_{m_{(n-1)}} - 2V_{m_{(n)}} + V_{m_{(n+1)}}) + G_a(V_{e_{(n-1)}} - 2V_{e_{(n)}} + V_{e_{(n+1)}}) \end{aligned}$$

and after rearranging yields

$$C_m \frac{dV_{m_{(n)}}}{dt} + G_m V_{m_{(n)}} - G_a(V_{m_{(n-1)}} - 2V_{m_{(n)}} + V_{m_{(n+1)}}) = G_a(V_{e_{(n-1)}} - 2V_{e_{(n)}} + V_{e_{(n+1)}}) \tag{3.2}$$

We seek precisely the solution of the cable equations for the transmembrane voltage V_m, given an externally applied stimulus V_e, to determine spatial and temporal nerve firing behavior.

3.1.3 McNeal Specific Assumptions

In addition to the standard assumptions in core-conductor theory that allow for a circuit-based representation of the nerve [23, 26], the McNeal method assumes the following:

1. The electric potential outside the fiber is determined only by the stimulus current, the electrical properties of the surrounding tissue, and the specific electrode geometry, **and is not influenced by the presence of the fiber**.

2. The external surface of any one node is at an equipotential, thus variations in current density over the nodal surface can be neglected.

The first assumption is justified since the dimensions of the single fiber are quite small and the fiber is generally located a given distance from the electrodes. Thus, the presence of the fiber itself is unlikely to alter the potential field generated by the stimulating electrodes. Furthermore, Plonsey has shown [30] that the secondary field

[4]Note that the membrane rest potential, V_r, is calculated using the Goldman Equation based on intracellular and extracellular ion concentrations and does not change with time. That is, $\frac{dV_r}{dt} = 0$.

generated by currents traveling down the length of the single fiber is two orders of magnitude smaller than the field generated by the stimulating electrodes.[5] Ephaptic coupling, or the synchronous firing of adjacent parallel fibers in a nerve bundle, may have an affect on the stimulating field in certain instances [31]. However, this case is ignored since we are only modeling the response of a *single* fiber to an imposed extracellular field.

The second assumption requires that the electric field generated by the electrode configuration produces a radially symmetric equipotential region outside of the axon at a given position along its length. For most electrode configurations, this condition will not strictly be satisfied. However, McNeal has shown [22] that transverse variations in extracellular potential are significantly smaller than longitudinal variations in potential along the axon. As we shall see in the Section 3.2.4, it is precisely the longitudinal variations in potential that drive the nerve stimulation.

3.2 Formulation of the Model

Inherent to any modeling endeavor is the dichotomy between accurately describing the problem to be modeled and the need to simplify the problem domain into something tractable. Oftentimes this process involves making gross simplifications and assumptions as a starting point for the model. The following sections describe the formulation of the model used to describe the electrical stimulation of peripheral vestibular nerves. It must be stressed that the methods used below are generic, allowing for more advanced models to follow without loss of generality.

3.2.1 Geometrical Simplifications

The present work aims to model the electrical stimulation of peripheral vestibular nerves innervating the semicircular canals (SSCs), as described in Section 2.3. In particular, we will model two cases of interest for an implantable prosthesis: the

[5]The secondary potential was shown to be 600 times smaller than the stimulating potential for the standard parameters used by McNeal [22], namely an axon diameter of $10\,\mu m$ and monopolar stimulus located $1\,mm$ away from the fiber.

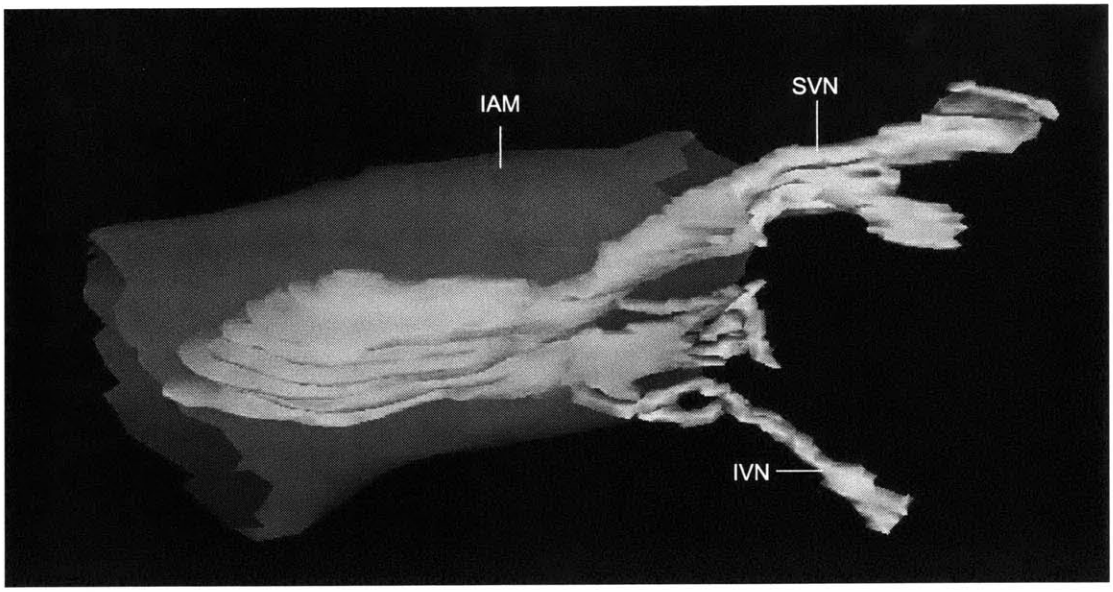

Figure 3-2: Digitized Reconstruction of a Human Vestibular Nerve [32] showing Characteristic Branching into Superior and Inferior Divisions: **IAM**, Internal Auditory Meatus; **SVN**, Superior Vestibular Nerve; **IVN**, Inferior Vestibular Nerve.

inferior vestibular nerve (IVN) innervating the ampulla of the posterior SSC and the branching superior vestibular nerve (SVN) innervating the ampullae of the superior and lateral SSCs. The basis for the geometrical simplifications include stylized models of vestibular geometry such as Figure 2-13, as well as a digitized reconstruction of a human vestibular nerve [32] as seen in Figure 3-2.

The IVN was modeled as a right cylinder of length $5\,mm$ and diameter of $0.7\,mm$, as seen in Figure 3-3. The nerve fascicle consists of $0.5\,mm$ diameter nerve tissue surrounded by a $50\,\mu m$ epineurium sheath and a $50\,\mu m$ layer of saline, representing cranial fluids. The SVN was modeled such that two fused cylinders split at a 30° angle to form the characteristic branches [33]. As seen in Figure 3-4, the branches are approximately $2\,mm$ in length, while the entire nerve is $6\,mm$ long [33]. Figure 3-5 shows a three-dimensional representation of the SVN model; the cross-sectional tissue variation for the SVN model is identical to the IVN model.

It must be noted that the exact morphology of nerves differs from person to person and in general is not well-characterized, particularly in the splitting region of the SVN. The separation distance and divergence angle of the two branches may well

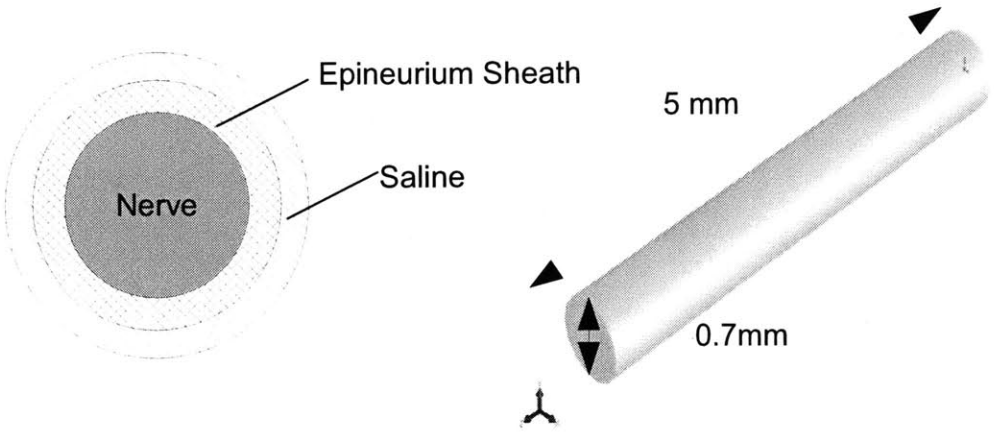

Figure 3-3: Model of Inferior Vestibular Nerve

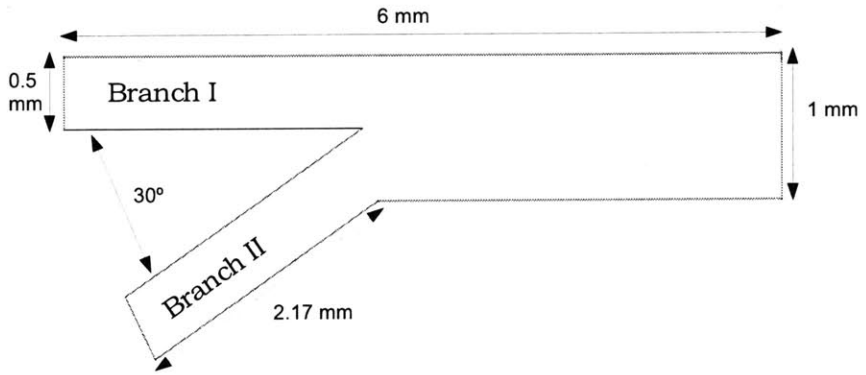

Figure 3-4: Dimensions of Superior Vestibular Nerve Model: Branch II splits at a 30° angle from Branch I

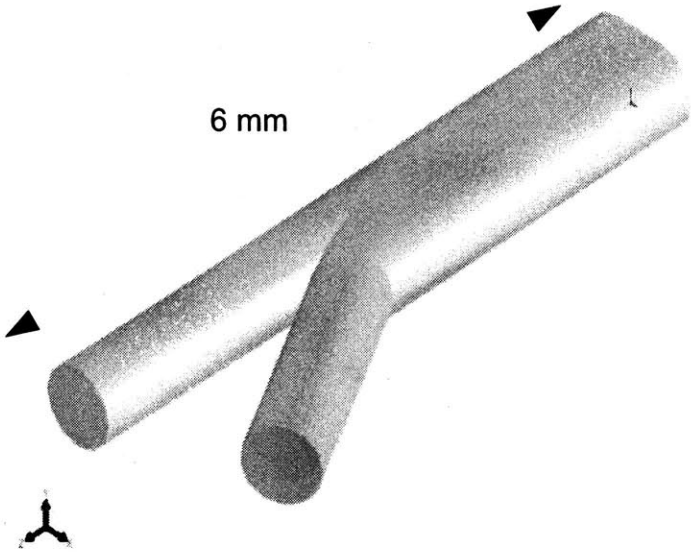

Figure 3-5: Model of Superior Vestibular Nerve

be much smaller than our model indicates, even to the limit where the two branches are fused together. Therefore the above rendition of the split SVN must be treated as a favorable scenario where two distinct branches of significant size are present.

3.2.2 Volume Conductor

As described in Section 2.1, the peripheral vestibular nerves lie within the complex structure of the temporal bone. From a simulation perspective the environment must be simplified into a domain that is tractable to solve. More specifically, we are interested in the solution of bioelectric fields generated from a given configuration of current sources located in the conducting medium.[6] The simplified conducting medium extends continuously in three-dimensions and is referred to as a *volume conductor.*

For the biological tissues and stimulus durations being modeled, the capacitive

[6]This is commonly referred to as the *forward problem* and is guaranteed to have a unique solution. Conversely the *inverse problem* is concerned with the determination of sources that generate a particular field pattern, such as from measured electric signals. The solution to the inverse problem is not unique [34].

component of tissue impedance is negligible and the currents in the volume conductor are dominated by conduction currents. Consequently, an ohmic description of the volume is sufficient and requires only the specification of tissue conductivity. Furthermore, electromagnetic propagation effects can be neglected [34]. This condition implies that the electromagnetic fields can be treated as *quasi-static*, and the phase of the time variation can be ignored [35].

The forward problem reduces to calculating the potential field for a given source configuration and requires the solution of *Poisson's* equation with appropriate boundary conditions. Poisson's equation,

$$\nabla^2\Phi = \frac{\nabla \cdot \mathbf{J}}{\sigma} \tag{3.3}$$

relates the second spatial derivative of potential, $\Phi\,[V]$, to the divergence of the the source current density $\mathbf{J}\,[\frac{A}{m^2}]$. For ease of potential field calculation, the majority of volume conductors are modeled as linear, homogeneous, and isotropic media of infinite extent for which analytical solutions are easily derived ([22, 29, 36, 37, 38, 39, 40, 41], for example). Analytical solutions for electric potential in inhomogeneous and/or anisotropic volume conductors have also been derived for a subset of highly symmetrical geometries that exhibit simple boundaries. Investigators have employed techniques such as the method of images [42], coordinate transformations [28, 42], and also Fourier transform methods [28, 30, 36, 43, 44, 45] to derive analytical solutions for the potential field.

However, analytic solutions to Poisson's equation are not always possible, especially for volume conductors that do no exhibit symmetry or that have complicated boundary conditions. For such models, or models with arbitrary source configurations, numerical implementation of current conservation is necessary to solve for the potential distribution. Several models of peripheral nerve stimulation have been conducted using finite difference [46, 47, 48] or finite element [49, 50, 51, 52, 53, 54, 55] methods. The trade off to increased model complexity is an increase in computation time.

Tissue	Resistivity (Ωmm)	Reference
Nerve (transverse)	1.25 x 10^4	[56]
Nerve (longitudinal)	2 x 10^3	[56]
Epineurium Sheath	1.25 x 10^4	[52]
Saline	5 x 10^2	[56]
Bone	5 x 10^4	[56]

Table 3.1: Tissue Resistivity

Two types of volume conductors were used to model the peripheral vestibular nerves with increasing complexity. The first domain was a homogeneous, isotropic medium with the averaged conductivity of bone, nerve, epineurium tissue, and saline fluid. Table 3.1 lists the resistivities of the tissues of interest, with an average value of ρ = 1.94 x $10^4\,\Omega mm$. A second, more detailed volume conductor that is inhomogeneous and anisotropic was created for each set of nerve geometries described in Section 3.2.1. As seen in Figures 3-3 and 3-5, the volume conductor incorporated bone, nerve, and epineurium tissue surrounded by layer of saline fluid. The bone and epineurium tissues have isotropic conductivity, while the nerve tissue has anisotropic conductivity that differs in the radial and longitudinal directions, respectively. The resistivity of epineurium is not known but was assumed to be equivalent to the transverse resistivity of nerve because of a similarity between the connective tissue [52].

3.2.3 Source-Field Models

The potential field solution $\Phi(x, y, z)\,[V]$ in the aforementioned volume conductor is derived from electromagnetic wave theory [34, 57, 58]. The existence of currents in the conductor implies the presence of an electric field $\mathbf{E}(x, y, z)\,[\frac{V}{m}]$[7], that in the quasi-static approximation [35] can be expressed as

$$\mathbf{E} = -\nabla\Phi \tag{3.4}$$

The electric field exerts a force upon charges in the medium that causes them to flow, thereby producing a current. The current density $\mathbf{J}\,[\frac{A}{m^2}]$ is related to the electric field

[7]Boldface symbols represent vector quantities.

by the complex conductivity tensor as

$$\mathbf{J} = (\sigma + j\omega\epsilon_r\epsilon_0)\mathbf{E}, \tag{3.5}$$

where σ is the material conductivity $[\frac{S}{m}]$, ω is the angular frequency of the $\mathbf{E}$ field $[\frac{rad}{s}]$, ϵ_0 is the permittivity of free space $[\frac{F}{m}]$, and ϵ_r is the dimensionless relative permittivity of the material. For the biological tissues and stimulus durations being modeled, the capacitive component of tissue conductance is negligible ($\sigma \gg j\omega\epsilon_r\epsilon_0$), and equation 3.5 reduces to a form of Ohm's law [34]. That is,

$$\mathbf{J} = \sigma\mathbf{E} \tag{3.6}$$

Gauss' Divergence Theorem relates the volume integral of the divergence of the current density to the net flux through a surface that encloses the volume, as seen in equation 3.7.

$$\int_v \nabla \cdot \mathbf{J} dv = \oint_s \mathbf{J} \cdot ds \tag{3.7}$$

The integral of the current density over the surface enclosing the volume is precisely given as

$$\int_s \mathbf{J} \cdot ds = \int_v I_s, \tag{3.8}$$

where $I_s(x, y, z)\,[\frac{A}{m^3}]$ is the enclosed current source density. Comparison of equation 3.7 to 3.8 reveals

$$\nabla \cdot \mathbf{J} = I_s, \tag{3.9}$$

a statement of the conservation of current. Substituting equation 3.4 into equation 3.6 and taking the divergence of both sides, we see (with constant σ)

$$\begin{aligned} \nabla \cdot \mathbf{J} &= \nabla \cdot (-\sigma \nabla \Phi) \\ &= -\sigma \nabla^2 \Phi \end{aligned} \tag{3.10}$$

Equating the right sides of equations 3.9 and 3.10 and rearranging yields *Poisson's* equation, namely,

$$\nabla^2\Phi = -\frac{I_s}{\sigma} \tag{3.11}$$

Poisson's equation, in the absence of sources, reduces to *Laplace's* equation,

$$\begin{aligned} \nabla^2\Phi &= -\frac{I_s}{\sigma} \\ &= 0 \end{aligned} \tag{3.12}$$

It is precisely Poisson's equation (Laplace's equation in source-free regions) that we wish to solve to calculate the potential field for a given source configuration.

Anisotropy

The previous derivation assumed a scalar value for σ, as is the case in isotropic media. Inspection of equation 3.6 reveals that the current density $\mathbf{J}$ is in the same direction as the electric field $\mathbf{E}$. For anisotropic media, however, equation 3.6 must be written in tensor form as

$$\mathbf{J} = \bar{\bar{\sigma}}\mathbf{E}, \quad \bar{\bar{\sigma}} = \begin{bmatrix} \sigma_{xx} & \sigma_{xy} & \sigma_{xz} \\ \sigma_{yx} & \sigma_{yy} & \sigma_{yz} \\ \sigma_{zx} & \sigma_{zy} & \sigma_{zz} \end{bmatrix} \tag{3.13}$$

The current density is weighted by the conductivity tensor for a given direction of the $\mathbf{E}$ field, resulting in a current density that may be rotated with respect to the electric field.

The nerves we wish to model have a higher conductivity in the longitudinal direction than in the transverse direction due to their structure. For a nerve situated with its principal axis along the z direction, the conductivity tensor in equation 3.13 reduces to

$$\bar{\bar{\sigma}} = \begin{bmatrix} \sigma_t & 0 & 0 \\ 0 & \sigma_t & 0 \\ 0 & 0 & \sigma_l \end{bmatrix}, \tag{3.14}$$

where σ_t and σ_l refer to the transverse and longitudinal conductivities, respectively.

Due to the complexity of our nerve model, numerical techniques were used to solve Poisson's equation for the anisotropic (and inhomogeneous) case.

The finite element package Ansys Mechanical/Emag (version 9.0, Ansys, Inc.) was used to calculate the potential field in the inhomogeneous and anisotropic volume conductor for a given electrode configuration (see Section 3.2.3). Ansys provides a convenient way to model orthotropic conductivities by assigning material conductivities that differ along the cardinal axes. For the case of the inferior vestibular nerve (IVN), an anisotropic model was achieved by simply placing the nerve parallel to a cardinal axis and assigning that axis a higher conductivity relative to the other two axes. However, the superior vestibular nerve (SVN) model contains two branches, both preferentially conducting longitudinally. It is not possible for both branches to be aligned to a cardinal axis, given their separation is 30°. To overcome this problem, the nerve was first placed such that the upper branch in Figure 3-4 (Branch I) was parallel to the cardinal z axis. The element coordinate system for the elements comprising the nerve tissue for the lower branch (Branch II) were then rotated 30° in the x-z plane to properly align the conductivity tensor with the lower branch (Figure 3-6). Thus, the nerve tissue in both branches was anisotropic.[8] To my knowledge, no other paper studying the excitation of nerves has included this level of detail in modeling, namely an inhomogeneous, anisotropic branched nerve structure.

Duality

The equations in the previous section are very similar to those found in classical electrostatics [58]. Since most electrical engineers are familiar with the governing equations of electrostatics, the following is presented as an alternate means to derive equations 3.4, 3.6, 3.9, and 3.11 for the interested reader. While electrostatics is concerned with the study electric fields and charges in dielectric media, our interest lies in the study of currents in conductive media. Nevertheless, the similarity in the governing equations of both fields allows for transformation from one context to the other.

[8]For details, consult Appendix A.1

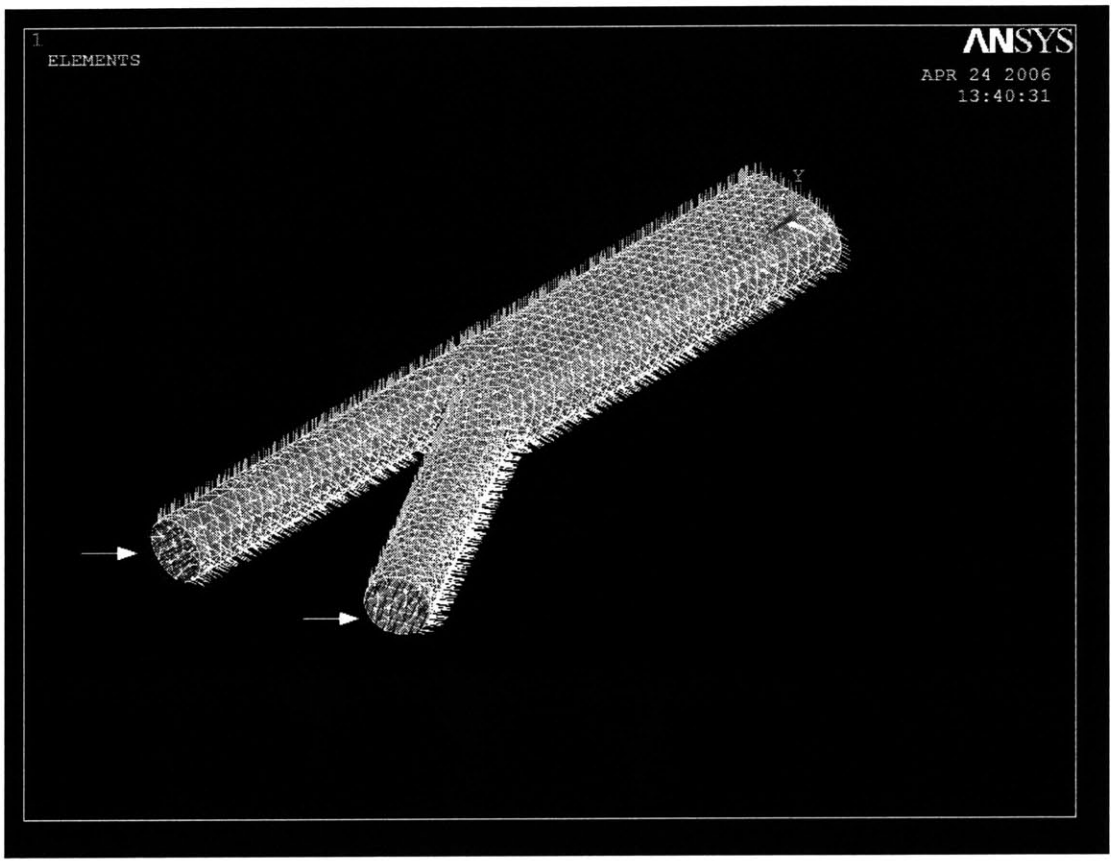

Figure 3-6: Rotation of the Element Coordinate System for the Superior Vestibular Nerve: The dark lines parallel to both branches (indicated by arrows) denote the virtual z axis, which has a higher conductivity than the x or y axes.

The governing equations for electrostatics are

$$\mathbf{E} = -\nabla\Phi \tag{3.15}$$

$$\mathbf{D} = \epsilon\mathbf{E} \tag{3.16}$$

$$\nabla \cdot \mathbf{D} = \rho \tag{3.17}$$

$$\nabla^2\Phi = -\frac{\rho}{\epsilon} \tag{3.18}$$

where $\rho\,[\frac{C}{m^3}]$ is the charge density, $\epsilon\,[\frac{F}{m}]$ is the material permittivity, and $\mathbf{D}\,[\frac{C}{m^2}]$ is the electric displacement field. Equations 3.15, 3.16, 3.17, 3.18 correspond precisely with equations 3.4, 3.6, 3.9, 3.11 provided the following transformations are made:

$$\epsilon \rightarrow \sigma \tag{3.19}$$

$$\mathbf{D} \rightarrow \mathbf{J} \tag{3.20}$$

$$\rho \rightarrow I_s \tag{3.21}$$

The correspondence is an application of the *principle of duality.*

Electrode Configurations

Six electrode configurations were used to model the stimulation of peripheral vestibular nerves for the inferior vestibular nerve, as seen in Figure 3-7. Circles enclosing a "+" denote anodes (sources of current), while circles enclosing a "−" denote cathodes (sinks of current). The same configurations were chosen to excite the superior vestibular nerve (Figure 3-8), with the exception of electrode configuration 3. For the inferior nerve, the separation of the transverse dipole was held constant as the electrode-to-nerve distances were increased. However, in the superior nerve case, the anode remained stationary between the two branches while the cathode distance was incrementally increased.

The configurations were chosen for their prevalence in electrical stimulation studies and also for their modeling simplicity. Each configuration is based upon the monopole, literally *single pole*, that describes a single point source (or sink) of current in the

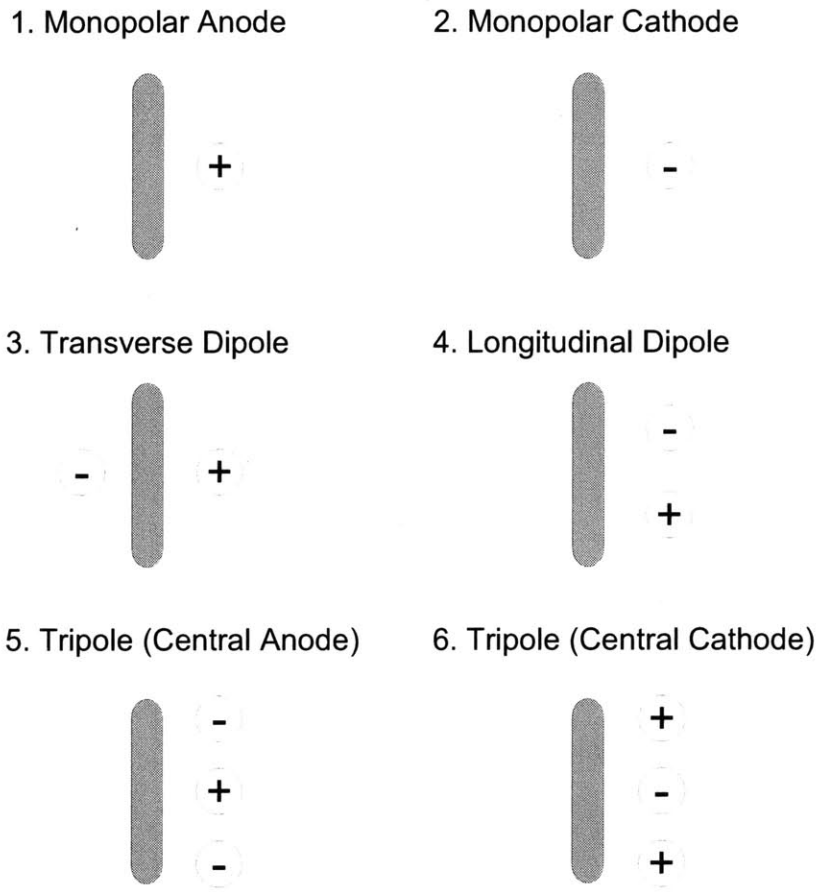

Figure 3-7: Modeled Electrode Configurations for the IVN Case as seen in Top View (x-z plane), *not to scale*: A circle enclosing a "+" denotes an anode, a circle enclosing a "−" denotes a cathode, and a gray cylinder represents a nerve. All electrodes were placed in the plane of the nerve in the y axis (out of the page), and the separation between electrodes was held constant at $1\,mm$ in the x-z plane for Configurations 4-6. All electrodes were modeled as point sources.

volume conductor. Although an isolated monopole cannot exist in nature due to the conservation of current, the potential field generated by a theoretical monopole accurately describes the potential field around a single pole of a widely separated dipole. Such a scenario occurs when the return electrode of a dipole pair is placed far from the source electrode.[9] Furthermore, more complex sources can easily be derived from the superposition of monopoles (dipoles, tripoles, ..., n-poles) [34, 58].

Solving Poisson's equation (Equation 3.11), we can derive the analytical solution for the potential field generated by a monopole in a linear, homogeneous, and isotropic medium of infinite extent. Due to the homogeneous and isotropic nature of the volume, we expect the current from the monopole to flow in the radial direction, with uniform current density $\mathbf{J}$ on concentric spheres around the source. From Equation 3.8, we see the the current density $\mathbf{J}$ on a spherical surface of arbitrary radius r from the source must simply be the source strength I divided by the surface area of the sphere. That is,

$$\mathbf{J} = \frac{I}{4\pi r^2}\hat{r}, \tag{3.22}$$

where $I\,[A]$ is the source current and $\hat{r}$ is a unit vector in the radially outward direction. Applying Equations 3.4 and 3.6 to Equation 3.22 results in

$$\mathbf{J} = \frac{I}{4\pi r^2}\hat{r} = -\sigma\nabla\Phi \tag{3.23}$$

Since the field is everywhere radial, there should be no transverse variation of potential, *i.e.* we expect equipotential surfaces for constant values of r. Therefore only the component of $\nabla\Phi$ in the direction of r can arise. This yields

$$-\sigma\frac{d\Phi}{dr} = \frac{I}{4\pi r^2}\hat{r} \tag{3.24}$$

Integration with respect to r and letting $\Phi(r \to \infty) = 0$ gives us

$$\Phi(r) = \frac{I}{4\pi\sigma r}, \tag{3.25}$$

[9] A common practice in neural stimulation is to place the stimulating electrode close to the nerve of interest and place the return electrode on a person's shoulder.

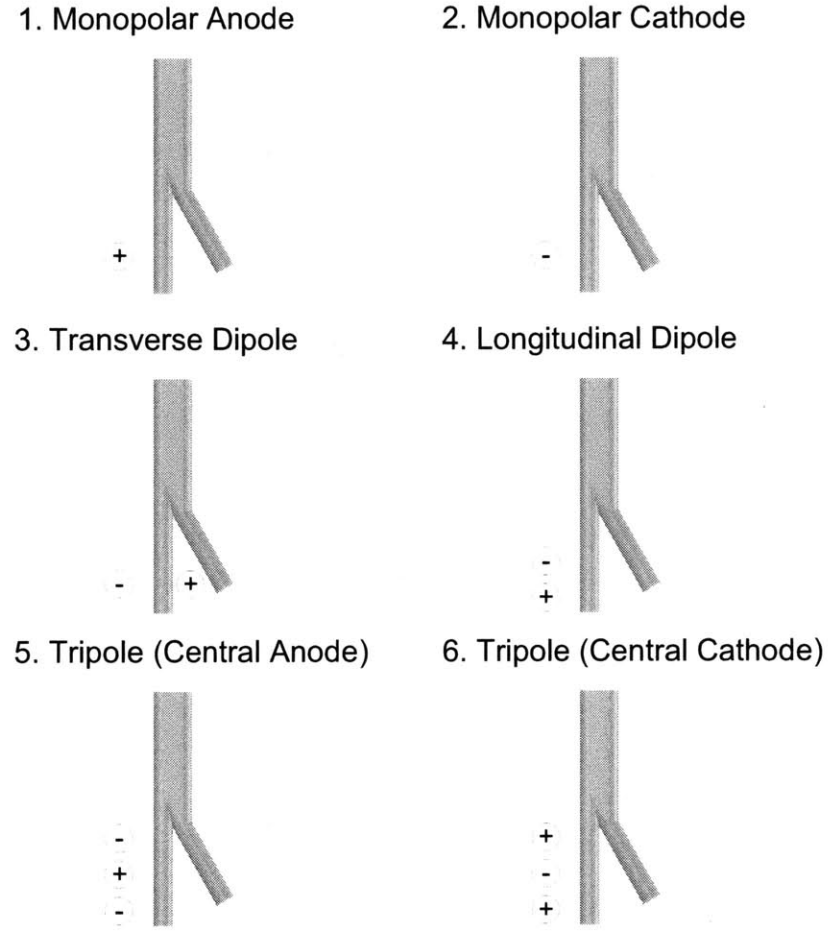

Figure 3-8: Modeled Electrode Configurations for the SVN Case as seen in Top View (x-z plane), *not to scale*: A circle enclosing a "+" denotes an anode, a circle enclosing a "−" denotes a cathode, and a gray cylinder represents a nerve. All electrodes were placed in the plane of the nerve in the y axis (out of the page), and the separation between electrodes was held constant at $1\,mm$ in the x-z plane for Configurations 4-6. All electrodes were modeled as point sources. Note: The anode in configuration 3 remains stationary.

the solution of the potential field in a homogeneous, isotropic medium of conductivity σ from a monopolar electrode of strength I. As suspected, Φ is constant on surfaces with constant r, and the potential decays as $\frac{1}{r}$. Due to the linearity in the field calculation, the solution to the potential field for the other electrode configurations were found using superposition.

The potential field in the inhomogeneous and anisotropic volume conductor was calculated numerically for all six configurations. For the dipolar configurations (Configurations 3 and 4), the electrodes were driven with equal magnitude and opposite sign to conserve current. Similarly, the flanking electrodes for the tripolar configurations (Configurations 5 and 6) were driven at half the magnitude of the central electrode. All electrodes were modeled as infinitesimal point sources for simplicity.[10] The electrodes were placed in the plane of the nerve in the y axis (out of the page in Figures 3-7 and 3-8), and the separation between electrodes was held constant at $1\,mm$ in the x-z plane for Configurations 4–6.

3.2.4 Nerve Fiber Models

Two models were used to analyze nerve firing behavior with increasing levels of complexity. The first model, termed the "activating function" is derived from the linear representation of a nerve fiber as seen in Figure 3-1. The model focuses on the field patterns produced by electrodes and their influence on the nerve fiber. The second model, described by Schwarz, Eikhof and Frijns, is based on the nonlinear characteristics of myelinated mammalian nerves. The details of both models are described below.

Activating Function

Examination of Equation 3.2 reveals that the fundamental "driving" term of the cable equation is not simply V_e, but rather is proportional to the second spatial difference

[10] As mentioned in Section 3.2 the methods used in the analysis are generic, allowing for a detailed representation of electrode characteristics if desired. For the first attempt at electrode placement, however, we decided to forgo the added level of complexity.

of V_e, namely $V_{e_{(n-1)}} - 2V_{e_{(n)}} + V_{e_{(n+1)}}$. For this reason, Rattay [37, 38, 39, 59] termed the second spatial difference of the extracellular potential the "activating function", formally defined as

$$f = V_{e_{(n-1)}} - 2V_{e_{(n)}} + V_{e_{(n+1)}} \tag{3.26}$$

The activating function is a method suggested to simplify the computations involved in determining the response of nerves to applied fields generated by extracellular electrodes. The function describes the sources that drive a nerve fiber, and has been used to predict sites of action potential (AP) initiation and relative electrode stimulation efficiency. Furthermore, the activating function has been used to verify trends in nerve stimulation such as anode blockade [27]. Normalized plots of the activating function for a monopolar anode, monopolar cathode, and longitudinal dipole can be found in Appendix C, Figures C-3 and C-4.

To initiate an action potential (AP), a nerve fiber must be depolarized such that the change in membrane potential from rest is positive in the region of excitation. From Equation 3.2, we see that $\frac{dV_m}{dt}$ is positive when $f > 0$. Therefore a positive activating function is a necessary (but not sufficient) condition for AP generation. The level of membrane depolarization is determined by the strength of the activating function. However, the activating function threshold for nerve firing is not well defined. Rattay's work focuses on using the activation function to explain observed and simulated phenomenon, not as a tool to predict nerve firing behavior. Meier [28] suggested that the threshold be weighted by the ratio of the membrane time constant to the pulse width

$$f > V_{Thres}\frac{R_m C_m}{T} \tag{3.27}$$

where R_m is the reciprocal of G_m and T is the pulse width. Meier used a generic value of $20\,mV$ for V_{Thres}. The value of the threshold is intrinsically coupled to the pulse width and fiber dimensions, however Meier's formulation does not take them into account.

The threshold value of the activating function used in this work is determined by the strength-duration curve (Section B.3.2) of the nonlinear SEF model described in the next section. The injected threshold current needed to excite a single node (I_{node}), as seen in Figure B-3, is $1.388\,nA$. We can equate this threshold with the activating function in Equation 3.2 as follows

$$\begin{aligned} G_a(V_{e_{(n-1)}} - 2V_{e_{(n)}} + V_{e_{(n+1)}}) &\geq I_{node} \\ V_{e_{(n-1)}} - 2V_{e_{(n)}} + V_{e_{(n+1)}} &\geq \frac{I_{node}}{G_a} \\ f &\geq \frac{I_{node}}{G_a} \\ f &\geq \frac{1.388\,nA}{G_a} \end{aligned} \tag{3.28}$$

where $G_a = \frac{\pi D^2}{4\rho_a L}$ is the axoplasmic conductance $[S]$. With this formulation, the activating function threshold ranges from a minimum of $12.4\,mV$ for a fiber diameter of $D = 10\,\mu m$ to a maximum of $124\,mV$ for a fiber of diameter $D = 1\,\mu m$.

SEF Model

A second, more detailed circuit model of a nerve fiber incorporating nonlinear ionic channel dynamics was used to determine nerve fiber excitation thresholds in addition to the activating function, which is based on a linear circuit model. The model used in this work is based on mammalian myelinated fibers as described by Frijns *et al* [60]. The Frijns model is based upon the work of Schwarz and Eikhof, who first measured and quantified action potentials and membrane currents in myelinated fibers (from the rat and cat) at 37° C, body temperature [61]. The resultant Schwarz-Eikhof-Frijns (SEF) model describes *in vivo* neural properties relevant for electrical prostheses design better than previously published models [60], and has been used to determine excitation thresholds for a cochlear implant model [48].

Model Description

A section of the SEF model is shown in Figure 3-9 that is conceptually similar to the linear model (Figure 3-1) discussed in Section 3.1.2. The membrane currents at each node include a capacitive current (I_C), leakage current (I_L), and ionic currents (I_{ion}) consisting of a nonlinear sodium current (I_{Na}) and a nonlinear potassium current (I_K). The myelin is treated as a perfect insulator, allowing only axial current flow between adjacent nodes. Table 3.2 lists a summary of relevant parameters, and a more detailed description can be found in Appendix B.

The deviation of the membrane potential (V_m) from rest can be found by conservation of current at the n^{th} node

$$\begin{aligned} C_m \frac{d V_{m_{(n)}}}{dt} + G_L(V_{m_{(n)}} - V_L) &- G_a(V_{m_{(n-1)}} - 2V_{m_{(n)}} + V_{m_{(n+1)}}) \\ &= G_a(V_{e_{(n-1)}} - 2V_{e_{(n)}} + V_{e_{(n+1)}}) - I_{ion_{(n)}} \end{aligned} \quad (3.29)$$

yielding a cable equation very similar to Equation 3.2. The leakage equilibrium potential (V_L) is chosen such that zero transmembrane current flows at rest, that is $I_L + I_{ion} = 0$. The resting membrane voltage is calculated using the Goldman Equation, as described in Appendix B.1. It should be noted that all potentials are referenced to a far-field ground.

The values of the extracellular potential ($V_{e_{(n)}}$) are determined by sampling the calculated potential field in the volume conductor at the nodes of Ranvier. As mentioned in Section 3.1.3, the values of the extracellular potential are determined solely from the properties of the volume conductor, namely the stimulus strength, tissue conductivity, and electrode configurations. Consequently, fiber kinetics of the SEF model do no influence the extracellular potential.

The model contains nonlinear sodium (G_{Na}) and potassium (G_K) conductances that give rise to nonlinear currents. The governing equations for the sodium and potassium currents are:

$$I_{Na_{(n)}} = \left[P_{Na} h_{(n)} m_{(n)}^3 \left(\frac{V_{m_{(n)}} F^2}{RT} \right) \frac{[c_{Na^+}^o] - [c_{Na^+}^i] \exp\left(\frac{V_{m_{(n)}} F}{RT} \right)}{1 - \exp\left(\frac{V_{m_{(n)}} F}{RT} \right)} \right] \cdot \pi dl \quad (3.30)$$

$$I_{K_{(n)}} = \left[P_K n_{(n)}^2 \left(\frac{V_{m_{(n)}} F^2}{RT} \right) \frac{[c_{K^+}^o] - [c_{K^+}^i] \exp\left(\frac{V_{m_{(n)}} F}{RT} \right)}{1 - \exp\left(\frac{V_{m_{(n)}} F}{RT} \right)} \right] \cdot \pi dl \quad (3.31)$$

using the conventions

P_{Na}	Sodium Permeability
P_K	Potassium Permeability
$m_{(n)}$	Sodium Activation Factor
$h_{(n)}$	Sodium Inactivation Factor
$n_{(n)}$	Potassium Activation Factor
$[c_{Na^+}^o]$	Extracellular Sodium Concentration
$[c_{Na^+}^i]$	Intracellular Sodium Concentration
$[c_{K^+}^o]$	Extracellular Potassium Concentration
$[c_{K^+}^i]$	Intracellular Sodium Concentration
F	Faraday's Constant
R	Ideal Gas Constant
T	Absolute Temperature

The activating factors $m_{(n)}$ and $n_{(n)}$ and the inactivating factor $h_{(n)}$ are nonlinear, time-varying, and voltage dependent and obey a first-order differential equation of the form

$$\frac{dm_{(n)}}{dt} = \alpha_{m_{(n)}} - (\alpha_{m_{(n)}} + \beta_{m_{(n)}}) m_{(n)} \quad (3.32)$$

The voltage and temperature dependence of the rate constants $\alpha_{m_{(n)}}$ and $\beta_{m_{(n)}}$ as well as the equations that govern $n_{(n)}$ and $h_{(n)}$ are described in Appendix B.1.

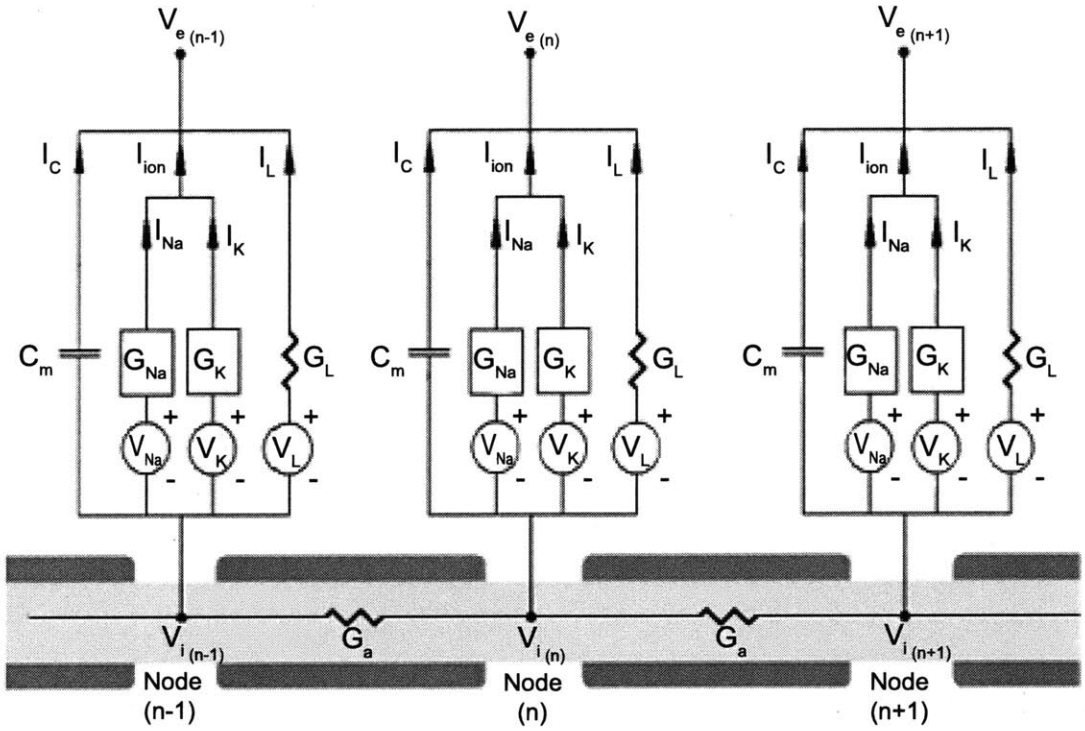

Figure 3-9: Nonlinear Circuit Model of the Nerve [48], Modified: Shown are three nodes of Ranvier with transmembrane currents consisting of a capacitive current (I_C), ionic current (I_{ion}), and leakage current (I_L). The extracellular potentials at each node ($V_{e,n}$) are determined by the potential field in the volume conductor, as described in Sections 3.2.2 and 3.2.3. The nonlinear, voltage-dependent kinetics of the sodium conductance (G_{Na}) and potassium conductance (G_K) are taken from Schwarz and Eikhoff [61]. See Table 3.2 and Appendix B.2 for parameter conventions.

Symbol	Parameter	Value	Units
D	Fiber Diameter	1–10	μm
d	Axon Diameter	$0.7D$	μm
l	Node of Ranvier Length	2.5	μm
L	Internodal Distance	$100D$	μm
ρ_a	Axoplasmic Resistivity	0.70	Ωm
c_m	Unit Area Membrane Capacitance	0.02	$\frac{F}{m^2}$
g_L	Unit Area Leak Conductance	728	$\frac{S}{m^2}$
G_a	Nodal Conductance	$\frac{\pi D^2}{4\rho_a L}$	S
C_m	Membrane Capacitance	$c_m \pi dl$	F
G_L	Leakage Conductance	$g_L \pi dl$	S

Table 3.2: Summary of Parameters

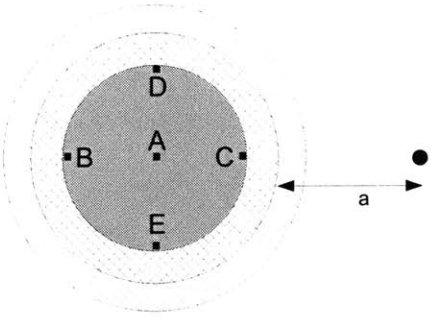

Figure 3-10: Nerve Fiber Interpolation for the Inferior Vestibular Nerve: Cross-section of the IVN showing five locations where nerve fibers were simulated. The longitudinal potentials in locations **A**–**E** were interpolated from the volume conductor and used to drive the nonlinear SEF model. The • denotes the position of the electrode with relation to the nerve bundle. The electrode-to-nerve distance, **a**, is taken from the electrode to the outside of the nerve.

Numerical Simulation

The NEURON Simulator [62] (version 5.9, N.T. Carnevale and M.L. Hines), henceforth referred to simply as NEURON, was used to model the nonlinear dynamics of the SEF model and was chosen for it convenience and efficiency in modeling biological systems. NEURON provides a highly programmable environment that separates membrane kinetics from fiber geometry, allowing for efficient model generation and geometry parameterization. Furthermore, the simulator provides a robust numerical engine that supports a variety of integration schemes (both explicit and implicit).

The SEF model was coded in the NMODL language and compiled for computational efficiency. The model was then available to include in simulation scripts run through NEURON's HOC interpretor. For each electrode configuration in Figures 3-7 and 3-8, the extracellular potentials (V_e) calculated in the volume conductor were interpolated at five locations for the IVN case as seen in Figure 3-10. For the SVN case, only the center interpolation point (**A**) was used. The • represents an electrode located a distance, **a**, away from the nerve.

A nerve fiber consisting of 50 nodes was simulated at each interpolation location for 10 fiber diameters ranging from 1–10 μm. The internodal length (L) is proportional

to the fiber diameter (D) through the relation $L = 100D$, giving an internodal length range of $100\,\mu m$ to $1\,mm$. Since our nerve model length was $5\,mm$ for the IVN case, the number of nodes ranged from 50 for $D = 1\,\mu m$ to 5 for $D = 10\,\mu m$. For simplicity, 50 nodes were simulated for each fiber diameter; however, in the case of fiber diameters of 2–$10\,\mu m$ where less than 50 nodes were required, the additional nodes were left undriven. That is, $V_{e_{(n)}}$ for the excess nodes was set to zero. The SVN case was handled in the same manner.

The values of V_e were sampled at nodes of Ranvier ($V_{e_{(n)}}$) and were used to drive[11] Equations 3.29-3.31, where we seek a solution to the membrane voltage ($V_{m_{(n)}}$) at each node as a function of time to determine the existence of a propagating action potential. Note that we only need to simulate $V_{m_{(n)}}$, $m_{(n)}$, $h_{(n)}$, and $n_{(n)}$ as functions of time, since other model parameters can be derived from these four values and the fiber dimensions.

The system is driven by a time-varying vector of extracellular potentials, $V_{e_{(n)}}$, sampled at the nodes of Ranvier. The driving function takes the form of a monophasic pulse of width $200\,\mu s$. The pulse width was chosen based on the strength-duration curve for the SEF model (See Appendix B.3.2). At pulse widths greater than $200\,\mu s$, the excitation threshold approaches the rheobase, or minimum value. We are interested in the *minimum* threshold currents necessary for nerve excitation for six electrode configurations (Figures 3-7 and 3-8) and various electrode-to-nerve distances. The effect of pulse width on threshold behavior is left for another study.

Since the potential field calculation is a linear process, the values of $V_{e_{(n)}}$ were only calculated once for a stimulus current of $I = 1\,\mu A$. To find threshold behavior, the interpolated vectors of $V_{e_{(n)}}$ were scaled using a binary search algorithm and used to drive the SEF model to find the threshold stimulus current necessary to initiate a propagating action potential. During the stimulus phase, the driving function took the form

[11]The extracellular potentials were converted into equivalent intracellular currents [46, 47] for implementation in NEURON.

$$V^d_{e_{(n)}}(t) = \begin{cases} C_{scale} \cdot V_{e_{(n)}} & 0 < t \leq 200\,\mu s \\ 0 & 200\,\mu s < t \leq 3\,ms \end{cases} \tag{3.33}$$

where C_{scale} was iteratively determined by the binary search algorithm. When $C_{scale} \cdot V_{e_{(n)}}$ caused a propagating action potential in the numerics (as described below), the threshold stimulus current was simply $I_{threshold} = C_{scale} \cdot 1\,\mu A$.

The system of Equations 3.29-3.31 was solved implicitly using the Crank-Nicholson method for a duration of $3\,ms$ with a fixed time step of $25\,\mu s$. A fiber was said to have "fired" when a propagating action potential was observed in the numerics. The existence of a propagating action potential was determined by monitoring the values of the sodium activation factor, $m_{(n)}$, at various nodes at the center and ends of the simulated fiber. When the value of $m_{(n)}$ for $n = 0, 1, 25, 48$, and 49 exceeded 0.8, a propagating action potential was guaranteed to have occurred. The process was repeated for each electrode configuration and electrode-to-fiber distance.

3.3 Design Approach

The approach used to determine electrode placement for the nerve model was as follows: current-distance relations for the range of fiber diameters (D = 1–10 μm) and interpolation locations (**A**–**E**) were calculated for the six electrode configurations shown in Figures 3-7 and 3-8. For simplicity, the focus was on three fiber diameters (D = 1,5,10 μm) and the most detailed combination of volume conductor and biophysical model, namely the anisotropic/inhomogeneous volume conductor and the SEF nonlinear model. The best electrode configuration and location was first determined for the IVN case; the SVN case was treated as a superposition of two IVN cases and thus the IVN results were used to guide the placement of electrodes in the SVN case. Finally, the simpler volume conductor and biophysical model (isotropic/homogeneous volume conductor and activating function) were compared against their more detailed counterparts.

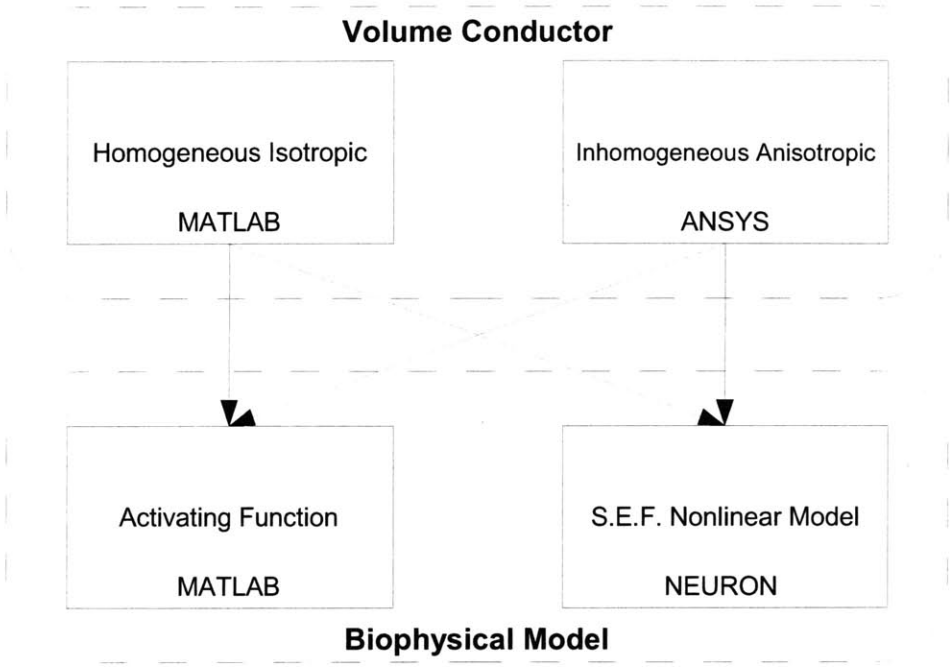

Figure 3-11: Block Diagram of Modeling Data Flow

3.3.1 Data Flow

Figure 3-11 recaps the the simulation data flow used in the model. The electric potential distribution for a stimulus electrode configuration is first calculated in a volume conductor. An analytic solution was solved in Matlab (version 7.0.1, Mathworks, Inc.) for the monopolar electrode configuration in a homogeneous and isotropic volume (See Section 3.2.3) . The finite element package Ansys (version 9.0, Ansys, Inc.) was used to solve for the potential distribution in an anisotropic and inhomogeneous volume (See Section 3.2.3) for all six electrode configurations in Figures 3-7 and 3-8.

The arrows in Figure 3-11 indicate the flow of data from the volume conductor to the biophysical models. All data transfer between models was done using custom scripts that passed data stored in ASCII files. The activating function calculations (See Section 3.2.4) were performed in Matlab, while the SEF nonlinear model (See Section 3.2.4) was implemented in the NEURON simulator (version 5.9, N.T. Carnevale and M.L. Hines).

3.3.2 Visualization Flow

A method of visualizing the nerve geometries, potential fields, and activating function in three-dimensions was also created. The rationale for the development was to simplify the display of 3D-data that is difficult to conceptualize in 2D-plots. The tool serves as an aid for presentations and may also help surgeons visualize the placement of electrodes prior to surgery.

Figure 3-12 shows the data flow for the visualization package. The nerve geometries and potential field are first sent from Ansys to Amira[12] (version 3.1.1, Mercury Computer Systems, Inc.) in a standard AVSUCD format. All layers of the inhomogeneous nerve are transfered to Amira, and the viewer can toggle between the layers or view them simultaneously. The potential field is then sampled in a uniform grid in Ansys before being sent to Matlab to calculate the activating function. The field must be interpolated because the solution in Ansys only exists at the finite element node locations which are not arranged in a uniform grid. The sampled potential solution and corresponding activating function are sent from Matlab to Amira for display. Amira overlays the potential field, activating function, and nerve geometry, so the viewer is able to see them simultaneously or is able to toggle them on or off individually. The field and activating function can be displayed as isosurfaces in three-dimensions or as isocontours on a single or multiple planes. Amira also allows for rotation, zoom, and video capture of the 3D space.

[12]Amira is a visualization and segmentation program commonly used for medical imaging.

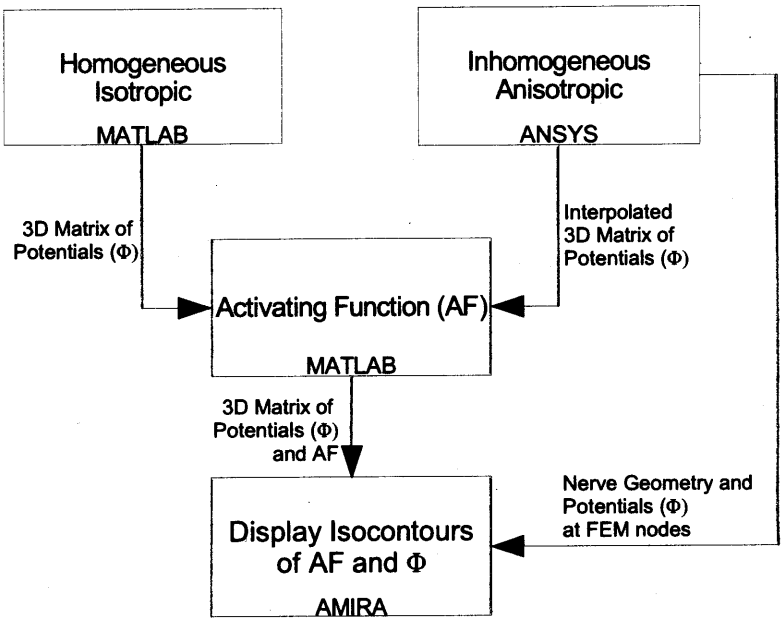

Figure 3-12: Block Diagram of Visualization Data Flow

Chapter 4

Results and Discussion

This chapter presents and discusses simulation results with an emphasis on the most detailed models studied, namely the inhomogeneous, anisotropic volume conductor and the nonlinear nerve model. The individual model results are presented in Section 4.1. Section 4.2 focuses on the current-distance relations derived from the individual component results and compares thresholds for the various electrode configurations. Suggestions for electrode placement are discussed in Section 4.3, and the topic of validation is covered in Section 4.4. Finally, the detailed methods used to determine the potential field and nerve threshold behavior are compared with the simplified homogeneous isotropic volume and the activating function in Section 4.5.

4.1 Model Component Results

4.1.1 Potential Field

All simulations were conducted on a computer with an Intel Pentium 4, 3.2 GHz processor and 4 GB of physical memory running Microsoft Windows XP (SP2). The potential field was calculated using Ansys, and a mesh convergence study was conducted to determine the balance between solution accuracy and computation time, as described in Appendix A.2. The solution for a single electrode placement solved in roughly 30 seconds, and the 50 load steps required to analyze an electrode-to-nerve

distance of 5 mm took approximately 30 minutes to complete.

The electrode-to-nerve distance was varied from 0.1 mm to 5 mm in 0.1 mm increments for each electrode configuration seen in Figures 3-7 and 3-8. All electrodes were driven at a magnitude of 1 μA, except the flanking electrodes in the tripolar configuration that were driven at half that magnitude to insure zero net current. Furthermore, the electrode separation in Configurations 3–6 was held constant at 1 mm. The choice to fix the electrode separation distance was made to reduce the parameter space, and the value of 1 mm was chosen with regard to practical electrodes[1] as well as for its prevalence in other simulation studies.

Figure 4-1 shows a contour plot of the potential field generated by a monopolar anode (electrode configuration 1) as viewed in Amira.[2] The lines displayed indicate contours of equipotential in the plane of the electrode that is located a distance 0.1 mm away from the inferior vestibular nerve. The contours radiate outward from the electrode and correspond to increasingly smaller values of potential. Due to the anisotropic conductivity of the nerve tissue, the isocontour pattern radiating away from the source is not circular.

Amira provides a powerful interface for viewing the potential and activating function as isocontours on any desired plane or even as three-dimensional isosurfaces. However, the visualization process flow (Figure 3-12) involves many steps and the interpolation routine in Ansys is computationally intense, requiring several minutes to complete. Therefore, the visualization tools were used primarily to illustrate individual case results. To derive the threshold results for each electrode configuration and electrode-to-nerve distance, the visualization process was forgone and only certain potentials within the nerve were considered.

For each electrode distance, the potential field was interpolated along five paths within the nerve (Figure 3-10) for the inferior vestibular nerve (IVN) case. For the superior vestibular nerve (SVN), only the potentials along the center of each branch

[1] A common stimulating electrode is created by flame forming a spherical ball at the tip of a platinum wire. For a typical wire of diameter 128 μm, a reasonable estimate of the spherical diameter would be 150–200 μm.

[2] For details of the visualization tools used, see Section 3.3.2.

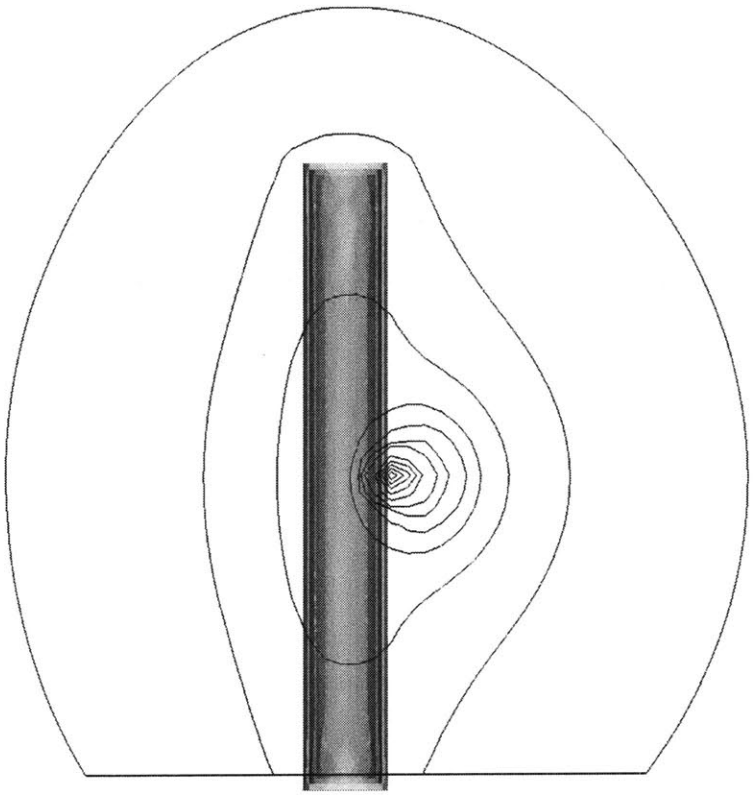

Figure 4-1: Isocontours of the Potential Field from a Monopolar Anode as seen in Amira: Shown is the field generated by a monopolar anode located $0.1\,mm$ from the IVN. The contour is a slice down the center of the nerve in the x-z plane where the electrode is placed. Note the three layers that comprise the IVN: the center nerve tissue, intermediate epineurium sheath, and outer saline layer.

were interpolated. It was assumed at each path location there existed a nerve fiber with a diameter between $D = 1\,\mu m$ and $D = 10\,\mu m$. The linear dependence between internodal distance (L) and fiber diameter (D), $L = 100D$, dictated that the potential along the paths was interpolated at a resolution of $0.1\,mm$, the node of Ranvier spacing for a fiber of diameter $D = 1\,\mu m$.

Figure 4-2 shows the potential along path $\mathbf{A}$[3] for each electrode configuration located a distance of $0.1\,mm$ away from the nerve. Several interesting trends can been seen in the figure, including the symmetry between the fields from Configurations 1

[3]For the definition of paths **A**–**E**, see Figure 3-10.

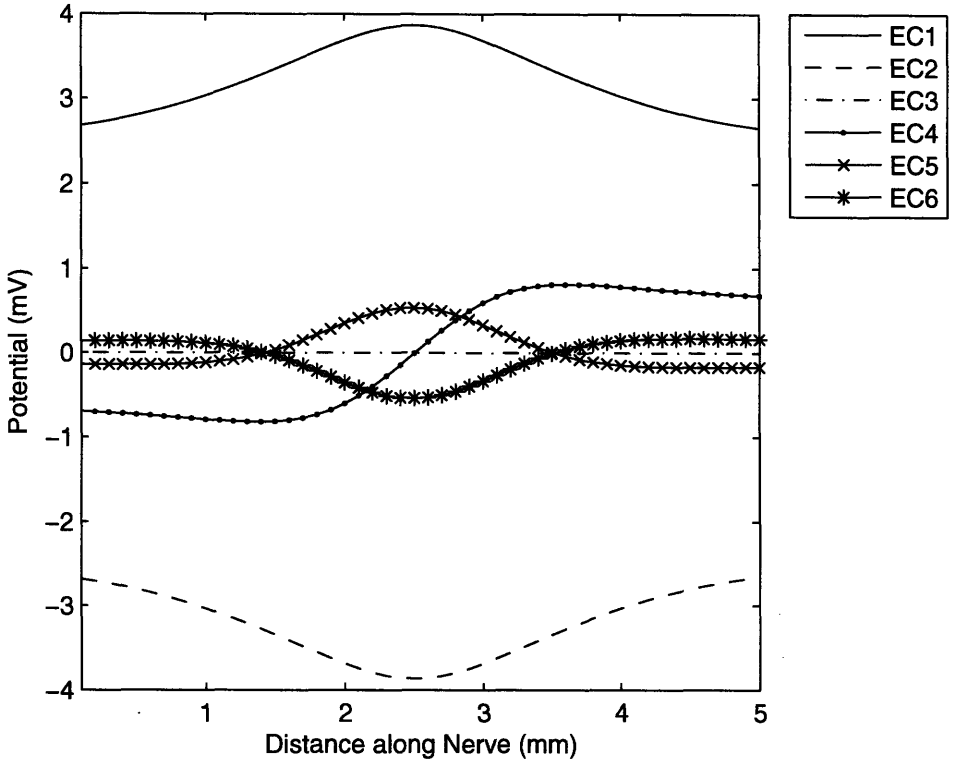

Figure 4-2: Potential Field along Path **A** for Six Electrode Configurations located $0.1\,mm$ from the IVN. **EC1**: Electrode Configuration 1, **EC2**: Electrode Configuration 2, *etc.* Note: Increasing distance along the nerve corresponds to more distal locations.

and 2 as well as Configurations 5 and 6. The field patterns are additive inverses of each other, a result of the linearity of the field calculation. Furthermore, the shape of the fields generated by the tripoles (Configurations 5 and 6) closely resemble the fields of their central electrode (Configurations 1 and 2, respectively) with a lower magnitude. The result can be explained by the effective reduction of central electrode strength by the weaker flanking electrodes of opposite polarity.

As expected, the magnitude of the field generated by Configuration 3 is zero since path **A** lies equidistant from electrodes of opposite polarity. In fact, the potential at paths **D** and **E** is also zero for Configuration 3 because they lie on the same equipotential plane as path **A**. Representative graphs of the potential at paths **B**–**E** for each electrode configuration at a distance of $0.1\,mm$ can be found in Appendix C,

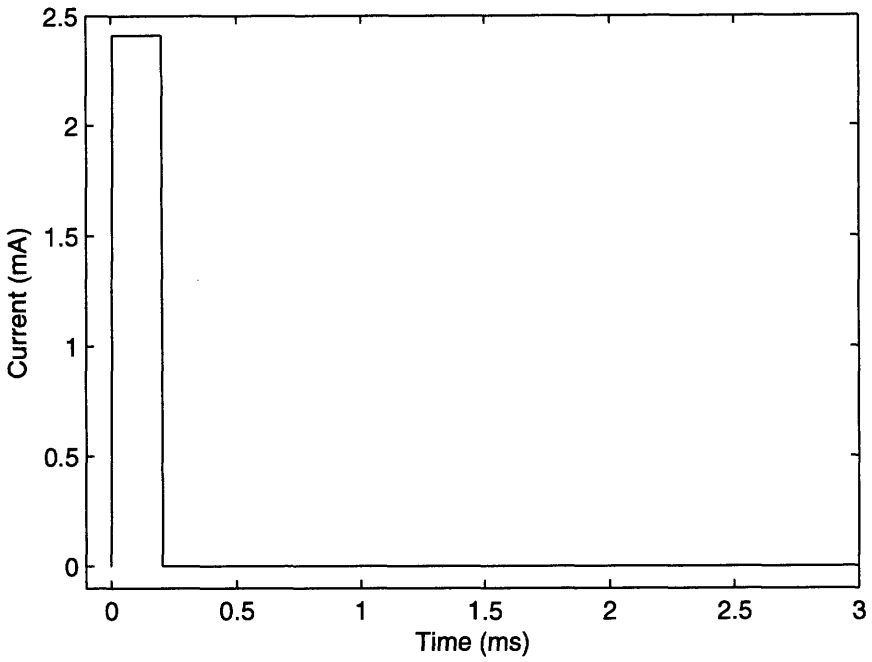

Figure 4-3: Suprathreshold Stimulus Waveform for Monopolar Anode: Shown is a $200\,\mu s$ stimulus with $C_{scale} = 2410$.

Supplemental Results.

4.1.2 SEF Model

Computing the threshold estimates in NEURON for the ten fiber diameters $D = 1$–$10\,\mu m$ at five path locations **A**–**E** (a total of 50 fibers) took approximately 30 seconds for each electrode-to-nerve distance; it took approximately 30 minutes to analyze the full $5\,mm$ electrode distance range. Figures 4-3 and 4-4 illustrate a typical simulation for a monopolar anode located $1\,mm$ away from the inferior vestibular nerve.

Figure 4-3 shows a stimulus current waveform of a monopolar anode (electrode configuration 1) driven with a suprathreshold current of $2.410\,mA$, resulting from a C_{scale} value of 2410 calculated from the binary search algorithm. The resulting potential distribution $V_{e_{(n)}}$ at path **C** along the IVN can been seen in Figure 4-4**A**. Shown is the scaled extracellular potential sampled at the nodes of Ranvier[4] for a

[4]Precisely the driving function, $V^d_{e_{(n)}}(t)$, in Equation 3.33.

fiber of diameter $D = 1\,\mu m$, where $n = 0$ is the most proximal node and $n = 49$ is the most distal node.

The response of the fiber to the suprathreshold stimulus can been seen in Figure 4-4**B**. Before the onset of the stimulus, the value of V_e is zero for all nodes and V_i equals the resting value of $-84.6\,mV$. Therefore V_m, the deviation from rest, is precisely zero for all nodes. At the onset of the pulse we see the effect the activating function, or second-spatial derivative of the potential, has on eliciting nerve firing. Regions in the center of the nerve (near node $n = 25$) are hyperpolarized, while regions at the ends of the nerve are depolarized, as predicted by the activating function for an anode (Figure C-3). The nodes reach their maximum value of depolarization or hyperpolarization at the end of the $200\,\mu s$ pulse. We see at the end of the pulse, node $n = 0$ is sufficiently depolarized to cause an action potential. From the symmetry of the nerve model and applied field, we would expect both node zero and node forty-nine to initiate an action potential. However, the since the solution to the potential is numerically calculated, it is likely that variations in potential exist at these nodes. Therefore, for this particular model run, the action potential propagated from node zero to node forty-nine.

The maximum deviation of the membrane potential from rest is $115.88\,mV$, corresponding to the space-clamped action potential for the SEF node (Figure B-4**A**). Furthermore, the action potential propagates down the nerve with velocity $v = 4.673\,\frac{m}{s}$. In comparison, the conduction velocity for a nerve fiber of diameter $D = 10\,\mu m$ is $v = 47.17\,\frac{m}{s}$. The action potential (AP) conduction velocity is proportional to fiber diameter ($v \propto D$), as expected for myelinated nerve fibers [26].

Figure 4-4**C** shows the response of the fiber to a subthreshold stimulus. The reduced scale more clearly shows the hyperpolarization of the central nodes, where the membrane potential of node $n = 25$ is lowered $11.8\,mV$ from its resting value. At the end of the stimulus pulse, the nodes at the ends of the fiber are depolarized to their fullest extent. V_m at node $n = 0$ increases $31.33\,mV$ and we see the onset of what appears to be an AP, however the stimulus is too weak to generate a propagating AP.

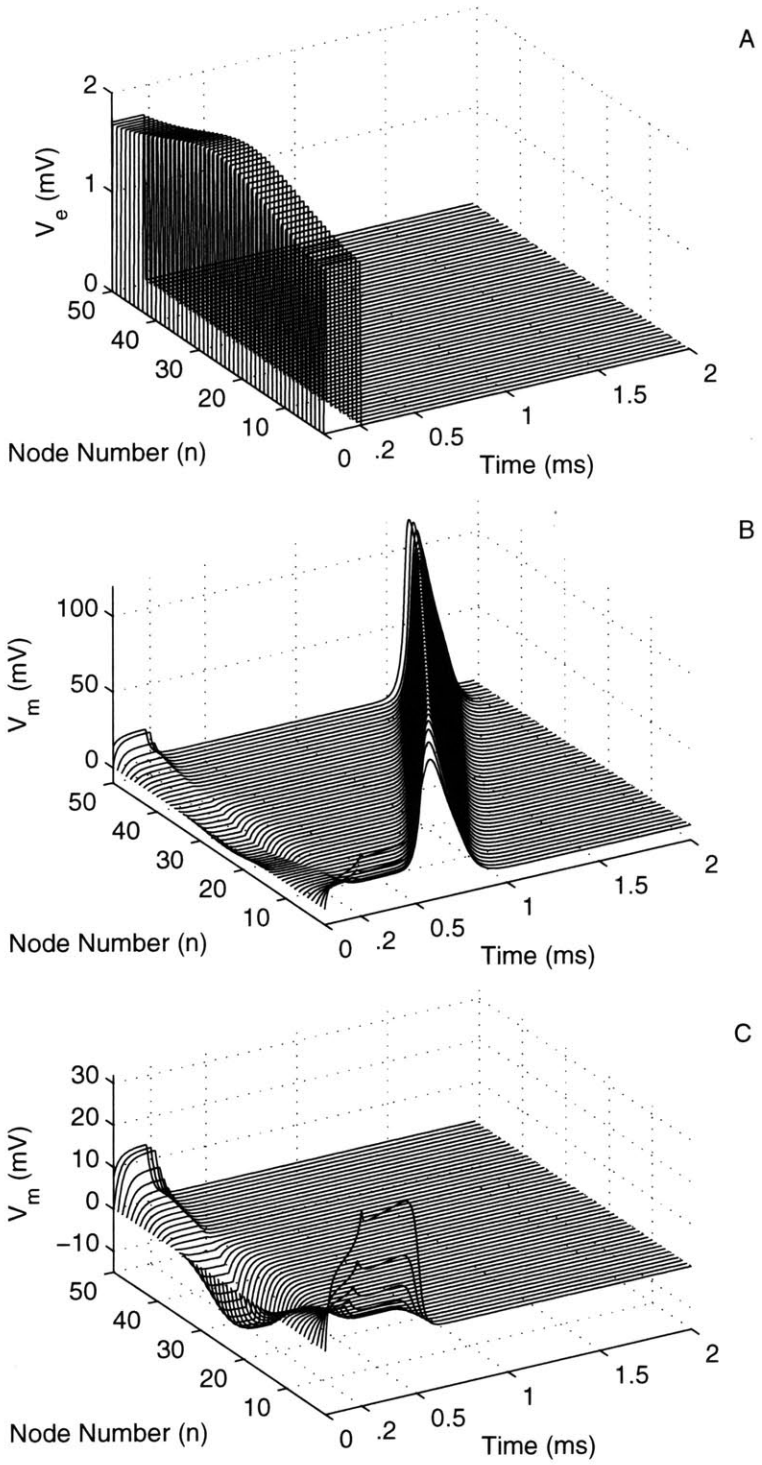

Figure 4-4: Response of a $D = 1\,\mu m$ Nerve Fiber to Supra- and Sub- Threshold Stimuli: **A**, Suprathreshold driving function $V^d_{e_{(n)}}(t)$ for monopolar anode (EC1); **B**, Membrane potential for suprathreshold stimulus; **C**, Membrane potential for subthreshold stimulus. See text for detailed description.

4.2 Current-Distance Relations

Current-distance relationships were obtained by calculating the fiber excitation threshold for each electrode configuration and electrode-to-nerve distance. Results for the inferior vestibular nerve (IVN) case are presented first, followed by the superior vestibular nerve (SVN) results.

4.2.1 Inferior Vestibular Nerve (IVN)

Individual Electrode Configuration Results

For each electrode configuration (EC), current-distance relations were calculated at each interpolation path **A**–**E** for fiber diameters ranging from $D = 1$–$10\,\mu m$. Figure 4-5 shows the thresholds calculated along interpolation path **A** for EC1.[5] We can clearly see the effect of electrode distance on threshold values. As the electrode-to-nerve distance increases, larger currents are necessary to stimulate nerve fibers, regardless of their diameter. This trend is consistent for all electrode configurations simulated. Furthermore, the threshold is approximately proportional to the square of electrode distance for distances greater than $1\,mm$, consistent for myelinated fibers stimulated with extracellular electrodes [40].

We also see that, for a given electrode distance, fibers of smaller diameter require more current to stimulate than fibers of larger diameter. This phenomenon, referred to as the inverse physiological recruitment order [28, 40, 44], can be explained by two nerve fiber properties, namely the internodal distance (L) and axoplasmic conductance (G_a). The internodal distance is proportional to fiber diameter, thus larger fibers have greater differences in extracellular potential at adjacent nodes of Ranvier, or simply put a larger activation function f. Additionally, the axoplasmic conductance is proportional to the square of fiber diameter, implying a higher conductance for larger fibers. From Equation 3.28, we see that increases in both properties lead to a greater driving force to the cable equation, suggesting a proportional weighting in favor of larger myelinated fibers.

[5]Note the current-distance curves are plotted on *log–log* axes.

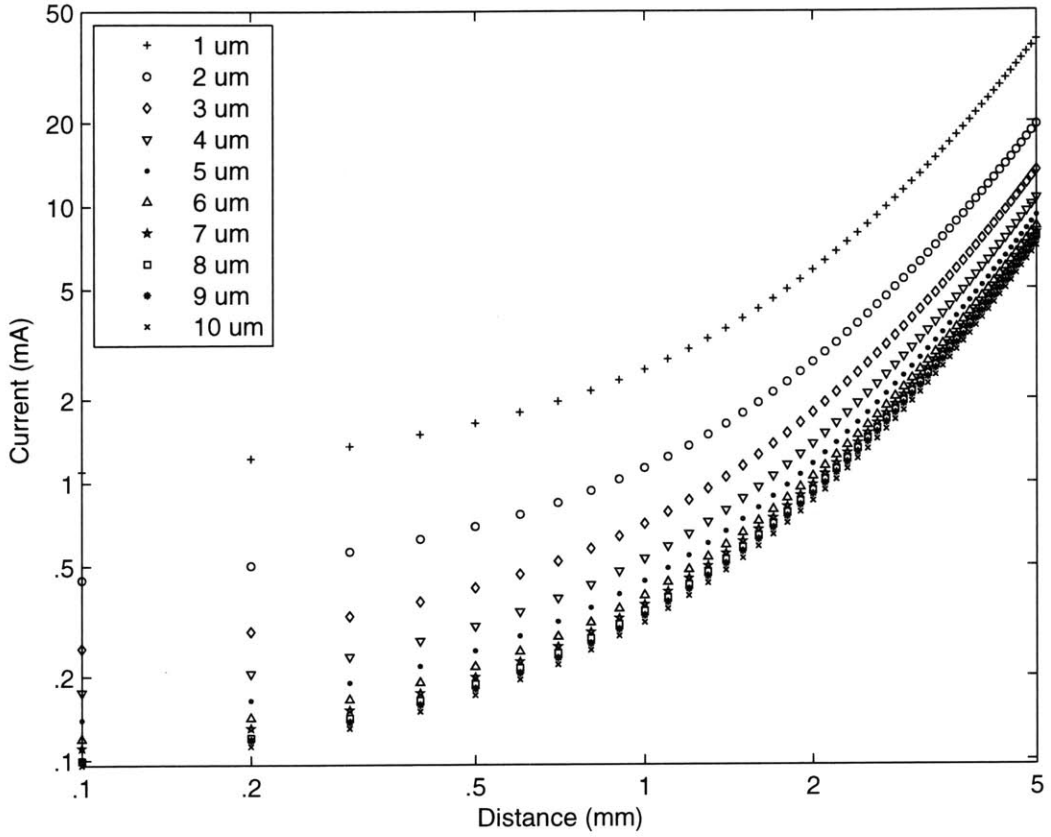

Figure 4-5: IVN Current-Distance Relations for Electrode Configuration 1, Interpolation A

Recall from Section 2.1.1 that vestibular nerve fibers are categorized as "small", "medium", and "large" based on size. In the context of vestibular stimulation, we are most interested in identifying trends based on these categories of fiber diameter. Therefore the remaining results will focus on three fiber diameters, $D = 1, 5, and\, 10\,\mu m$, to represent each respective category. Figure 4-6 shows the current distance relations for the three fiber diameters parameterized by interpolation path for EC1.

It is clear from the figure that the recruitment order for the interpolation paths remains consistent across fiber diameter. Fibers located at path **C** are easiest to excite, while those located on path **B** are hardest to excite. The result can be explained simply by examining electrode placement. As we recall from Figure 4-5, smaller threshold currents are needed for smaller electrode to nerve distances. For all configurations except EC3, the simulated electrodes are located on the side of the nerve bundle closest to path **C**, and we therefore expect path **C** to have the lowest threshold. For electrode configuration 3, both electrodes are equidistant from the nerve bundle, with the cathode placed on the side of the nerve bundle closest to path **B** and the anode placed on the side closest to path **C**. In this case, nerve fibers along path **B** are easiest to excite. The result is not surprising, as cathodal stimulation tends to be more effective than anodal stimulation, as we shall see in the next section. Incidentally, no excitation occurs at paths **A**, **D**, and **E**, as they lie on an equipotential plane of zero volts.

We notice in Figure 4-6 that the excitation threshold for paths **D** and **E** are identical for all fiber diameters. The result is, not surprisingly, consistent for all fiber diameters. Since paths **D** and **E** are located equidistant from every electrode, we expect the potential distribution, and therefore excitation threshold, to be identical along these paths.

Comparison of Electrode Configurations

Our modeling objective is to examine the *minimum* nerve firing thresholds for the various electrode configurations. As such, we are not concerned with the location

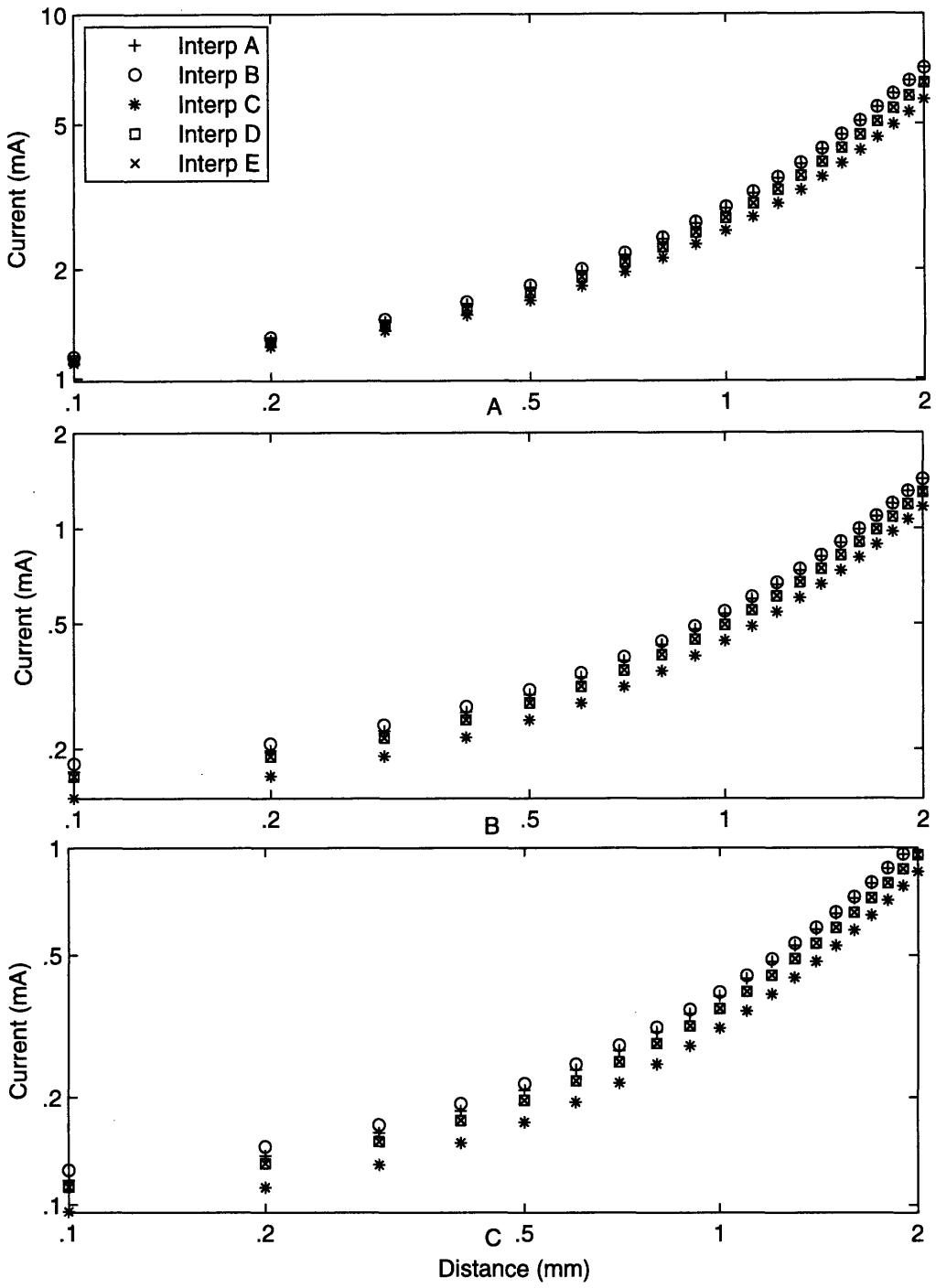

Figure 4-6: IVN Current-Distance Relations for Electrode Configuration 1: **A**, Fiber Diameter $D = 1\,\mu m$; **B**, Fiber Diameter $D = 5\,\mu m$; **C**, Fiber Diameter $D = 10\,\mu m$

in the nerve bundle where excitation is initiated. Therefore, the remaining results will eliminate interpolation path from the parameter space, focusing on minimum thresholds regardless of path. As previously mentioned, minimum thresholds were generally found on path **C** for all electrode configurations except electrode configuration 3, where minimum thresholds were located on path **B**.[6]

Figures 4-7 and 4-8 show current-distance relations for each of the six electrode configurations studied. Interestingly, only configurations 1, 2, and 4 are able to elicit stimulation throughout the full $5\,mm$ range examined, and EC4 can only do so for $D = 5\,\mu m$ and $D = 10\,\mu m$ fibers at distances greater than $1.7\,mm$. Even so, stimulation at these distances is not very practical for the vestibular system. In addition to the potentially unsafe currents involved (e.g. $I \approx 200\,mA$ for EC2 at $5\,mm$), stimulation at such large distances will more than likely lead to adverse effects from stimulation of other nerves in the vicinity. Further discussion on this topic is deferred to Section 4.3, Suggestions for Electrode Placement.

Continuing our examination of Figures 4-7 and 4-8, we can also see that the inverse physiological recruitment order is not strictly obeyed for electrode configurations 2 and 3, as well as configurations 5 and 6. Although the $D = 1\,\mu m$ fibers always maintain the highest thresholds, the recruitment order of $D = 5\,\mu m$ and $D = 10\,\mu m$ fibers is reversed for electrode-to-nerve distances of less than $0.5\,mm$. The result has implications for the selective stimulation of either the phasic (quickly changing) or tonic (slowly changing) components of the vestibular response, and will be addressed later in the section.

Furthermore, electrode configurations 2, 3 and 6 exhibit some outliers in the $D = 10\,\mu m$ trace. These outliers stem from the inability to generate an action potential at the closest path to the electrodes, regardless of stimulus strength. As a result, the binary search algorithm assigns an infinite value to the current, and the minimum threshold is taken from another path. For example, at a distance of $1\,mm$, EC3 is unable to generate an action potential at path **B**. Therefore the minimum threshold is derived from path **C**. Since path **C** is further away from the cathodal stimulus

[6]Exceptions to this trend will be highlighted.

than path **B**, the excitation threshold is slightly higher. Two plausible explanations exist for this behavior: 1) The electrode configuration creates a potential distribution along the path that is either incapable of generating an action potential due to a weak stimulus or blocking phenomenon, or 2) The numerical approximation to the cable equation causes the binary search algorithm to miss the threshold. It was unclear which of the two explanations caused the outliers. However, it was verified that the reversal of the recruitment order for fiber diameters $D = 5\,\mu m$ and $D = 10\,\mu m$ is not attributed to the outlier phenomenon.

Figures 4-9 to 4-11 show IVN thresholds parameterized by electrode configuration for fiber diameters $D = 1, 5$, and $10\,\mu m$. Additionally, relative threshold values at various sampled distances are shown in Table 4.1. The table provides a convenient way of analyzing threshold trends between electrode configurations.[7] For example, one can quickly see that EC4 excited the nerve with the lowest threshold for distances smaller than $0.5\,mm$ for small fiber diameters ($D = 1\,mm$), while EC1 had the lowest threshold at distances greater than $0.5\,mm$. Furthermore, relative differences in electrode strengths can easily be identified; EC6, for example, required 7% more current to excite $D = 1\,mm$ fibers than EC4 for a distance of $0.1\,mm$.

Examination of the threshold values reveals a few trends consistent across all fiber diameters. For small electrode-to-nerve distances, cathodal stimulation (EC2) thresholds were lower than anodal stimulation (EC1) thresholds. The result is consistent from the activation function of both waveforms—cathodal stimuli produce a positive activating function across larger regions along the nerve (Figure C-3). However, for larger electrode-to-nerve distances, a crossover occurred with anodal stimulation having the lowest threshold for $D = 1$ and $5\,\mu m$ fibers and the second-lowest threshold for $D = 10\,\mu m$. Furthermore, the central anode tripole (EC5) and transverse dipole (EC3) were generally the worst performing electrode configurations. For small and medium sized fibers, the longitudinal dipole (EC4) and central cathode tripole (EC6) were the best performing electrodes at small distances, requiring similar threshold currents. For larger fibers, the longitudinal dipole was consistently the lowest thresh-

[7]For reference, absolute threshold values can be found in Table C.1.

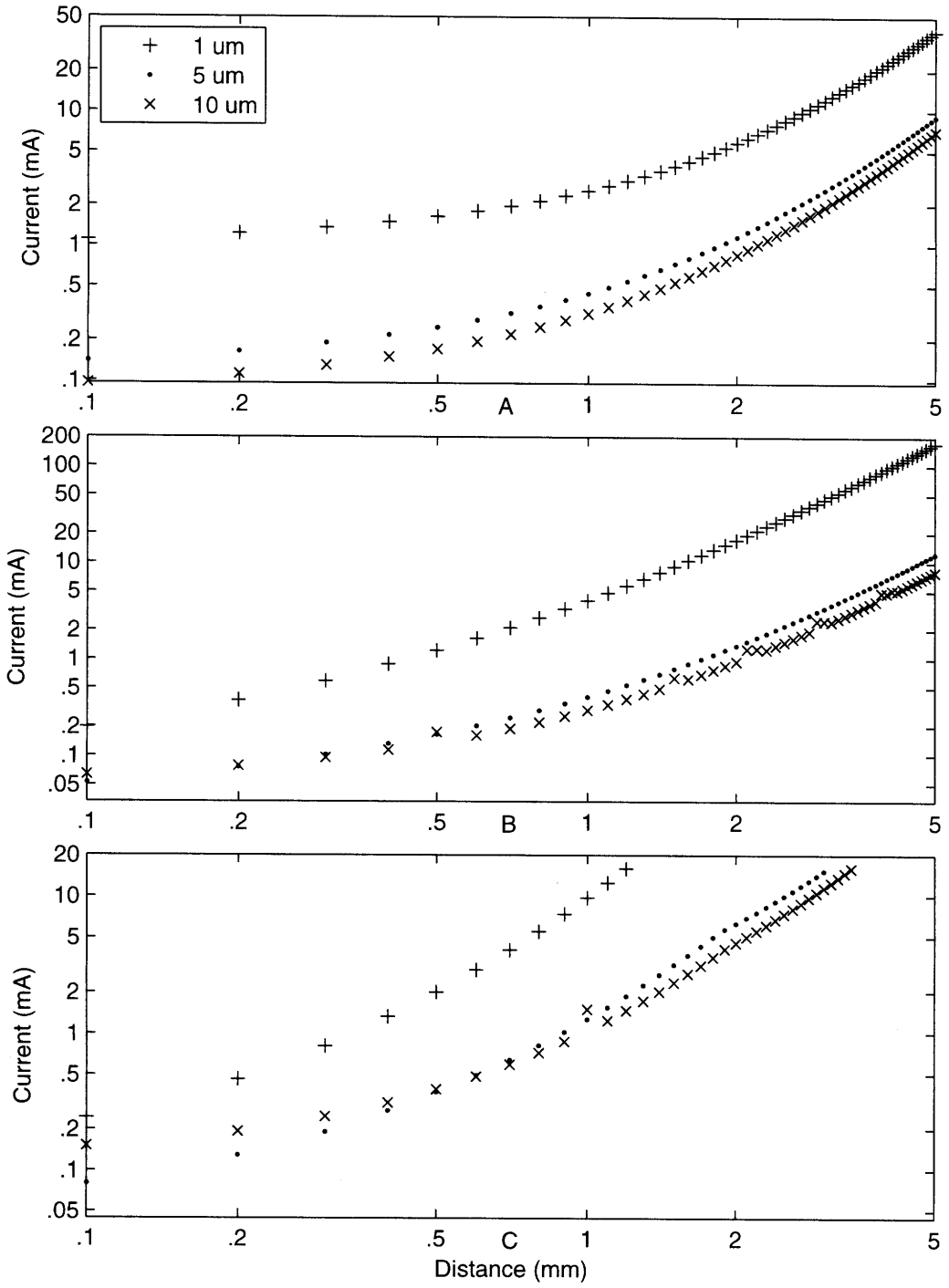

Figure 4-7: IVN Current-Distance Relations for Electrode Configuration 1-3: **A**, Electrode Configuration 1; **B**, Electrode Configuration 2; **C**, Electrode Configuration 3

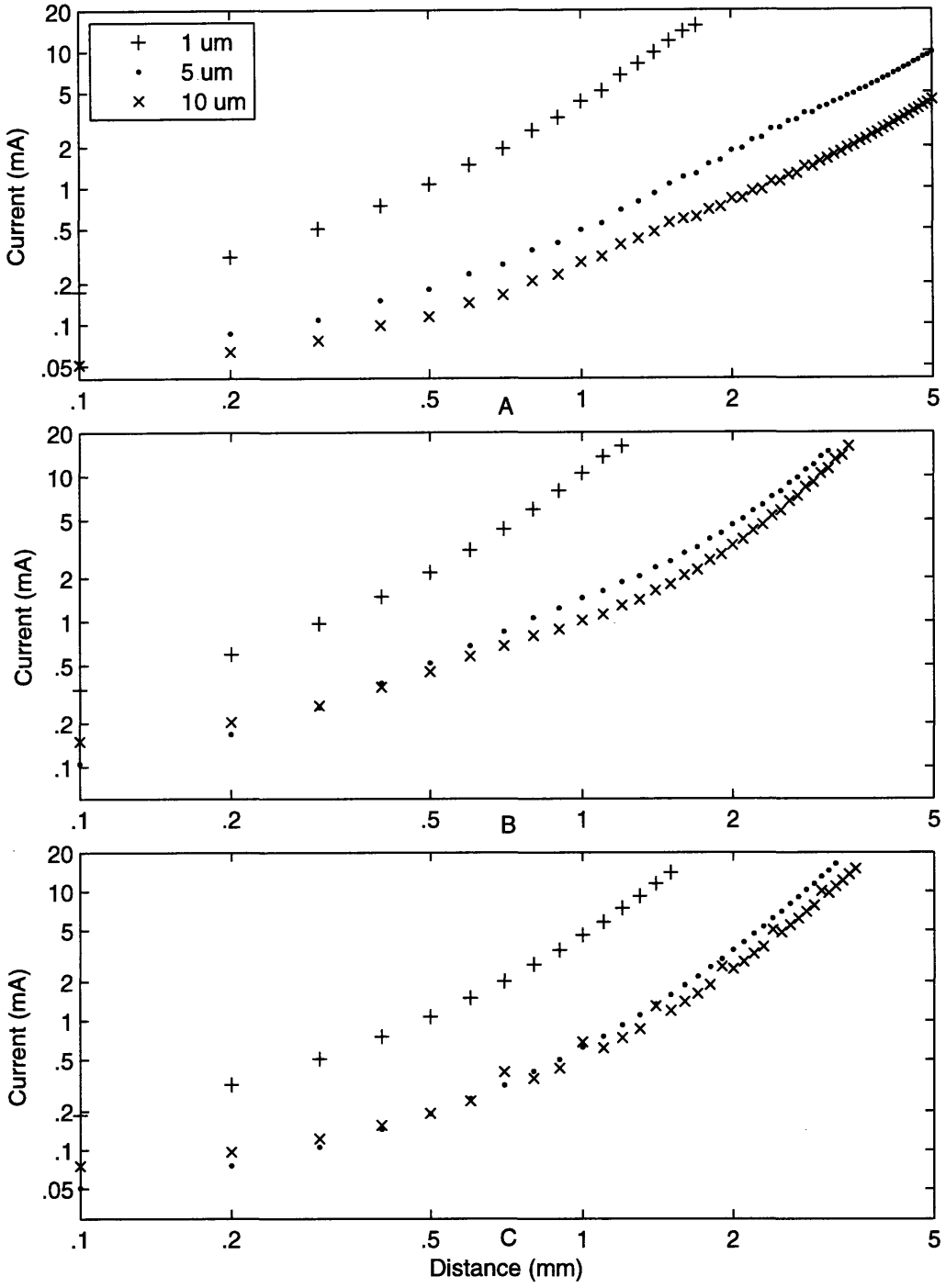

Figure 4-8: IVN Current-Distance Relations for Electrode Configurations 4-6: **A**, Electrode Configuration 4; **B**, Electrode Configuration 5; **C**, Electrode Configuration 6

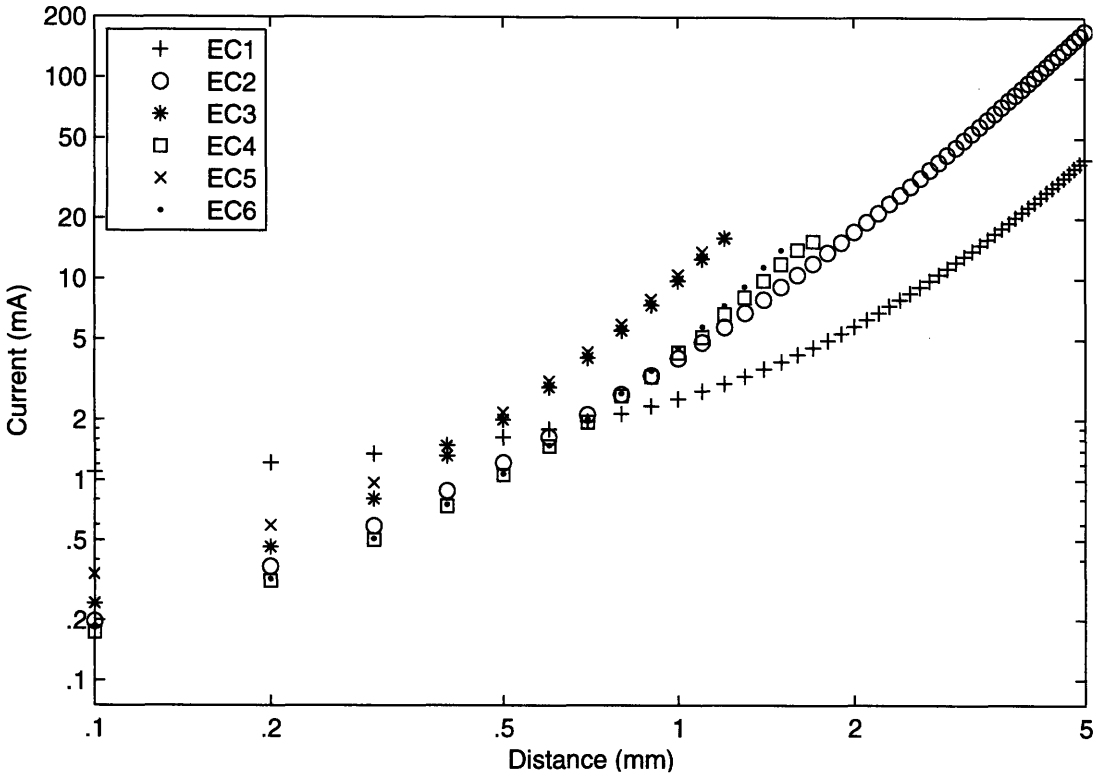

Figure 4-9: IVN Current-Distance Relations for Fiber Diameter $D = 1\,\mu m$

old configuration.

One of the goals for this research was to characterize the threshold behavior of peripheral vestibular nerve fibers across several parameters, including location inside the nerve bundle and fiber diameter. From a strictly scientific standpoint, the data collected and trends observed are quite interesting and novel. However, a secondary goal of the research was to identify a best-case electrode configuration to use in an implanted device. While the data on the individual nerve diameter thresholds may be of later interest for studies concerned with selective stimulation of the phasic or tonic components of the vestibular response[8], they are not of primary interest to our goal of selecting an electrode configuration that simply excites the nerve. In the first design of such a device, the primary metric of interest is to elicit *any* vestibular response, without regard to the specific component being transmitted. Therefore we will now

[8]As described in Chapter 2, larger nerve fibers (to first order) preferentially terminate on Type I hair cells and thus carry the phasic component of the vestibular nerve response. In contrast, smaller fibers preferentially terminate on Type II hair cells and transmit the tonic response [1].

$D = 1\,\mu m$

	0.1 mm	0.2 mm	0.5 mm	1 mm	2 mm	5 mm
EC 1	6.32	3.89	1.54	1.00	1.00	1.00
EC 2	1.13	1.18	1.15	1.58	2.95	4.36
EC 3	1.40	1.47	1.88	3.83	Inf	Inf
EC 4	1.00	1.00	1.00	1.69	Inf	Inf
EC 5	1.95	1.89	2.05	4.10	Inf	Inf
EC 6	1.07	1.02	1.01	1.79	Inf	Inf
Rel. (μA)	174.07	314.49	1062.06	2551.11	5817.68	39364.41

$D = 5\,\mu m$

	0.1 mm	0.2 mm	0.5 mm	1 mm	2 mm	5 mm
EC 1	2.75	2.16	1.49	1.09	1.00	1.00
EC 2	1.04	1.00	1.00	1.00	1.19	1.34
EC 3	1.58	1.70	2.24	3.14	5.43	Inf
EC 4	1.05	1.13	1.09	1.22	1.61	1.07
EC 5	2.07	2.21	3.11	3.59	3.97	Inf
EC 6	1.00	1.00	1.15	1.54	3.01	Inf
Rel. (μA)	50.79	75.69	165.96	404.64	1165.23	9143.25

$D = 10\,\mu m$

	0.1 mm	0.2 mm	0.5 mm	1 mm	2 mm	5 mm
EC1	1.87	1.77	1.50	1.09	1.03	1.61
EC 2	1.25	1.24	1.54	1.03	1.14	1.82
EC 3	2.95	3.04	3.44	5.25	5.50	Inf
EC 4	1.00	1.00	1.00	1.00	1.00	1.00
EC 5	2.93	3.21	3.96	3.55	4.02	Inf
EC 6	1.47	1.53	1.69	2.40	3.01	Inf
Rel. (μA)	51.19	63.20	113.57	286.10	830.79	4398.00

Table 4.1: Relative IVN Threshold Values for $D = 1, 5, 10\,\mu m$ at Various Distances: Threshold values are expressed as a ratio to the minimum threshold at a given distance. The minimum current threshold in microamps (μA) is listed on the last row for each fiber diameter; Values of "Inf" indicate the inability to initiate nerve firing.

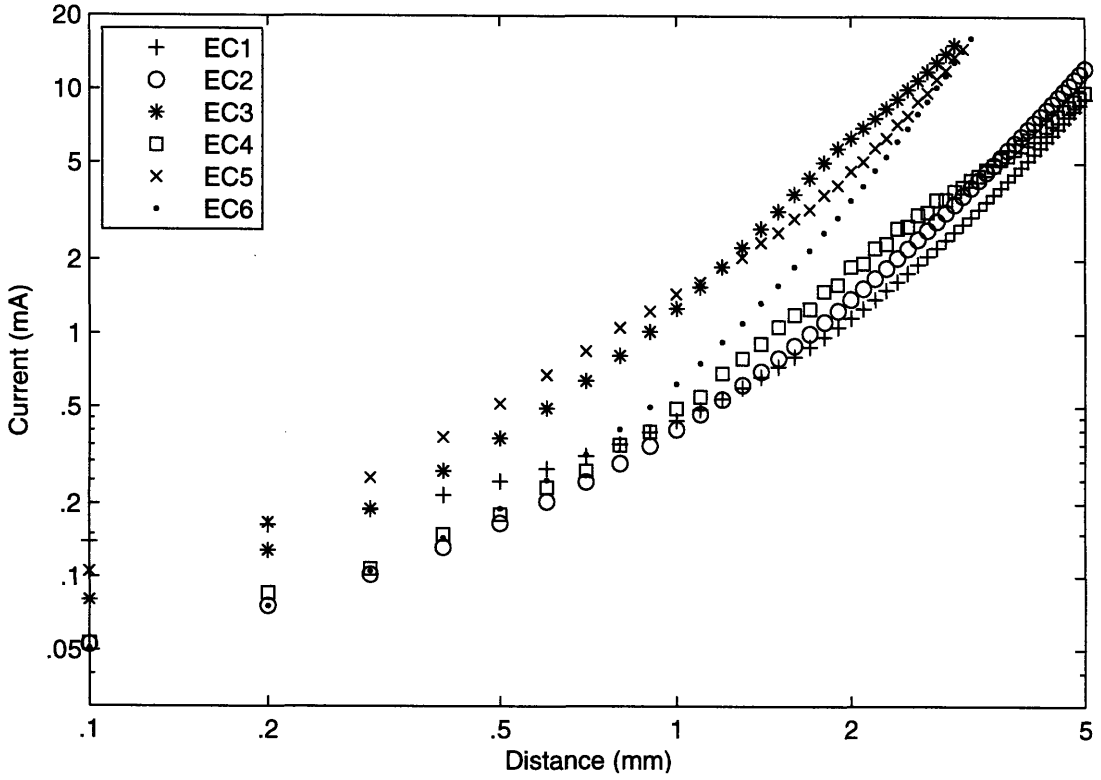

Figure 4-10: IVN Current-Distance Relations for Fiber Diameter $D = 5\,\mu m$

eliminate fiber diameter from the parameter space and simply focus on the minimum current thresholds required to initiate nerve firing.

The minimum current-distance relations for the IVN case can be seen in Figure 4-12, and the corresponding absolute and relative values at sampled distances are found in Table 4.2. The similarities between Figures 4-11 and 4-12 at distances greater than $1\,mm$ are apparent, indicating that the majority of minimum threshold values targeted the stimulation of $D = 10\,\mu m$ fibers. At distances less than $1\,mm$, however, several of the minimum threshold values were derived from the stimulation of $D = 5\,\mu m$ fibers, as marked by boldface values in Table 4.2.

Several interesting trends can be identified from the data. For small distances, electrode configurations 2, 4, and 6 performed almost equally well, requiring just $50\,\mu A$ of current when located $100\,\mu m$ from the nerve. Across the entire distance spectrum, electrode configuration 4 was the most effective electrode geometry. EC2, 4 and 6 all share a primary cathodal component, and were significantly more effective

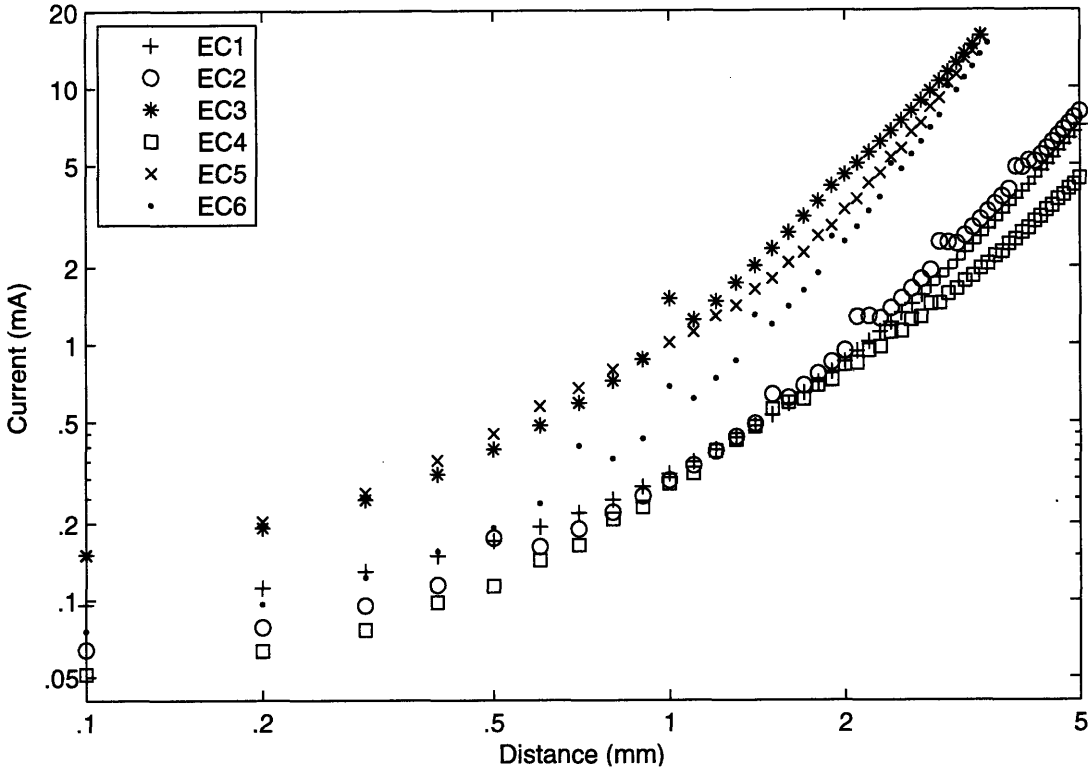

Figure 4-11: IVN Current-Distance Relations for Fiber Diameter $D = 10\,\mu m$

at eliciting nerve firing at small distances than configurations with a primary anodal component (EC1 and EC5). The activating function shape of electrode configuration 4 (Figure C-4) is a possible explanation for the low threshold values. The positive region of the function is broader than for other cathodal stimuli, suggesting a larger portion of the nerve is depolarized. However, it is possible that the strong negative region of f blocks AP propagation toward the anode, resulting in a unidirectional signal flow. To improve chances of an afferent response, the dipole should be oriented such that the anode is positioned closer to the end-organs. Several of the trends observed at small distances are reversed for large distances. The tripolar configurations (EC5 and EC6), as well as the longitudinal dipole, become much less effective because they start to resemble zero net sources at large distances. In contrast, the monopolar anode (EC1) becomes more effective; at a distance of $2\,mm$, the threshold is within just 3% of the treshold for EC4.

Absolute

	0.1 mm	0.2 mm	0.5 mm	1 mm	2 mm	5 mm
EC 1	95.77	111.85	170.42	312.25	855.55	7099.27
EC 2	**52.64**	**75.91**	**165.96**	294.57	943.20	8013.33
EC 3	**80.33**	**128.51**	**371.95**	**1270.20**	4567.57	Inf
EC 4	51.19	63.20	113.57	286.10	830.79	4398.00
EC 5	**105.23**	**167.48**	449.46	1015.51	3340.89	Inf
EC 6	**50.79**	**75.69**	**190.92**	**623.85**	2502.96	Inf

Relative

	0.1 mm	0.2 mm	0.5 mm	1 mm	2 mm	5 mm
EC 1	1.89	1.77	1.50	1.09	1.03	1.61
EC 2	1.04	1.20	1.46	1.03	1.14	1.82
EC 3	1.58	2.03	3.28	4.44	5.50	Inf
EC 4	1.01	1.00	1.00	1.00	1.00	1.00
EC 5	2.07	2.65	3.96	3.55	4.02	Inf
EC 6	1.00	1.20	1.68	2.18	3.01	Inf
Rel. (μA)	50.79	63.20	113.57	286.10	830.79	4398.00

Table 4.2: Minimum IVN Threshold Values expressed in Absolute (*Top*) and Relative (*Bottom*) terms: Absolute threshold values are expressed in microamps (μA), while relative threshold values are expressed as a ratio to the minimum threshold at a given distance, listed on the last row for each fiber diameter; Minimum thresholds derived from $D = 5\,\mu m$ fibers are denoted in boldface.

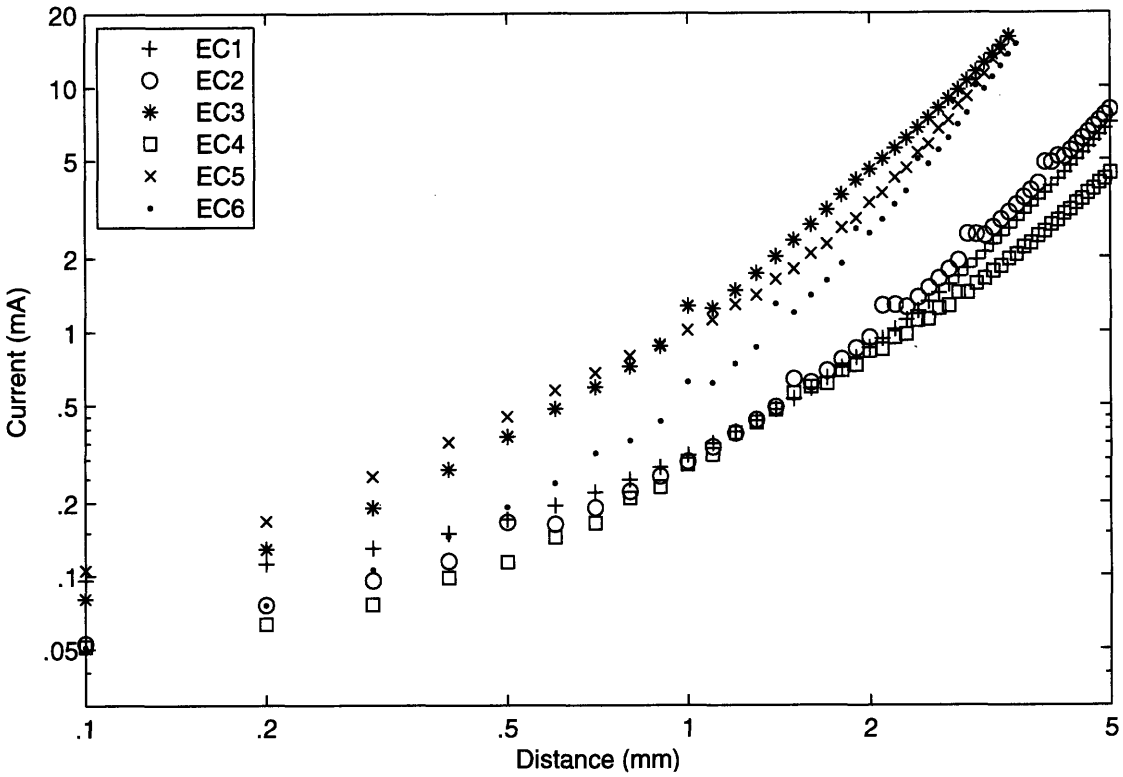

Figure 4-12: Minimum IVN Current-Distance Relations

4.2.2 Superior Vestibular Nerve (SVN)

The results presented in this section focus the minimum currents needed to excite Branch I and Branch II of the superior vestibular nerve. The effectiveness of the electrode configurations will be presented, and the data will be used to suggest the placement of electrodes to preferentially stimulate either of the branches.

Comparison of Electrode Configurations

The configurations tested were identical to those considered for the IVN case, with the exception of EC3. Each electrode configuration was placed nearest Branch I and subsequently moved away from the nerve with a resolution of $100\,\mu m$. The transverse dipole (EC3) for the SVN case included a stationary anode located centrally between the two branches and a mobile cathode whose distance was systematically increased from the nerve.

Figures 4-13 and 4-14 show the current-distance relations for Branch I and Branch

II, respectively. We can see that the threshold results for Branch II are in general greater than Branch I, as expected due to the larger distance to the electrode configurations. The exception to this trend is with electrode configuration 3. As the cathode moves further away from the nerve, the anode is more effective at stimulating the nerve and the threshold values drop. This result is significantly different from the monotonically increasing current-distance relations observed in the IVN case. We can see that other simulation results differ from the IVN case in Figure 4-12. For example, while EC4 was consistently the best performing configuration for the IVN case even at large distances, it does not perform as well for Branch II. For Branch I, electrode configurations 2, 4, and 6 had low thresholds for small electrode distances (the same as the IVN case), however at larger distances the change in configuration threshold order is apparent. Therefore for small distances, the configurations behaved similarly for the IVN case and Branch I of the SVN case, as we would expect. For large electrode distances, the deviations can be explained by the fundamentally different volume conductors for the two cases.

A comparison between the minimum threshold values for each electrode configuration is presented in Figures 4-15 and 4-16. We can see that threshold currents needed to excite Branch I are generally smaller than those needed to excite Branch II. The exceptions to this trend occur for electrode configuration 3, and a small range of distances for EC2 around $4\,mm$. The results suggest that the separation of the modeled SVN is large enough to allow for selective stimulation of either of the branches. The implications of the absolute threshold values for each branch, as well as the relative differences in between each branch will be considered in the next section.

4.3 Suggestions for Electrode Placement

4.3.1 IVN Case

The primary criteria for selecting an electrode configuration for the IVN case is threshold value. The use of minimum currents are preferred whenever possible to reduce

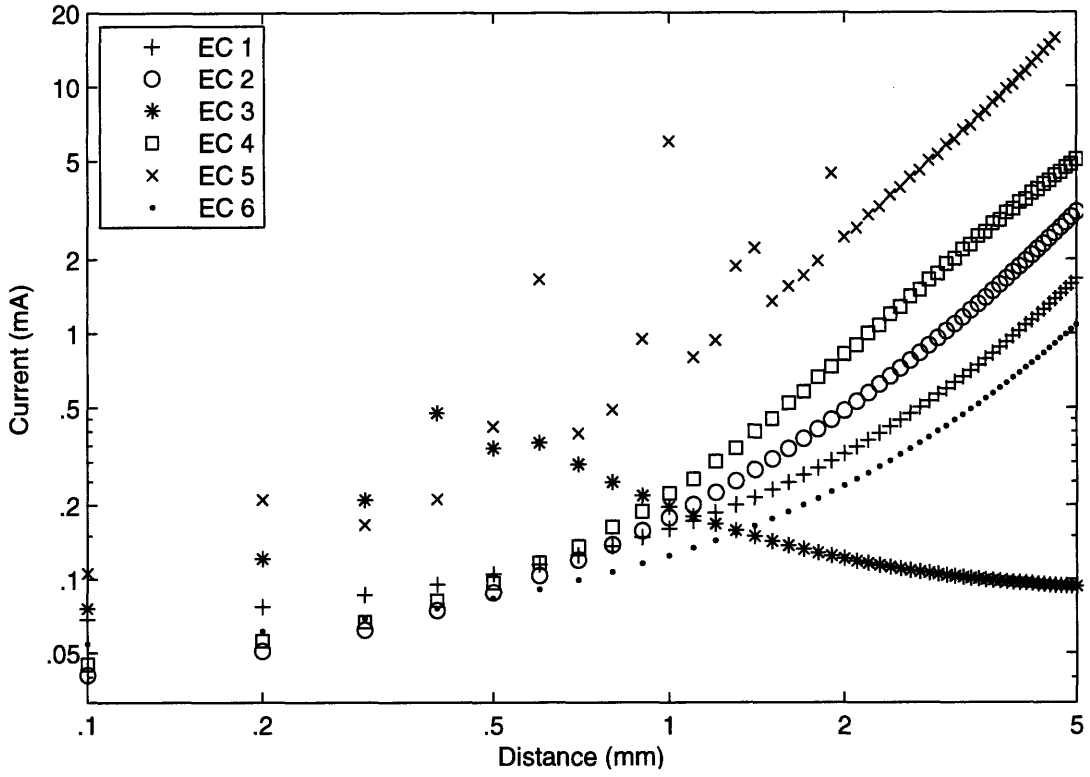

Figure 4-13: Minimum SVN Current-Distance Relations for Branch I

the chance of injury or discomfort to the patient. Furthermore, a secondary criteria is configuration simplicity—the ability to use a configuration with fewer electrodes is much preferred to using one with multiple electrodes. In addition to those two criteria, the distance to the electrode must also be considered. The close proximity of several nerves in the temporal bone cavity would suggest that one try to place the stimulating electrode closest to the nerve of interest as possible to reduce unwanted stimulation. While in general that is true, one must also consider the possible damages to the nerve if the electrode is brought in direct contact, as the nerves are quite delicate.

Keeping these criteria in mind, it seems that the best choice for an electrode configuration for the IVN case is EC2, the monopolar cathode. The simulation data from Figure 4-12 indicate that EC2 has the smallest threshold values for a monopolar electrode. The single electrode would allow for the most precise placement accuracy, as the separation distance between multiple electrodes would not be an issue. Further-

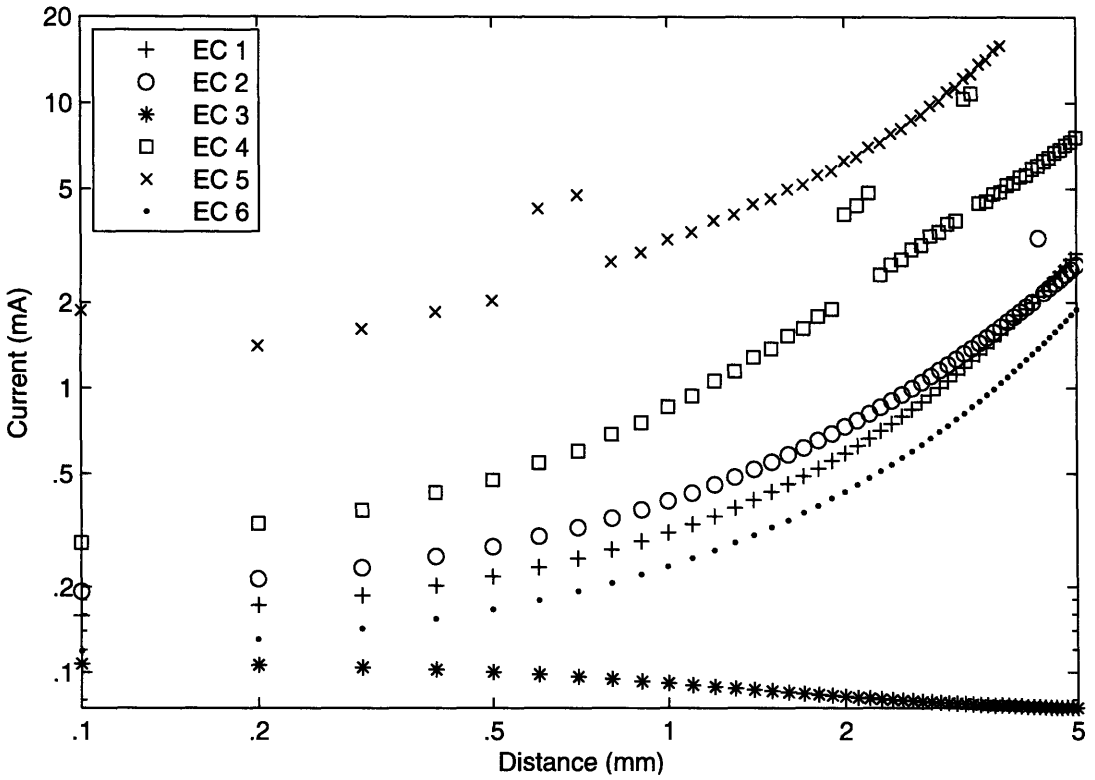

Figure 4-14: Minimum SVN Current-Distance Relations for Branch II

more, the electrode needs to be driven only with small currents to elicit nerve firing when placed close to the nerve. Nominal currents of $56\,\mu A$ and $76\,\mu A$ are required for distances of $100\,\mu m$ and $200\,\mu m$, respectively.

It must be noted that our simulations do not factor into account current density at the electrode interface. Strictly speaking, both the absolute charge delivered at the electrode and the current density play a role in nerve stimulation. The issues of electrically safe stimulus currents, current densities, and electrode-to-tissue interfaces have been abstracted away. A good starting point for discussion of such topics can be found here [63]. We will note that although the theoretical current density at our modeled point sources is infinite, the experimental implementation of such electrodes is most likely a spherical ball formed at the tip of a platinum wire. Thus, the actual current density would depend on the surface area of the exposed electrode.

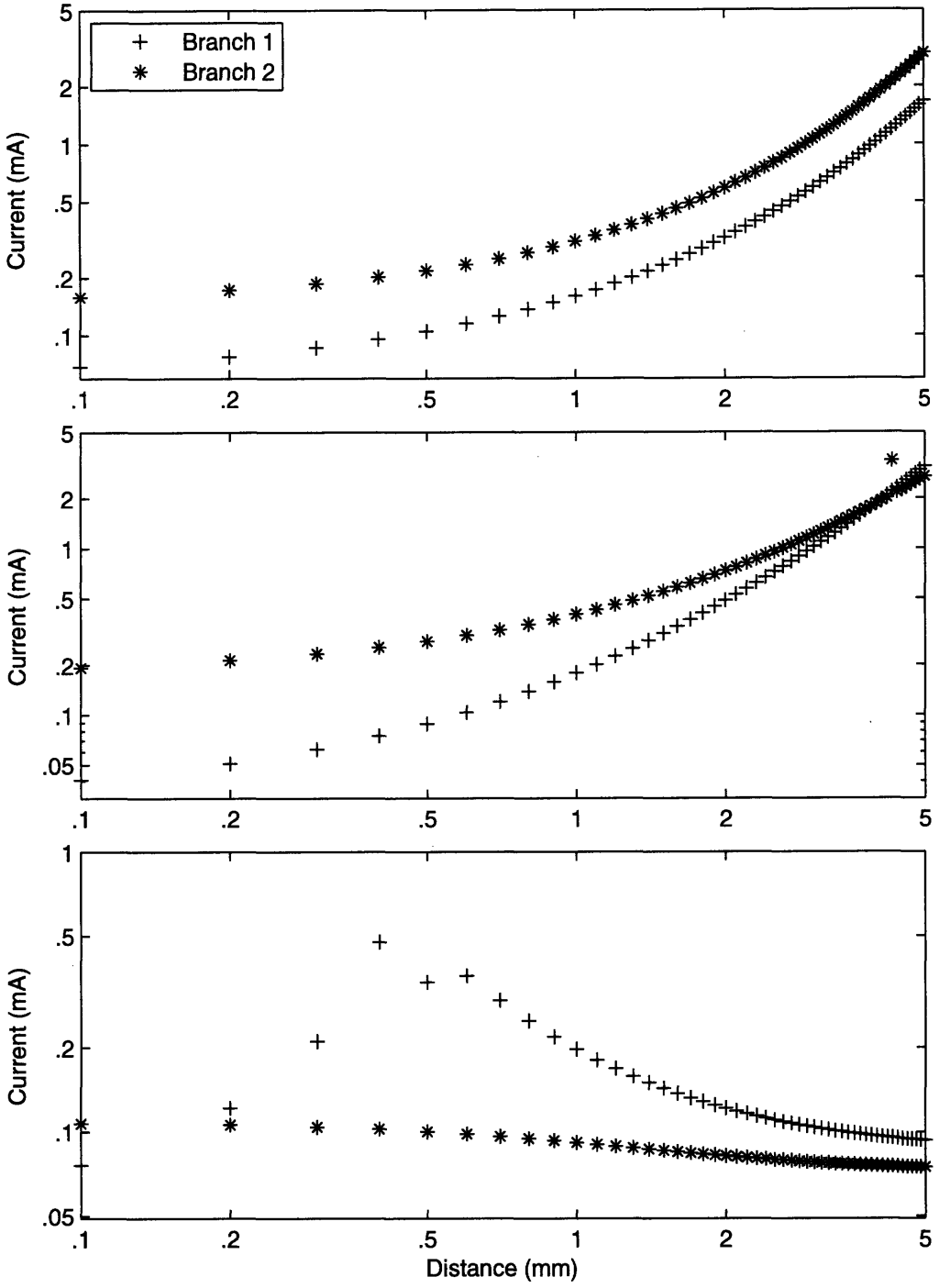

Figure 4-15: SVN Minimum Current-Distance Relations for Electrode Configurations 1–3

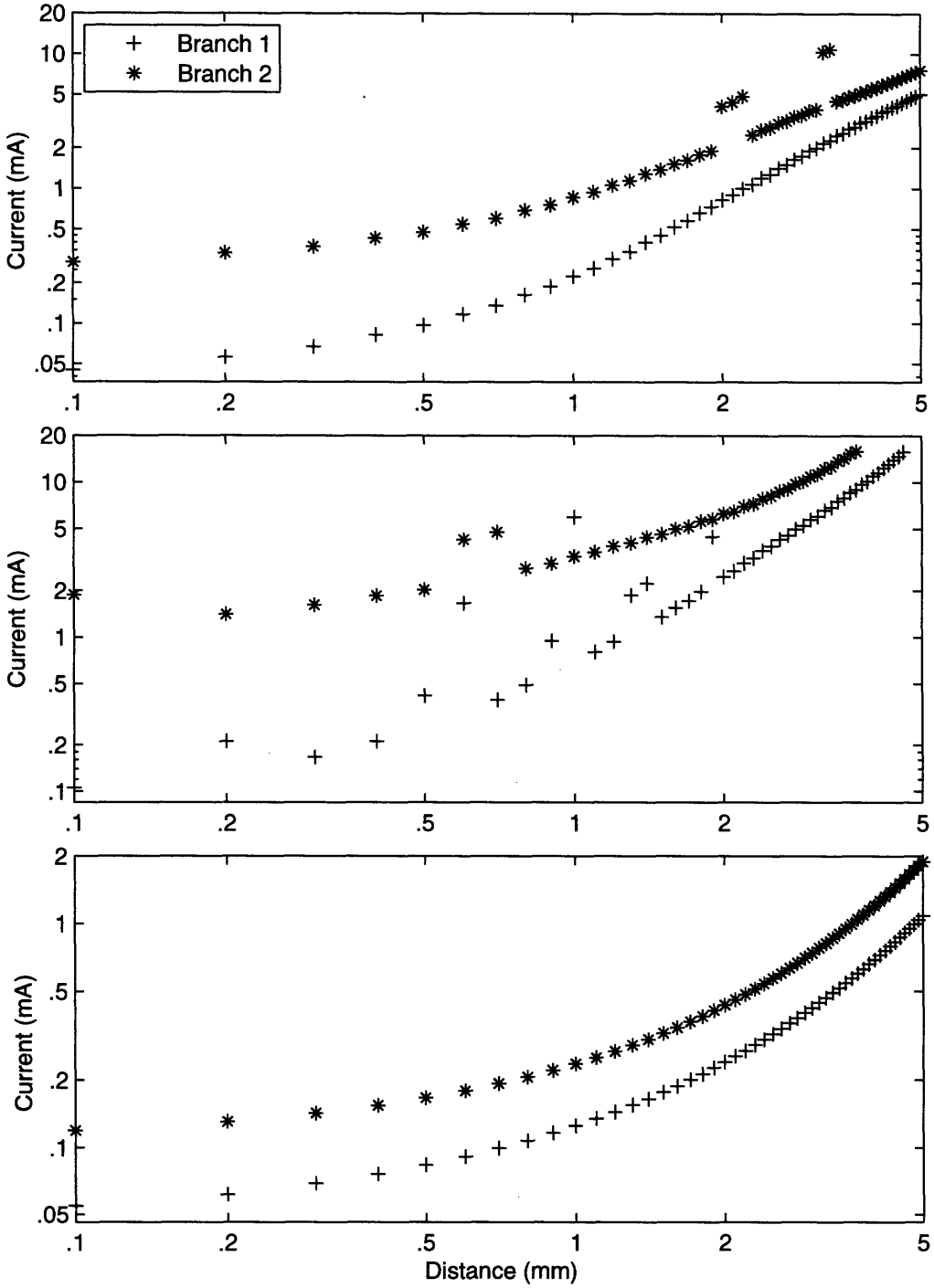

Figure 4-16: SVN Minimum Current-Distance Relations for Electrode Configurations 4–6

4.3.2 SVN Case

In addition to the criteria mentioned for the IVN case, we must also consider the relative differences in thresholds for the two branches in the SVN case. We wish to optimally find the greatest difference in threshold value for a given electrode configuration and stimulation distance, to maximize our probability of selective stimulation. Another important consideration is the proximity of the SVN to the facial nerve. Examination of the human 3D temporal bone reconstruction [32] reveals that the distance to the facial nerve may be as small as $0.5\,mm$ in the branching regions of the SVN.[9] The inadvertent stimulation of the facial nerve would result in twitching of the face muscles, and should be avoided.

The electrode configuration that seems best suited for selective stimulation is again the monopolar cathode. When located a distance of $100\,\mu m$ away from the nerve, 5.5 times more current is needed to stimulate Branch II than Branch I. Although this ratio is smaller than the ratios for electrode configurations 4 and 5 (6.9 and 11), EC2 is a much easier geometry to implement *in vivo*. The ratio for distances of $200\,\mu m$ and $300\,\mu m$ drops only slightly to 4.7 and 4.2, respectively. The absolute current values at these distances are also small, ranging from $31\,\mu A$ to $51\,\mu A$. Furthermore, EC2 has the advantage of being combined with a stationary anode to become electrode configuration 3. Placing the cathode $300\,\mu m$ from Branch I and placing the anode centrally between Branch I and Branch II would allow for sequential selective stimulation of both branches. Driving the cathode with a current of magnitude $51\,\mu A$ and leaving the anode undriven would excite only Branch I. However, driving both the cathode and anode with a current of $106\,\mu A$ would excite just Branch II without exciting Branch I. Therefore we show that it is possible to selectively excite both branches of the superior vestibular nerve model by varying the electrode configuration and stimulus amplitude.

It is difficult to predict the response of the facial nerve from our simulation data.

[9] A larger separation window does exist, but is located further medially down the nerve away from the branch. A selective fascicular stimulation technique would need to be employed to target stimulation at this location.

Surely the addition of another nerve tissue to the volume conductor would change the field behavior. Nevertheless, let us examine the threshold data at an electrode-to-nerve distance of $0.5\,mm$. We see for electrode configuration 2 that the minimum threshold value is $75\,\mu A$, approximately 1.5 times that for the configuration suggested above. It is conceivable that one could therefore selectively stimulate Branch I of the SVN and avoid the stimulation of the facial nerve using EC2.

Judging the relation for electrode configuration 3 is considerably more difficult. Unlike the potential field calculation, the response of the nerve fiber is not linear, and we cannot simply examine the behavior of the anode and cathode separately. While the minimum threshold value for Branch II is lower than the suggested stimulus ($102\,\mu A$ compared to $106\,\mu A$), we cannot conclusively say whether or not the facial nerve will be excited. Examination of the current-distance relation indicates that the slope is negative. The reduction in threshold values for increasing distance, as previously mentioned, is likely due to the stationary anode, whose stimulating powers increase as the cathode moves farther away. It is therefore not possible to predict the behavior at a given distance to the facial nerve because no anode would be located in its vicinity.

4.4 Validation of Results

The lack of quantitative vestibular specific stimulation data from human trials makes it difficult to validate our simulation results. Nevertheless, we will attempt to qualitatively address the findings of a recent study [64] that investigated the electrical stimulation of the inferior vestibular nerve prior to innervation of the posterior semicircular canal.

The stimulation was performed with a monopolar electrode driven with a multiphasic stimulus waveform containing four phases. Each pulse consisted of a $200\,\mu s$ cathodal phase, followed by neutral and anodal phases of the same duration. The fourth phase was also neutral, with a duration that was modulated to obtain a given pulse repetition rate. The threshold data was collected at a rate of 200 pulses per

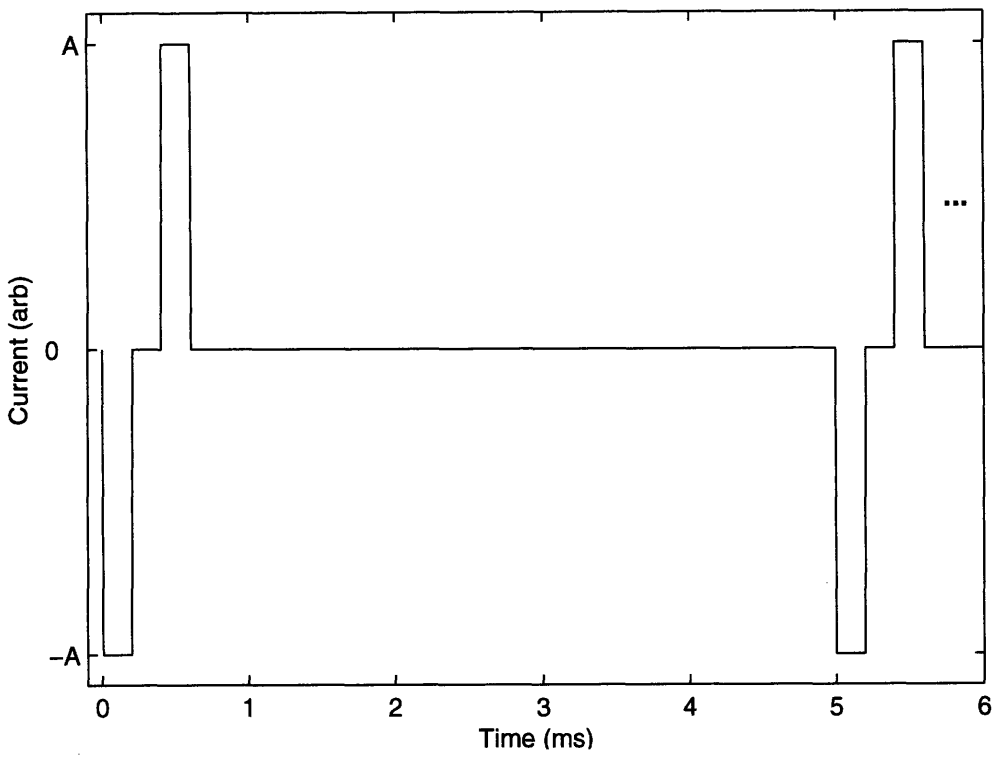

Figure 4-17: Multiphasic Stimulus Waveform used to Determine Current-Distance Thresholds in Human Patients [64]: See text for description.

second, constraining the length of the fourth phase to $4.4\,ms$. Figure 4-17 graphically illustrates the waveform driven at an arbitrary amplitude A.

Strictly speaking, the stimulus applied in the human study does not match any of the electrode configurations simulated. However, because our volume conductor is treated as purely resistive, we may think of the multiphasic waveform as being a superposition of two applied stimuli, namely a monopolar cathode followed by a monopolar anode. The $200\,\mu s$ neutral phase that separates the two stimuli would allow enough time for an action potential generated by the cathodal phase to travel a significant length down the nerve,[10] and would therefore not disrupt the ability of the anodal phase to generate an action potential. It is therefore conceivable that the stimulation was elicited by either of the two phases, thus we will compare the threshold results to the simulation results of electrode configurations 1 and 2, the

[10]An action potential traveling on a $D = 10\,\mu m$ fiber would travel a distance of $9.4\,mm$ in the span of $200\,\mu s$.

monopolar anode and monopolar cathode.

In the surgical experiment, threshold data points were obtained by stimulating the nerve with the above waveform at three locations. The first stimulation was attempted without any drilling into the temporal bone. The second stimulation was made while approaching the nerve, at a point where the nerve could not be visually seen. The third and final stimulation was attempted at a distance of $100\,\mu m$ from the nerve, as estimated by a surgical technique referred to as "blue-lining". At the first location, no nerve response was observed[11] at the maximum $1\,mA$ current applied, and only a weak response was observed with the same amplitude at the second stimulus site. In contrast, currents ranging from $100\,\mu A$ to $1\,mA$ were able to excite the nerve at the closest stimulation site [64].

We can assign approximate distances to correspond to the qualitative stimulation sites by examining the 3D reconstruction of a human temporal bone [32]. The distance from the inferior vestibular nerve to the tympanic membrane, the surgical site of entrance, is approximately $7\,mm$. This implies that the intermediate stimulation site lies somewhere between $100\,\mu m$ and $7\,mm$, most likely somewhere between the two extremes. Examination of the minimum current thresholds in Figure 4-12 reveals that our simulation results correspond to the experimental findings. Our model predicts a current of $1\,mA$ is capable of stimulating a fiber approximately $2\,mm$ away from either EC1 or EC2. An experimental stimulus of this strength was unable to stimulate the nerve at the first electrode site, located well beyond $2\,mm$ from the nerve. At the intermediate site, this level of current produced a small response. If in fact the intermediate location was located around $2\,mm$, the finding would be consistent with the simulation results. Finally, at a distance of $100\,\mu m$ from the nerve, the model predicts threshold current values of approximately $53\,\mu A$ and $96\,\mu A$ for electrode configurations 1 and 2, respectively. The experimental findings suggest a value of $100\,\mu A$, consistent with the prediction for an anodal stimulus and only a factor of two off from the prediction for a cathodal stimulus.

We must stress that although the model seems to fully predict *in vivo* stimulation

[11]The nerve response was measured by monitoring the patient's vestibulo-ocular response.

behavior for two electrode configurations, the comparisons made were based upon fundamentally qualitative findings. To fully validate the model, a more systematic study would need to be conducted. Nevertheless, the correspondence between the experimental and theoretical models is quite exciting.

4.5 Comparison of Methods

The results derived in this chapter has so far focused on the most detailed modeled studied, namely potential distributions in the inhomogeneous and anisotropic volume conductor driving the nonlinear SEF model to determine threshold behavior. However, our analysis would not be complete without comparing these models to their simpler counterparts, the homogeneous isotropic volume and the activating function. The following sections describe differences in threshold behavior across the models for the inferior vestibular nerve (IVN) case.

4.5.1 Homogeneous Isotropic Volume Conductor

The potential distribution for all six electrode configurations was computed for the homogeneous volume using the averaged resistivity of all tissues, $\rho = 1.94 \text{ x } 10^4\, \Omega\, mm$. The averaged value was nearly an order of magnitude greater than the transverse resistivity of the nerve, and consequently the potential distribution in the nerve was much higher than for the anisotropic, inhomogeneous case. Figure 4-18 shows the percent error of the field calculation as compared to the Ansys calculated solution along path **C** with an electrode distance of $1\, mm$. We can see that the error was substantial across all electrode configurations, ranging from a minimum of 33% for eletrode configurations 1 and 2 to a maximum of 300% for EC3.

The effect of the larger potentials on threshold calculations performed in NEURON is apparent from Figures 4-19 and 4-20. The figures compare the current-distance relations of the Ansys and homogeneous results for each electrode configuration. We can clearly see that the threshold values are lower for the homogeneous case in all configurations except at large distances for EC3.

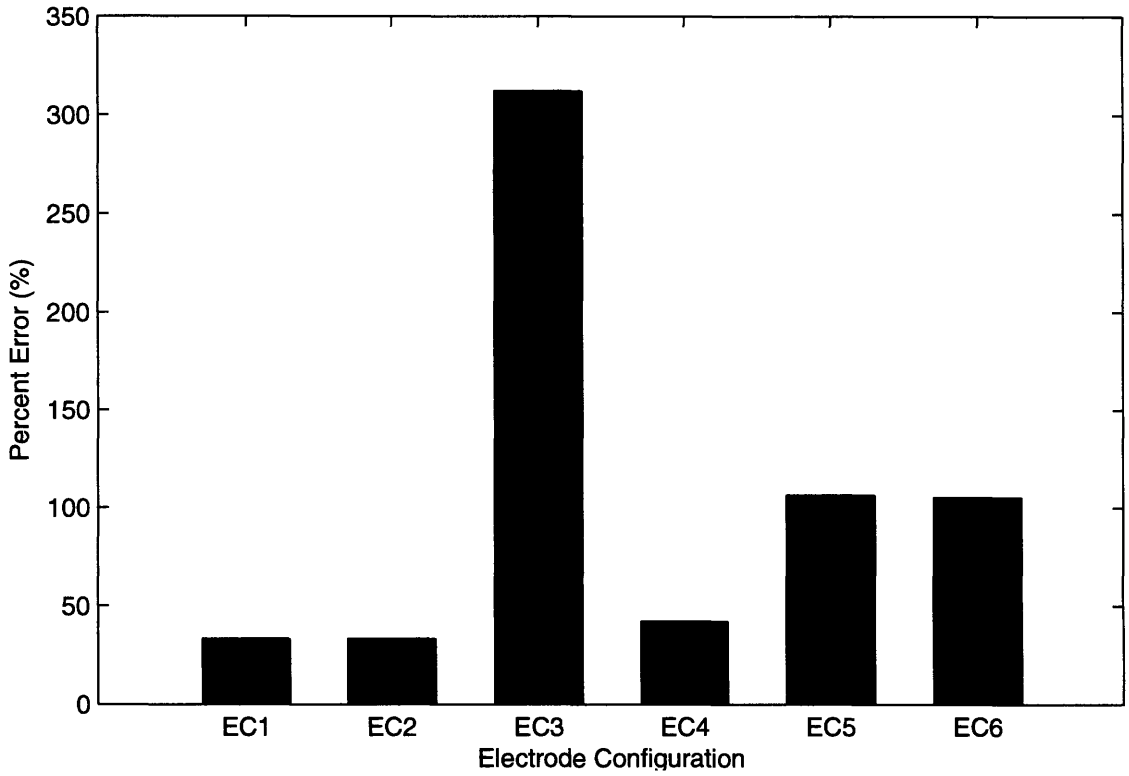

Figure 4-18: Percent Error of Homogeneous Potential Solution Calculated along Path C with an Electrode Distance of $1\,mm$

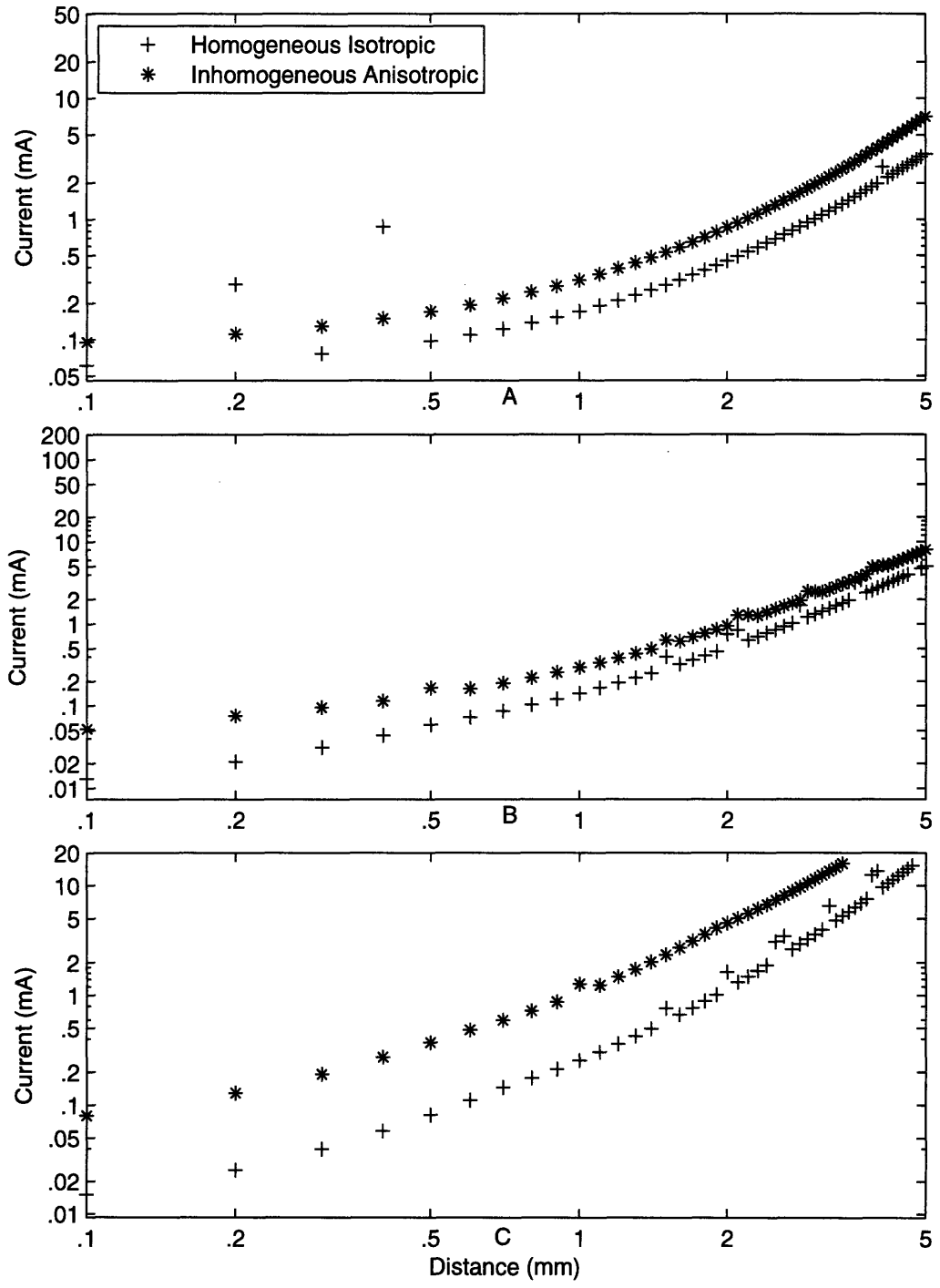

Figure 4-19: Minimum IVN Current-Distance Relations derived from the Homogeneous Volume Conductor: **A**, Electrode Configuration 1; **B**, Electrode Configuration 2; **C**, Electrode Configuration 3

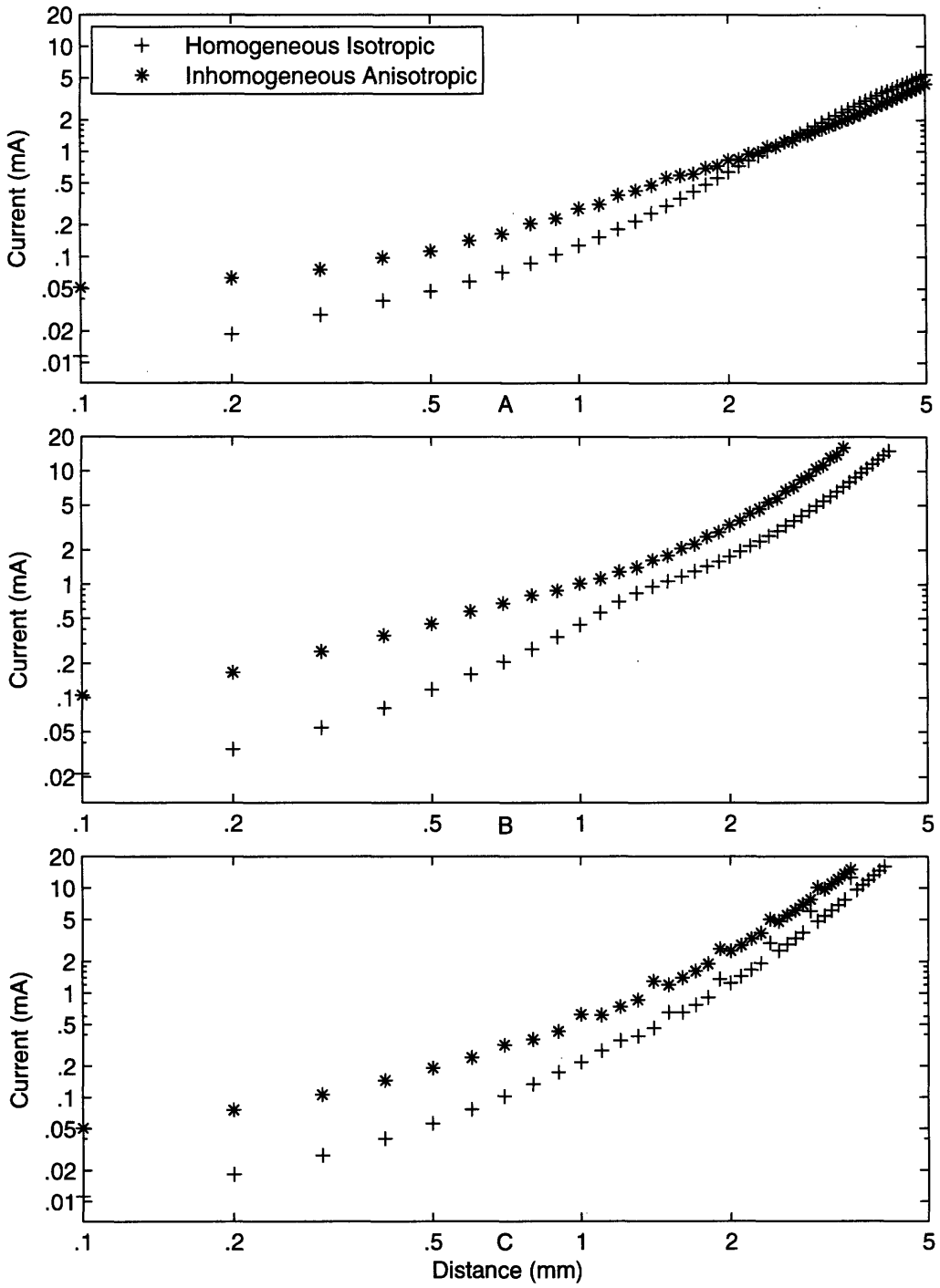

Figure 4-20: Minimum IVN Current-Distance Relations derived from the Homogeneous Volume Conductor: **A**, Electrode Configuration 4; **B**, Electrode Configuration 5; **C**, Electrode Configuration 6

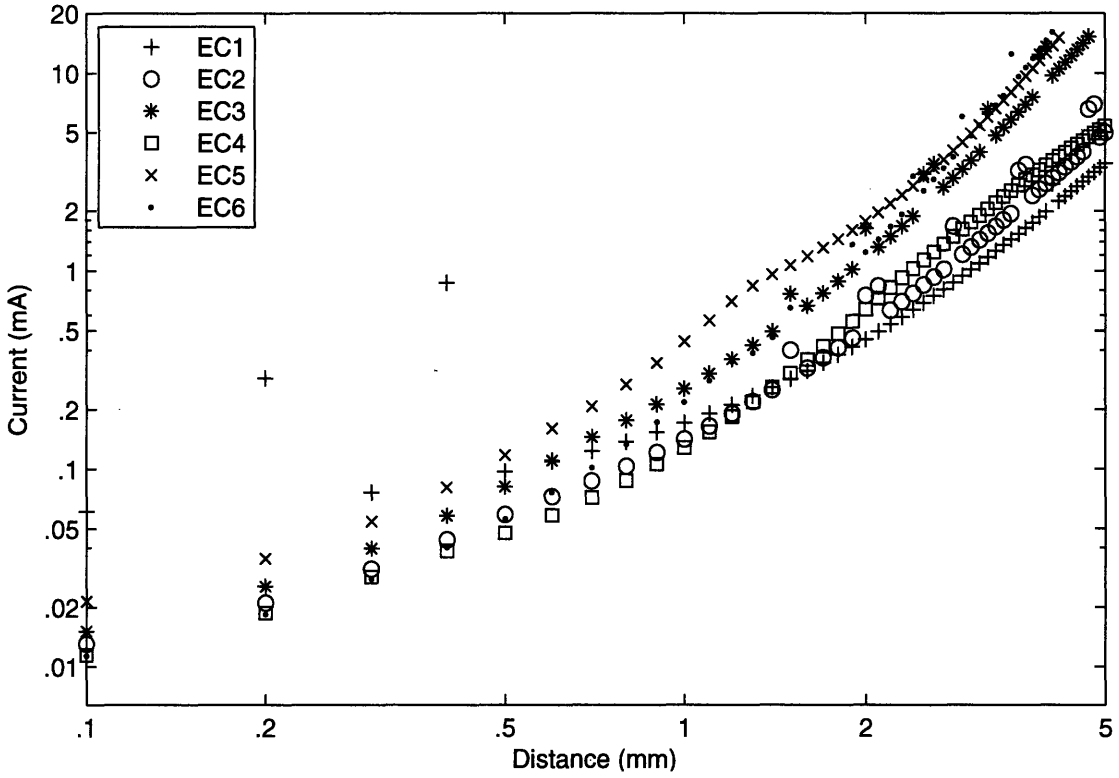

Figure 4-21: Minimum IVN Current-Distance Relations derived from the Homogeneous Volume Conductor

Figure 4-21 shows the minimum thresholds for the homogeneous case, and Table 4.4 shows the absolute and relative values of the threshold, as compared to the inhomogeneous, anisotropic solution. We can clearly see that the threshold values are lower than for the anisotropic case. In fact, examination of Table 4.4 shows the values are on average 4 times smaller at a distance of $0.1\,mm$ and twice as small at a distance of $5\,mm$.

The results indicate that the threshold values calculated by the nonlinear SEF model can vary greatly between the homogeneous isotropic volume and the inhomogeneous, anisotropic volume. A follow-up study would be needed to determine if a smaller value for the resistivity would improve the correlation of threshold values. Such a study would be very beneficial, as the calculation time for the analytical solution is much faster than the numerical solution.[12]

[12]The solution to all EC's solved in just a few seconds in Matlab, compared to the several hours required for the Ansys solutions.

Absolute						
	0.1 mm	**0.2 mm**	**0.5 mm**	**1 mm**	**2 mm**	**5 mm**
EC 1	61.22	287.13	97.23	171.21	452.40	3488.47
EC 2	13.05	21.02	59.03	141.88	747.72	5011.80
EC 3	15.09	25.47	81.49	254.90	1626.62	Inf
EC 4	11.45	18.68	47.51	127.93	638.72	5389.92
EC 5	21.40	35.23	117.61	441.60	1769.52	Inf
EC 6	11.33	18.35	55.90	217.42	1236.40	Inf

Relative						
	0.1 mm	**0.2 mm**	**0.5 mm**	**1 mm**	**2 mm**	**5 mm**
EC 1	1.56	0.39	1.75	1.82	1.89	2.04
EC 2	4.03	3.61	2.81	2.08	1.26	1.60
EC 3	5.32	5.05	4.56	4.98	2.81	-
EC 4	4.47	3.38	2.39	2.24	1.30	0.82
EC 5	4.92	4.75	3.82	2.30	1.89	-
EC 6	4.48	4.12	3.42	2.87	2.02	-

Table 4.3: Minimum IVN Threshold Values (Homogeneous, Isotropic Case) expressed in Absolute (*Top*) and Relative (*Bottom*) terms: Absolute threshold values are expressed in microamps (μA), while relative threshold values are expressed as an inverse ratio to the minimum threshold for the anisotropic, inhomogeneous solution.

4.5.2 Activating Function

The inhomogeneous, anisotropic potential data was used to calculate stimulation thresholds based on the activating function, using the threshold criteria described in Equation 3.28. Figures 4-22 and 4-23 compare the threshold results obtained from the activating function to those obtained from the SEF model for each electrode configuration. It is clear from the figures that the activation function predicts a lower value for the stimulus threshold than the nonlinear model. The exception to this trend occurs for electrode configuration 4, where the activating function predicts a higher threshold for distances greater than approximately $1.2\,mm$.

We can see from the figures that the shape of the CD relations roughly correspond for electrode configurations 2, 3, 4, and 6. By simply scaling the activating function results, we can improve their correlation to the SEF results. The amount of scaling would precisely correspond to the adjustment of the activating function definition used in Equation 3.28. However, the scale factors were found to be inconsistent

across all of the electrode configurations for the minimum threshold curves displayed in Figures 4-22 and 4-23. The same result was found by examining the scale factors for individual fiber diameters—a single value used for the activation function threshold was not sufficient to predict the nonlinear results.

Therefore preliminary analysis indicates that a single definition of the activation function threshold is unable to predict the results from the SEF model. The result is not entirely surprising, since we are trying to capture the nonlinear dynamics of the SEF model with a simple linear function that only examines the field created by the electrodes, not the response of the nerve fiber to the imposed field. However, over small regions of interest, the activating function current-distance relations can correspond to those produced by the SEF model. Unfortunately, a systematic method for determining the activation function threshold *a priori* was not found. Without further analysis, it is unclear weather or not an electrode configuration specific or model specific definition for the activating function threshold can be determined. At the very least, the activating function serves as a useful qualitative tool to explain trends found using the nonlinear model.

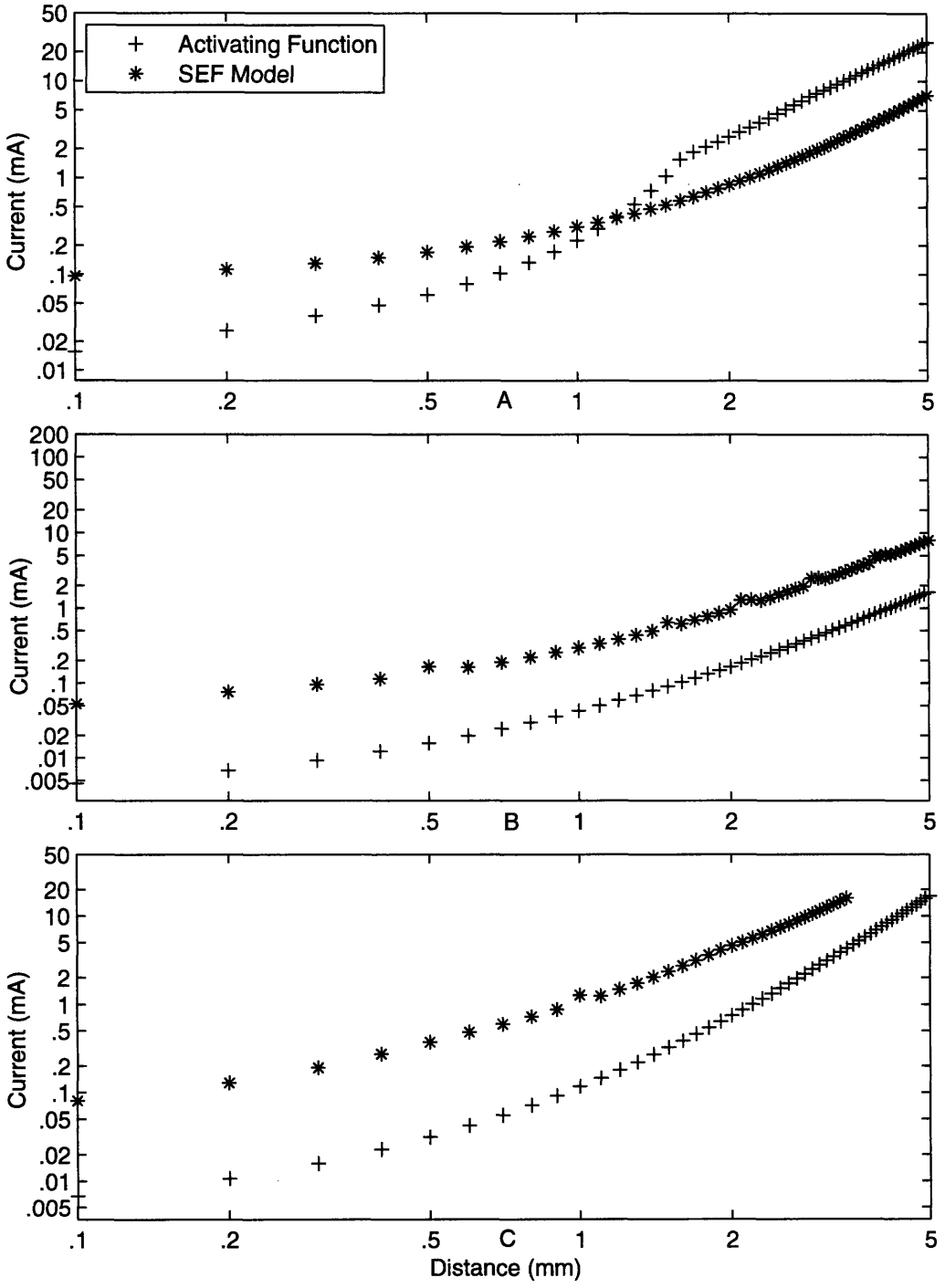

Figure 4-22: Mininmum IVN Current-Distance Relations (Activating Function): **A**, Electrode Configuration 1; **B**, Electrode Configuration 2; **C**, Electrode Configuration 3

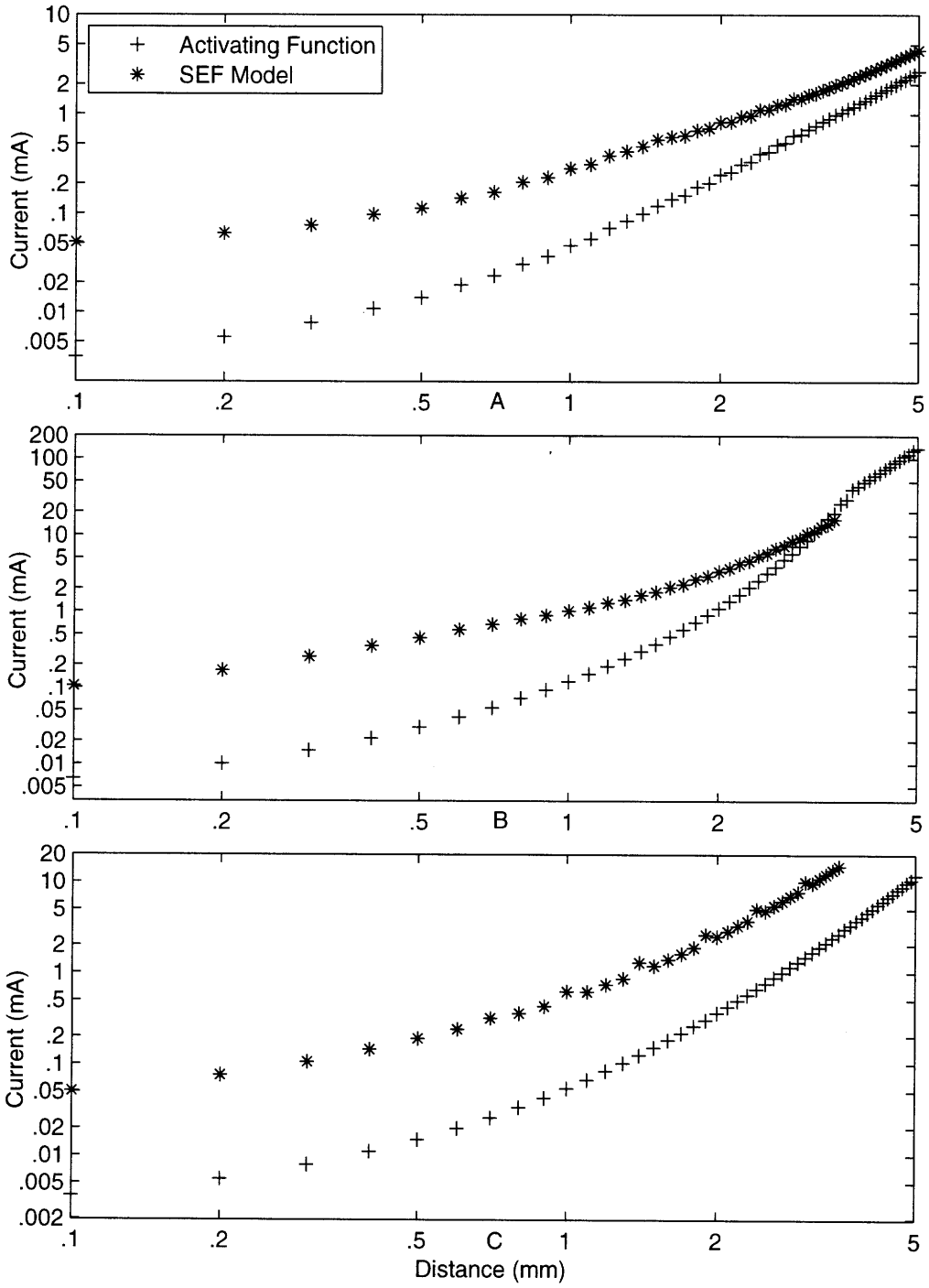

Figure 4-23: Minimum IVN Current-Distance Relations (Activating Function): **A**, Electrode Configuration 1; **B**, Electrode Configuration 2; **C**, Electrode Configuration 3

THIS PAGE INTENTIONALLY LEFT BLANK

Chapter 5

Conclusion

5.1 Summary

The research conducted as part of this thesis modeled the extracellular stimulation of peripheral vestibular nerves for a proposed human implantable prosthesis. Two types of models were created to analyze nerve threshold behavior, volume conductors and biophysical models. Volume conductors were created to determine the potential distributions generated by each of the electrode configurations. The potential distributions were subsequently used to drive biophysical models to predict nerve firing behavior. The results focused on the most detailed models studied, namely a fully anisotropic and inhomogeneous finite-element volume and the nonlinear Schwarz-Eikhof-Frijns (SEF) model based on mammalian myelinated nerve fibers.

The nerve firing threshold results computed with the detailed models were compared to two simpler models, a homogeneous and isotropic volume and the linear activating function. The homogeneous, isotropic volume was found to overestimate the potential distribution within the nerve and produced lower threshold results than the anisotropic, inhomogeneous volume. Furthermore, the linear activating function model was found to be a poor predictor of excitation thresholds.

Systematic current-distance relations were derived across several parameters including interpolation path, fiber diameter, and electrode configuration for two cases, the inferior vestibular nerve and the branched superior vestibular nerve. Trends were

analyzed across parameters and were explained whenever possible with the qualitative description of the activation function. Furthermore, the dataset was reduced by eliminating fiber diameter and interpolation path from the parameter space to obtain the minimum threshold necessary to elicit nerve firing. The minimum firing thresholds were compared for the two nerve cases and were used as the basis for determining optimal electrode configurations for each case.

Suggestions were made on the placement and type of electrode configuration best suited for stimulating the respective nerves. The criteria used for the selection included minimum current, simplicity of the electrode configuration, and proximity to other nerves. For the inferior nerve case, a cathodal stimulus located at a distance of $100\,\mu m$ or $200\,\mu m$ and driven with a stimulus current of $56\,\mu A$ or $76\,\mu A$ was recommended. Selective stimulation of each branch was the goal for the superior nerve case, imposing a further criteria to maximize the threshold ratio between stimulation of the respective branches. A transverse dipole electrode configurations was suggested that allowed selective stimulation of either branch. The configuration included a cathode located $300\,\mu m$ from Branch 1 and an anode centrally located between both branches. When driven with a cathodal stimulus of strength $51\,\mu A$, only Branch I was excited, while driving both electrodes with a magnitude of $106\,\mu A$ excited only Branch II. The proximity to the facial nerve was considered in the choices of configuration and placement, however it was inconclusive whether or not the facial nerve would fire with the suggested electrode configurations and stimuli.

5.2 Recommendations for Future Work

The work conducted as part of this thesis opens the door to a wide range of follow-up studies, both experimental and theoretical. Presented below are a few suggestions for future work.

1. Conduct an experimental validation of the threshold data by systematically varying the stimulus site *in vivo* and recording the current values needed to elicit nerve firing. The study would validate the simulation results and encourage

further analysis of the data.

2. Conduct a parameterized simulation study varying the angle between the branches of the superior vestibular nerve and also their dimensions. The anatomical variations in nerve distances are not well-characterized, therefore the study would give insight into the ideal stimulus configurations needed to preferentially stimulate branches in different geometrical orientations.

3. Conduct a simulation study to determine electrode configurations and/or stimulus waveforms that preferentially target the tonic or phasic component of the vestibular nerve. Parameters to consider include pulse width and shape, as well as electrode location and geometry.

4. Perform a sensitivity analysis on all the model parameters to determine which ones have the greatest impact on the simulation results. The analysis would shed light into which parameters should be further experimentally verified.

5. Study the relationship between thresholds for the activating function and nonlinear model to determine if a suitable threshold can be found to reliably predict the nonlinear results for an operating range of interest.

6. Study the relationship between thresholds for the homogeneous, isotropic volume conductor and the inhomogeneous, anisotropic volume to determine if a suitable averaged conductivity can be found to reliably predict thresholds for an operating range of interest.

THIS PAGE INTENTIONALLY LEFT BLANK

Appendix A

Ansys Verification

A.1 Rotation of Element Coordinate System

As described in Section 3.2.3, the model for the superior division of the vestibular nerve (SVN) was both inhomogeneous and anisotropic. The anisotropy was achieved by placing Branch I parallel to the z axis, and setting conductivity of that axis higher than the transverse x and y axes[1]. Branch II was made anisotropic by rotating the element coordinate system (ESYS) of elements comprising that branch by 30° in the x-z plane, as shown in the code fragment in Figure A.1.

The effect of not rotating the ESYS for Branch II results in a higher potential in the region due to the higher resistivity. The higher potential would in turn cause the threshold predictions to be lower than they actually should be. Figure A-2 shows the difference in potential distributions with and without ESYS rotation for a monopolar anode of strength $I = 1\,\mu A$ placed inside of Branch II. The effect of not rotating the ESYS is a 7.45% increase in the maximum potential. *Extracellular* electrode placements shows the same trend of overestimating the potential, although the effect decreases with increasing electrode-to-nerve distances. Table A.1 summarizes these findings.

[1]Table 3.1 lists the transverse and longitudinal nerve tissue resistivities

```
! Rotate coordinate system (CS) of branch
! Select Nodes Associated with branched areas
cmsel,s,branch
nsla,s,1
cm,bnodes,node

! Select Elements Associated with branched nodes
esln,s,0
cm,belem,elem

! Set global CS to cartesian
csys

! Select branched elements
cmsel,s,belem
mat,1 $type,1 $real,1

! Create new local CS rotated 30 degees x-z plane
loca,11,0,0,0,0,0,30

! Create a new element CS from the local CS
esys,11

! Modify all the elements in the branch to new element CS
emod,all

! Set global CS to cartesian
csys

! Select and plot all elements
allsel
eplot
```

Figure A-1: Source Code used to rotate the element coordinate system (ESYS) of Branch II. The code fragment is written in APDL (Ansys Parametric Design Language) and would appear in a larger ANSYS script following the MESHING and preceding the BOUNDARY CONDITIONS source code.

Distance to Nerve (mm)	**Potential Overestimate (%)**
0 (inside nerve)	7.45
.1	2.51
1	1.86
5	1.37

Table A.1: Maximum Potential Overestimate without ESYS Rotation for a monopolar anode of strength $I = 1\,\mu A$. The effect of potential overestimate decreases as the electrode distance to the nerve increases. Since the potential field estimate is linear, the percentage overestimate would remain the same for increased stimulus strengths.

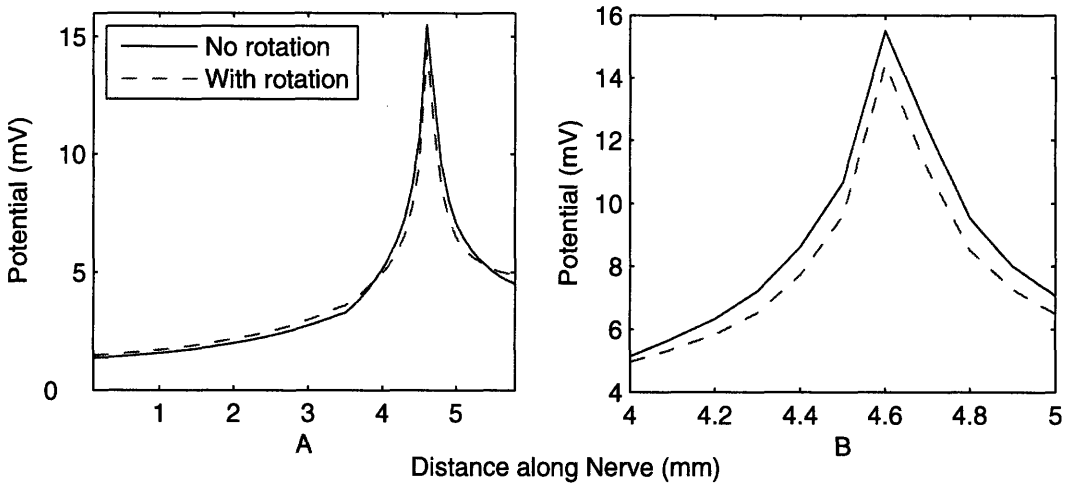

Figure A-2: Effect of ESYS Rotation on Potential Field, Monopolar Anode placed inside Branch II: **A**, Potential versus distance along the nerve plotted for stimulus strength $I = 1\,\mu A$. **B** shows a zoomed version of **A** in the region of the electrode. The effect of not rotating the ESYS is a 7.45% increase in maximum potential. Note: Increasing distance along the nerve corresponds to more distal locations.

A.2 Mesh Size Verification

The finite element method (FEM), like all numerical techniques, requires a balance between solution accuracy and computation time. To find a balance suitable for our simulations, a mesh convergence study was conducted to determine an optimal mesh resolution. Two mesh sizes were used in our model due to a large difference in size scales for our geometry. The nerve, epineurium, and saline structures were small and complex, requiring a fine mesh to represent accurately. In comparison, the bone encasing those structures was very large and was modeled as a sphere of radius $20\,mm$ to represent boundary conditions. Since we were not interested in potential field solutions in this region, a larger mesh could be used to create this large and simple structure.

A combination of mesh sizes was investigated, with Mesh Number 1 being the finest and Mesh Number 6 being the most course, as seen in Table A.2. Elements used to model nerve, epineurium, and saline were of size "Element Size I" and elements

Mesh Number	Element Size I (mm)	Element Size II (mm)
1	0.1	5
2	0.1	10
3	0.2	5
4	0.2	10
5	0.3	5
6	0.3	10

Table A.2: Mesh Number and Corresponding Resolution: Elements used to model nerve, epineurium, and saline were of size "Element Size I" and elements used to model bone were of size "Element Size II".

used to model bone were of size "Element Size II". The mesh convergence study consisted of examining both run time and accuracy of each mesh. All simulations were conducted on a computer with an Intel Pentium 4, 3.2 GHz processor and 4 GB of physical memory running Microsoft Windows XP (SP2) and Ansys Mechanical/Emag (v. 9.0).

Figure A-3 shows the relation between run time and mesh number for a single load step (electrode placement). As expected, increasing the mesh coarseness decreased computation time with respect to both CPU cycles and wall time. Since numerous electrode placements were considered for a given electrode configuration (Figures 3-7 and 3-8), it was imperative to keep computation time reasonable. For example, 51 load steps were required to examine an electrode-to-nerve distance of $5\,mm$ with an electrode placement accuracy of $0.1\,mm$.

Mesh Number 1 was used as a benchmark to compare the accuracy of the coarser meshes. Figure A-4 shows the average percent difference for potentials interpolated at 5 locations within the nerve (Figure 3-10) with respect to Mesh Number 1. Overall, the magnitude of the difference for all mesh cases was fairly small, less than 1%. However, Mesh Numbers 5 and 6 exhibited a large variation in percent difference across the interpolation paths due to their larger element sizes in the interpolated regions.

Mesh Number 4 was chosen as an adequate compromise between computation time and solution accuracy. The single load step solution solved in roughly 30 seconds in Ansys, nearly 6 times faster than Mesh Number 1, with only a 0.2% loss in accuracy.

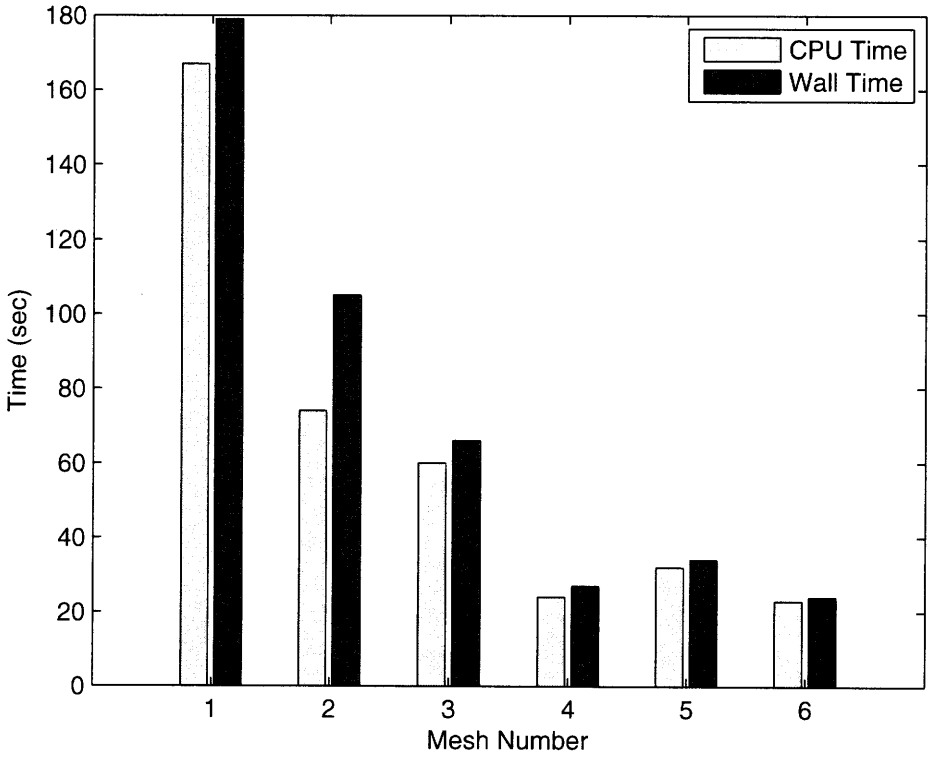

Figure A-3: Run Time versus Mesh Resolution: Shown are CPU and wall times for a single load step (electrode placement) in Ansys. See Table A.2 for a correspondence between Mesh Number and resolution.

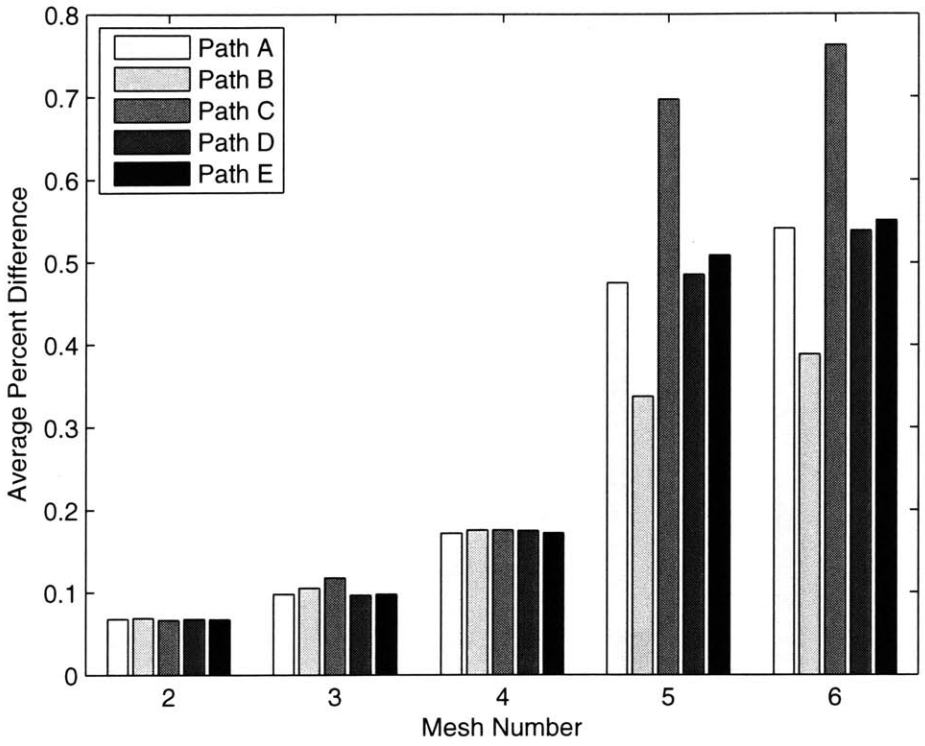

Figure A-4: Average percent difference of potentials interpolated at 5 locations within the nerve with respect to Mesh Number 1.

The potential solution for a typical run of 51 load steps completed in a little over 30 minutes. The threshold analysis of those 51 load steps also took roughly 30 minutes to compute in NEURON. Therefore, the current-distance analysis for an electrode configuration took approximately an hour to complete.

Appendix B

Schwarz-Eikhof-Frijns (SEF) Model

The description of the SEF model presented in this Appendix is based upon the work of Frijns and Schwarz-Eikhoff to quantify neural activity in the myelinated nerves of mammals exposed to extracellular stimuli. The description of the equations and model parameters were taken from their respective publications [60, 61].

B.1 Equations

The nodal conductances and membrane capacitance are calculated using fiber geometry as

$$G_a = \frac{\pi D^2}{4\rho_a L} \tag{B.1}$$

$$C_m = c_m \pi dl \tag{B.2}$$

$$G_L = g_L \pi dl \tag{B.3}$$

The resting membrane potential is calculated using the Goldman Equation [60]

$$V_r = \frac{RT}{F} ln \left(\frac{P_K n_0^2 [c^o_{K+}] + P_{Na} h_0 m_0^3 [c^o_{Na+}]}{P_K n_0^2 [c^i_{K+}] + P_{Na} h_0 m_0^3 [c^i_{Na+}]} \right) \tag{B.4}$$

where m_0, h_0, n_0 are the steady-state values of the (in)activation factors. The sodium inactivation factor and potassium activation factor follow first-order differential equa-

tions

$$\frac{dh_{(n)}}{dt} = \alpha_{h_{(n)}} - (\alpha_{h_{(n)}} + \beta_{h_{(n)}})h_{(n)} \tag{B.5}$$

$$\frac{dn_{(n)}}{dt} = \alpha_{n_{(n)}} - (\alpha_{n_{(n)}} + \beta_{n_{(n)}})n_{(n)} \tag{B.6}$$

The voltage and temperature dependent rate constants, α and β, used to determine the activation factors $m_{(n)}$, $h_{(n)}$, and $n_{(n)}$ are given by:

$$\alpha_{m_{(n)}} = \left[\frac{A_{\alpha m}(V_{(n)} - B_{\alpha m})}{1 - \exp\left(\frac{B_{\alpha m} - V_{(n)}}{C_{\alpha m}}\right)}\right] \cdot Q_{10,\alpha m}^{\left(\frac{T-T_0}{10}\right)} \tag{B.7}$$

$$\alpha_{h_{(n)}} = \left[\frac{A_{\alpha h}(B_{\alpha h} - V_{(n)})}{1 - \exp\left(\frac{V_{(n)} - B_{\alpha h}}{C_{\alpha h}}\right)}\right] \cdot Q_{10,\alpha h}^{\left(\frac{T-T_0}{10}\right)} \tag{B.8}$$

$$\alpha_{n_{(n)}} = \left[\frac{A_{\alpha n}(V_{(n)} - B_{\alpha n})}{1 - \exp\left(\frac{B_{\alpha n} - V_{(n)}}{C_{\alpha n}}\right)}\right] \cdot Q_{10,\alpha n}^{\left(\frac{T-T_0}{10}\right)} \tag{B.9}$$

$$\beta_{m_{(n)}} = \left[\frac{A_{\beta m}(B_{\beta m} - V_{(n)})}{1 - \exp\left(\frac{V_{(n)} - B_{\beta m}}{C_{\beta m}}\right)}\right] \cdot Q_{10,\beta m}^{\left(\frac{T-T_0}{10}\right)} \tag{B.10}$$

$$\beta_{h_{(n)}} = \left[\frac{A_{\beta h}}{1 + \exp\left(\frac{B_{\beta h} - V_{(n)}}{C_{\beta h}}\right)}\right] \cdot Q_{10,\beta h}^{\left(\frac{T-T_0}{10}\right)} \tag{B.11}$$

$$\beta_{n_{(n)}} = \left[\frac{A_{\beta n}(B_{\beta n} - V_{(n)})}{1 - \exp\left(\frac{V_{(n)} - B_{\beta n}}{C_{\beta n}}\right)}\right] \cdot Q_{10,\beta n}^{\left(\frac{T-T_0}{10}\right)} \tag{B.12}$$

B.2 Parameters

Symbol	Parameter	Value	Units
$V_{i_{(n)}}$	Intracellular Potential		V
$V_{e_{(n)}}$	Extracellular Potential		V
$V_{m_{(n)}}$	Deviation of Membrane Potential from Rest		V
V_r	Resting Membrane Potential	-0.0846	V
V_L	Leakage Reversal Potential		V
D	Fiber Diameter	1–10	μm
d	Axon Diameter	$0.7D$	μm
l	Node of Ranvier Length	2.5	μm
L	Internodal Distance	$100D$	μm
ρ_a	Axoplasmic Resistivity	0.70	Ωm
c_m	Unit Area Membrane Capacitance	0.02	$\frac{F}{m^2}$
g_L	Unit Area Leak Conductance	728	$\frac{S}{m^2}$
G_a	Axoplasmic Conductance	$\frac{\pi D^2}{4\rho_a L}$	S
C_m	Membrane Capacitance	$c_m \pi dl$	F
G_L	Leakage Conductance	$g_L \pi dl$	S
P_{Na}	Sodium Permeability	51.5×10^{-6}	$\frac{m}{s}$
P_K	Potassium Permeability	2.04×10^{-6}	$\frac{m}{s}$
T	Absolute Body Temperature	310.15	K
T_0	Absolute Temperature	293.15	K
F	Faraday's Constant	96485	$\frac{C}{mol}$
R	Ideal Gas Constant	8.314	$\frac{J}{Kmol}$
$[c^o_{Na^+}]$	Extracellular Sodium Concentration	142.0	$\frac{mol}{m^3}$
$[c^i_{Na^+}]$	Intracellular Sodium Concentration	10.0	$\frac{mol}{m^3}$
$[c^o_{K^+}]$	Extracellular Potassium Concentration	4.2	$\frac{mol}{m^3}$
$[c^i_{K^+}]$	Intracellular Potassium Concentration	141.0	$\frac{mol}{m^3}$
m_0	Steady-state Sodium Activation Factor	0.0077	·
h_0	Steady-state Sodium Inactivation Factor	0.76	·
n_0	Steady-state Potassium Activation Factor	0.0267	·

Symbol	Parameter	Value	Units
$Q_{10,\alpha m}$	Temperature Correction Factor	2.2	·
$Q_{10,\beta m}$	Temperature Correction Factor	2.2	·
$Q_{10,\alpha h}$	Temperature Correction Factor	2.9	·
$Q_{10,\beta h}$	Temperature Correction Factor	2.9	·
$Q_{10,\alpha n}$	Temperature Correction Factor	3.0	·
$Q_{10,\beta n}$	Temperature Correction Factor	3.0	·
$A_{\alpha m}$	α_m Constant	0.49	·
$B_{\alpha m}$	α_m Constant	25.41	·
$C_{\alpha m}$	α_m Constant	6.06	·
$A_{\beta m}$	β_m Constant	1.04	·
$B_{\beta m}$	β_m Constant	21.00	·
$C_{\beta m}$	β_m Constant	9.41	·
$A_{\alpha h}$	α_h Constant	0.09	·
$B_{\alpha h}$	α_h Constant	-27.74	·
$C_{\alpha h}$	α_h Constant	9.06	·
$A_{\beta h}$	β_h Constant	3.70	·
$B_{\beta h}$	β_h Constant	56.00	·
$C_{\beta h}$	β_h Constant	12.50	·
$A_{\alpha n}$	α_n Constant	0.02	·
$B_{\alpha n}$	α_n Constant	35.00	·
$C_{\alpha n}$	α_n Constant	10.00	·
$A_{\beta n}$	β_n Constant	0.05	·
$B_{\beta n}$	β_n Constant	10.00	·
$C_{\beta n}$	β_n Constant	10.00	·

Table B.1: SEF Model Parameters

B.3 Characteristics

The interested reader may wish to compare the SEF model to other well-established biophysical models such as the Hodgkin-Huxley model derived from the giant squid axon [65], the Frankenhaeuser-Huxley model derived from a myelinated Xenopus Laevis nerve [66], or the Chiu model derived from a myelinated rabbit nerve [67]. No direct comparison is made in this work, however the reader is invited to consult the following references [26, 37, 39, 59, 58, 63, 68, 69, 70]. The following sections detail so-called standard model data at 37° C under space(voltage)-clamp.

B.3.1 Activation Factor Kinetics

A form of the first-order kinetic equations governing the activation factors we have already seen is

$$\begin{aligned} \frac{dx_{(n)}}{dt} &= \alpha_{x_{(n)}}(1 - x_{(n)}) - \beta_{x_{(n)}} x_{(n)} \\ &= \alpha_{x_{(n)}} - (\alpha_{x_{(n)}} + \beta_{x_{(n)}}) x_{(n)} \end{aligned} \tag{B.13}$$

where $x_{(n)}$ can be replaced by $m_{(n)}$, $h_{(n)}$, or $n_{(n)}$. Another form in terms of a time constant and a final value (dropping the node index), is

$$\tau_x \frac{dx}{dt} + x = x_\infty \tag{B.14}$$

where α_x, β_x, τ_x, and x_∞ are functions of membrane potential (V_m) and temperature. By constraining the temperature to 37° C, the variables are only a function of membrane potential. The time constant and final value of x in Equation B.14 have the form

$$x_\infty = \frac{\alpha_x}{\alpha_x + \beta_x} \tag{B.15}$$

$$\tau_x = \frac{1}{\alpha_x + \beta_x} \tag{B.16}$$

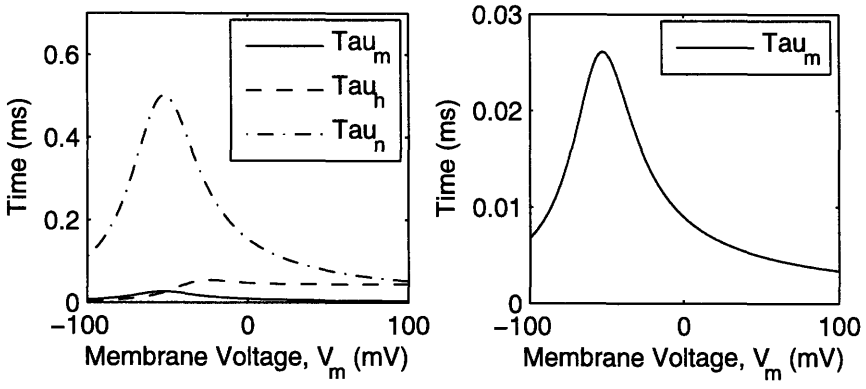

Figure B-1: Activation Factor Time Constants versus Membrane Voltage (V_m): τ_m is shown on a separate scale on the right since it is smaller than τ_n or τ_h.

Figures B-1 and B-2 show the time constants and the steady-state values for the activation factors plotted against membrane voltage V_m.

B.3.2 Strength-Duration Curve

Figure B-3 shows the strength-duration behavior of the SEF model. The calculated results are derived from the equation

$$I = I_{rh} \cdot \left(1 + \frac{\tau_{chr}}{t_{pulse}}\right) \tag{B.17}$$

where I_{rh} is the reobase current, τ_{chr} is the chronaxie time, and t_{pulse} is the pulse width. The reobase current is the minimum threshold required to initiate an action potential and the chronaxie time is the pulse width at exactly twice the reobase value. For the SEF model, the reobase current is $1.388\,nA$ and the chronaxie time is $62\,\mu s$.

B.3.3 Action Potential

Figure B-4 shows the response of the membrane potential, state variables, and transmembrane currents to a suprathreshold current applied to a space-clamped node.

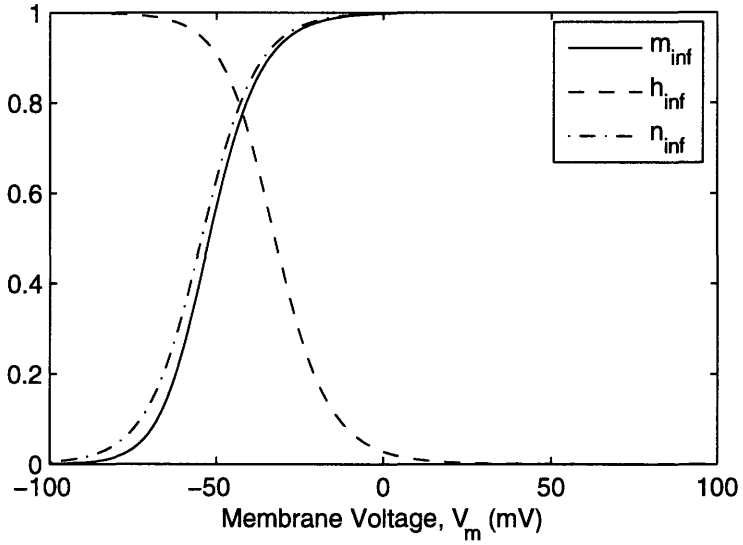

Figure B-2: Steady-State Values versus Membrane Voltage (V_m)

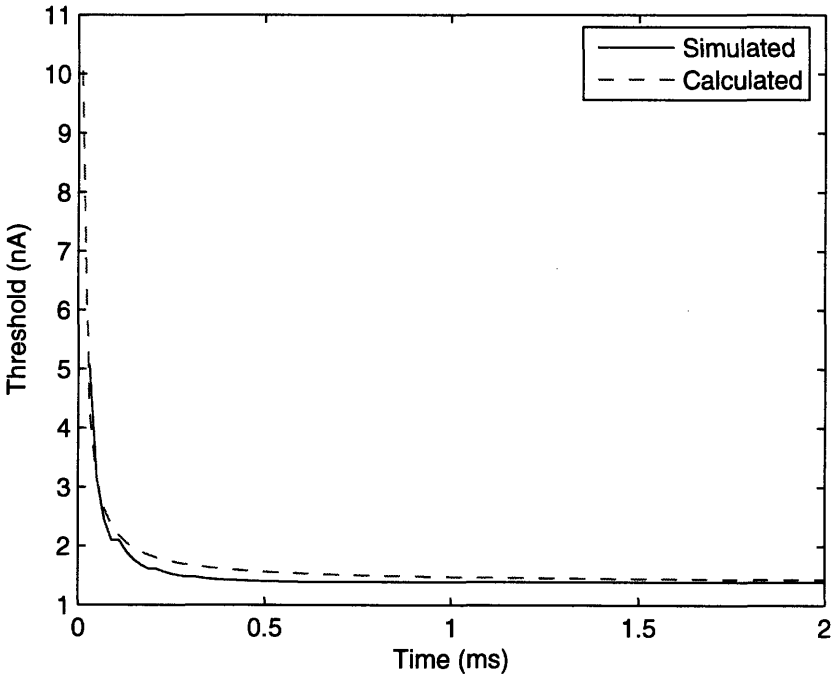

Figure B-3: SEF Strength-Duration Curve: Shown are the simulated and theoretically calculated results. The reobase current value is $1.388\,nA$ and the chronaxie time is $62\,\mu s$.

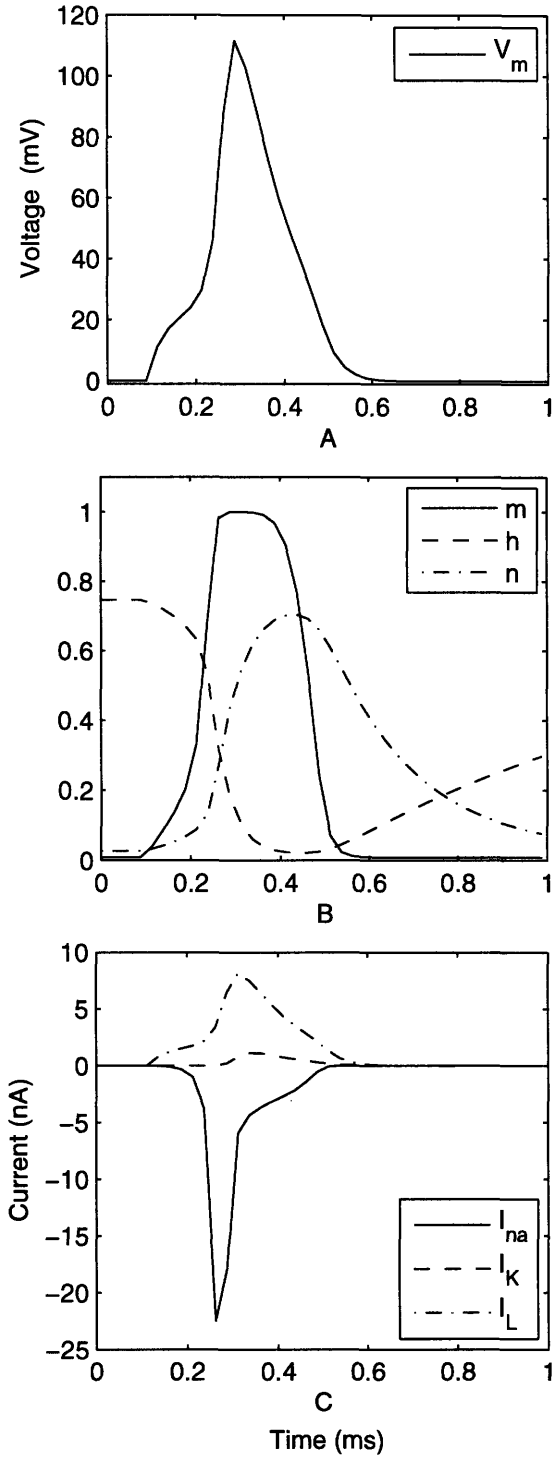

Figure B-4: Dynamics of SEF Action Potential (AP) showing membrane potential, state variables, and transmembrane currents: **A**, Deviation of membrane potential from rest. Note that the AP does not exhibit hyperpolarization; **B**, Sodium activation (m) and inactivation (h) factors and potassium activation (n) factor; **C**, Transmembrane currents (I_{Na}, sodium current; I_K, potassium current; I_L, leakage current)

Appendix C

Supplemental Results

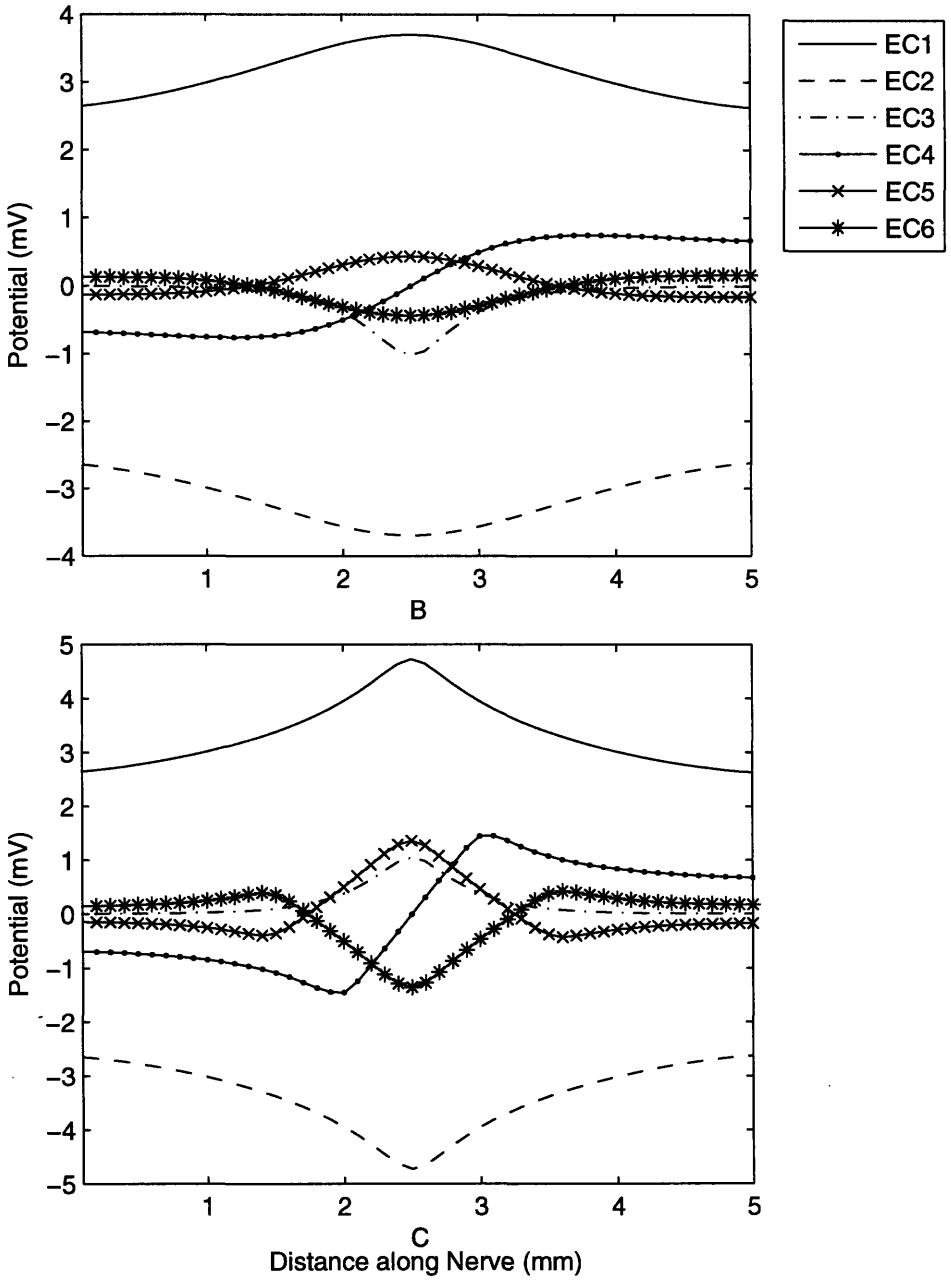

Figure C-1: Potential Field along Paths **B** and **C** for Six Electrode Configurations located $0.1\,mm$ from the IVN. **EC1**: Electrode Configuration 1, **EC2**: Electrode Configuration 2, *etc.* Note: Increasing distance along the nerve corresponds to more distal locations.

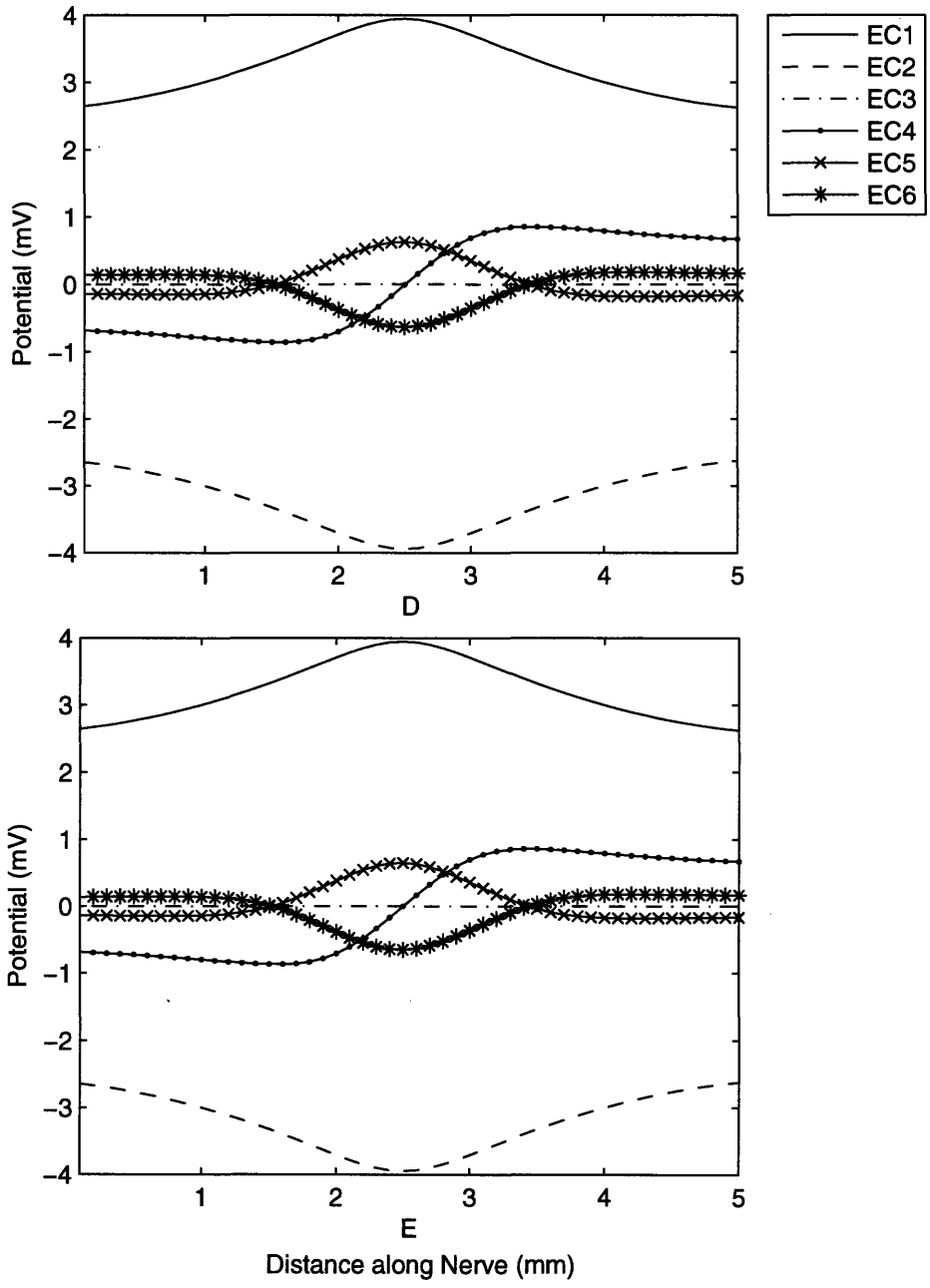

Figure C-2: Potential Field along Paths **D** and **E** for Six Electrode Configurations located 0.1 *mm* from the IVN. The potential distribution is exactly the same for paths **D** and **E**, as expected.

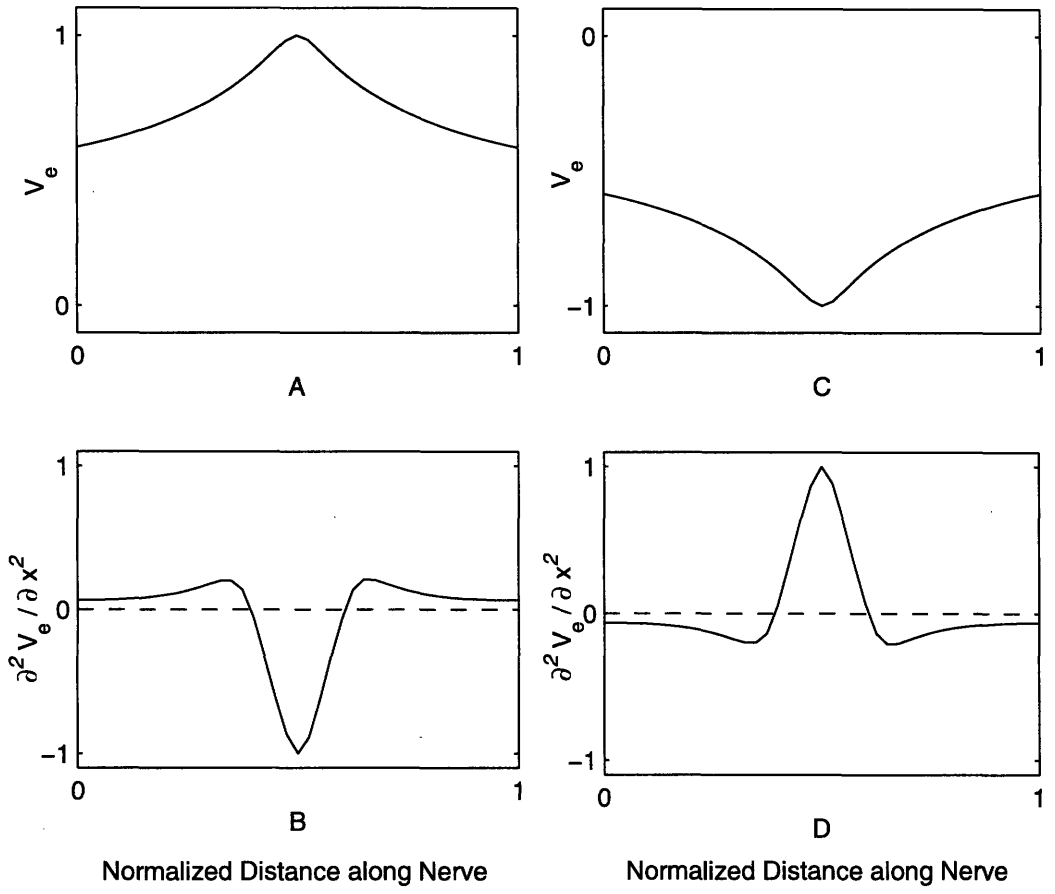

Figure C-3: Potential (**A**) and activating function (**B**) for a monopolar anode; Potential (**C**) and activating function (**D**) for a monopolar cathode; Note: All plots are normalized.

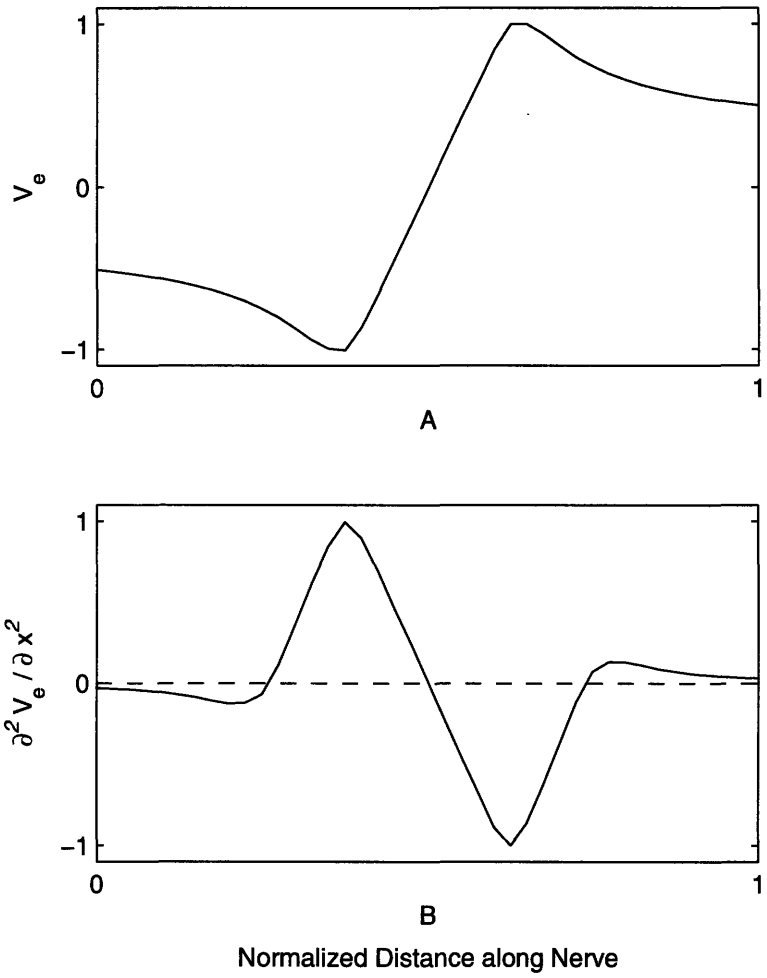

Figure C-4: Potential (**A**) and activating function (**B**) for a transverse dipole; Note: All plots are normalized.

$D = 1\,\mu m$

	0.1 mm	0.2 mm	0.5 mm	1 mm	2 mm	5 mm
EC 1	1099.58	1224.38	1638.09	2551.11	5817.68	39364.41
EC 2	197.35	370.92	1220.89	4035.21	17169.01	171621.00
EC 3	242.82	463.83	1996.85	9767.48	Inf	Inf
EC 4	174.07	314.49	1062.06	4310.26	Inf	Inf
EC 5	339.80	594.72	2175.29	10469.61	Inf	Inf
EC 6	187.07	321.05	1075.43	4560.85	Inf	Inf

$D = 5\,\mu m$

	0.1 mm	0.2 mm	0.5 mm	1 mm	2 mm	5 mm
EC 1	139.43	163.75	246.73	439.82	1165.23	9143.25
EC 2	52.64	75.91	165.96	404.64	1384.64	12269.80
EC 3	80.33	128.51	371.95	1270.20	6325.33	Inf
EC 4	53.10	85.73	180.64	494.35	1878.92	9769.97
EC 5	105.23	167.48	516.78	1453.05	4629.38	Inf
EC 6	50.79	75.69	190.92	623.85	3510.18	Inf

$D = 10\,\mu m$

	0.1 mm	0.2 mm	0.5 mm	1 mm	2 mm	5 mm
EC 1	95.77	111.85	170.42	312.25	855.55	7099.27
EC 2	63.79	78.20	174.90	294.57	943.20	8013.33
EC 3	151.09	192.27	391.09	1501.53	4567.57	Inf
EC 4	51.19	63.20	113.57	286.10	830.79	4398.00
EC 5	150.12	202.99	449.46	1015.51	3340.89	Inf
EC 6	75.44	96.59	192.33	685.40	2502.96	Inf

Table C.1: IVN Threshold Values for $D = 1, 5, 10\,\mu m$ at Various Distances: Threshold values expressed in microamps (μA); Values of "Inf" indicate the inability to initiate nerve firing.

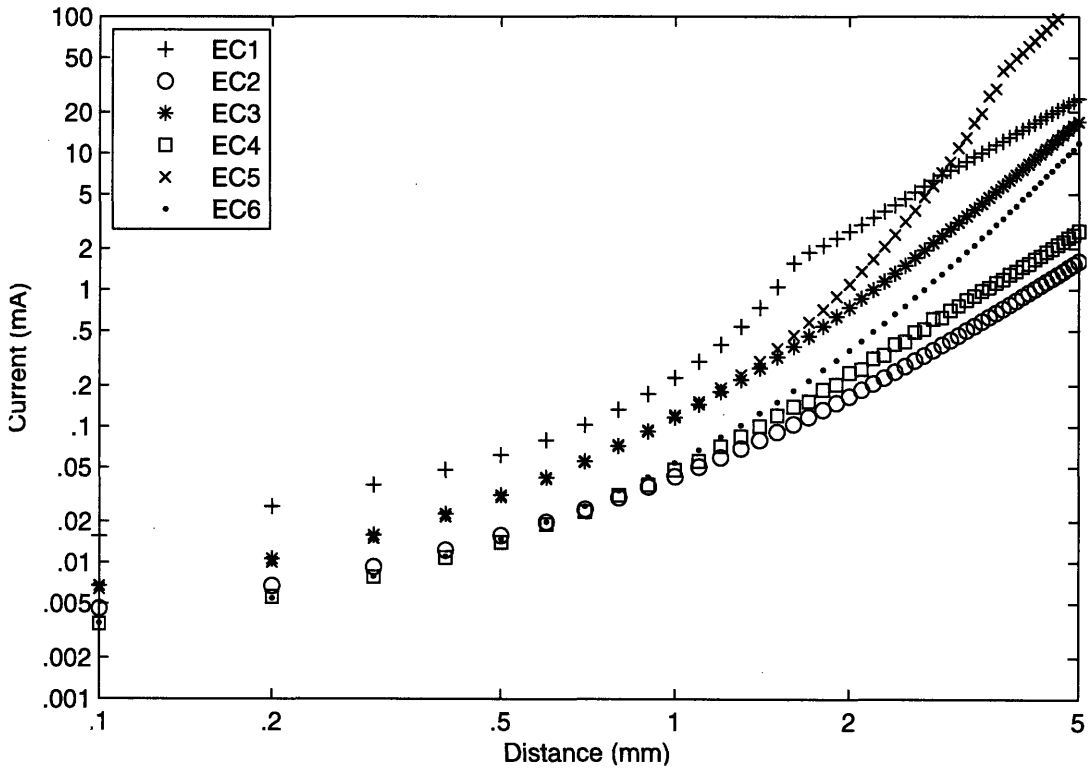

Figure C-5: Minimum IVN Current-Distance Relations (Activating Function): **A**, Electrode Configuration 1; **B**, Electrode Configuration 2; **C**, Electrode Configuration 3

THIS PAGE INTENTIONALLY LEFT BLANK

Bibliography

[1] V. J. Wilson and G. M. Jones. *Mammalian Vestibular Physiology.* Plenum Press, New York, 1979.

[2] C. Wall, III, D.M. Merfeld, S.D. Rauch, and F.O. Black. Vestibular prostheses: The engineering and biomedical issues. *J Vestib Res*, 12(2-3):95 – 113, 2003.

[3] National Institutes of Health. National Strategic Research Plan, DC-134. *Balance and Balance Disorders*, pages 77–110, 1995.

[4] C. Wall, III and M.S. Weinberg. Balance prostheses for postural control. *IEEE Eng Med Biol Mag*, 22(2):84, 2003.

[5] C. Wall, III, M.S. Weinberg, P.B. Schmidt, and D.E. Krebs. Balance prosthesis based on micromechanical sensors using vibrotactile feedback of tilt. *IEEE Trans Biomed Eng*, 48(10):1153, 2001.

[6] P.P. Kadkade, B.J. Benda, P.B. Schmidt, and C. Wall, III. Vibrotactile display codng for a balance prosthesis. *IEEE Trans Neural Syst Rehabil Eng*, 11(4):392, 2003.

[7] C. Wall, III and E. Kentala. Control of sway using vibrotactile feedback of body tilt in patients with moderate and severe postural control deficits. *J Vestib Res*, 15(5-6):313–325, 2005.

[8] W. Gong and D. M. Merfeld. Prototype neural semicircular canal prosthesis using patterned electrical stimulation. *Ann Biomed Eng*, 28(5):572–581, 2000.

[9] W. Gong and D. M. Merfeld. System design and performance of a unilateral horizontal semicircular canal prosthesis. *IEEE Trans Biomed Eng*, 49(2):175–181, 2002.

[10] R. F. Lewis, W. Gong, M. Ramsey, L. Minor, R. Boyle, and D. M. Merfeld. Vestibular adaptation studied with a prosthetic semicircular canal. *J Vestib Res*, 12(2-3):87–94, 2002.

[11] A. M. Shkel, J. Liu, C. Ikei, and Z. Fan-Gang. Feasibility study on a prototype of vestibular implant using MEMS gyroscopes. In *IEEE Sensors*, pages 1526–1531, Orlando, Fl, 2002.

[12] J. Liu, A. M. Shkel, K. Niel, and Z. Fan-Gang. System design and experimental evaluation of a MEMS-based semicircular canal prosthesis. In *Proceedings of the 1st International IEEE EMBS Conference on Neural Engineering*, pages 177–180, Capri Island, Italy, 2003.

[13] J. Liu and A. M. Shkel. An electronic prosthesis mimicking the dynamic vestibular function. In *IEEE Sensors Conference*, volume 2, pages 996–1001, 2003.

[14] J.P. Kelly. Vestibular system. In *Principles of Neural Science*. E.R. Kandel and J.H. Schwartz, editors, Elsevier, New York, 1st edition, 1981.

[15] P. Roland and J. Rutka. Physiology of the vestibular system. In *Ototoxicity*. BC Decker, 2004.

[16] M.J.T. FitzGerald and J. Folan-Curran. *Clinical Neuroanatomy and Related Neuroscience*. Saunders, 4th edition, 2001.

[17] R. P. Schefter and S. G. Harner. Histologic study of the vestibulocochlear nerve. *Ann Otol Rhinol Laryngol*, 95(2 Pt 1):146–50, 1986.

[18] H. Engstrom and B. Engstrom. The structure of the vestibular sensory epithelia. In *The Vestibular system: function and morphology*. T. Gualtierotti, editor, Springer-Verlag, New York, 1981.

[19] I. Lopez, G. Ishiyama, Y. Tang, M. Frank, R.W. Baloh, and A. Ishiyama. Estimation of the number of nerve fibers in the human vestibular endorgans using unbiased stereology and immunohistochemistry. *J Neurosci Methods*, 145:37–46, 2005.

[20] B. Bergstrom. Morphology of the vestibular nerve. I. Anatomical studies of the vestibular nerve in man. *Acta Otolaryngol*, 76(2):162–72, 1973.

[21] K. Tsuji, S.D. Rauch, C. Wall, III, L. Velazquez-Villasenor, R.J. Glynn, S.N. Merchant. Temporal bone studies of the human peripheral vestibular system: Meniere's disease. *Ann Otol Rhinol Laryngol*, 109:26–31, 2000.

[22] D. R. McNeal. Analysis of a model for excitation of myelinated nerve. *IEEE Trans Biomed Eng*, 23(4):329–337, 1976.

[23] R. Fitzhugh. Computation of impulse initiation and saltatory conduction in a myelinated nerve fiber. *Biophys J*, 2:11–21, 1962.

[24] W.A.H. Rushton. The effect upon the threshold for nervous excitation of the length of nerve exposed, and the angle between current and nerve. *J. Physiol. (London)*, 63:357, 1927.

[25] J.J. Lussier and W.A.H. Rushton. The excitability of a single fiber in a nerve trunk. *J. Physiol. (London)*, 117:87, 1952.

[26] T. F. Weiss. *Cellular Biophysics, Volume 2: Electrical Properties.* MIT Press, Cambridge, MA, 1997.

[27] E. N. Warman, W. M. Grill, and D. Durand. Modeling the effects of electric fields on nerve fibers: Determination of excitation thresholds. *IEEE Trans Biomed Eng*, 39(12):1244–1254, 1992.

[28] J. H. Meier, W. L. Rutten, A. E. Zoutman, H. B. Boom, and P. Bergveld. Simulation of multipolar fiber selective neural stimulation using intrafascicular electrodes. *IEEE Trans Biomed Eng*, 39(2):122–34, 1992.

[29] A. G. Richardson, C. C. McIntyre, and W. M. Grill. Modelling the effects of electric fields on nerve fibres: Influence of the myelin sheath. *Med Biol Eng Comput*, 38(4):438–446, 2000.

[30] R. Plonsey and R. C. Barr. Electric field stimulation of excitable tissue. *IEEE Trans Biom Eng*, 42(4):329–336, 1995.

[31] J.W. Clark and R. Plonsey. A mathematical study of nerve fiber interaction. *Biophys J*, 10:937–957, 1970.

[32] H. Wang and C. Northrop. *3D Model of Human Temporal Bone.* M.C. Liberman and S. Merchant, Eds., 2005.

[33] C. Wall, III. Personal communication. 2006.

[34] J. Malmivuo and R. Plonsey. *Bioelectromagnetism - Principles and Applications of Bioelectric and Biomagnetic Fields.* Oxford University Press, New York, 1995.

[35] R. Plonsey and D.B. Heppner. Considerations of quasi-stationarity in electrophysiological systems. *Bull Math Biophys*, 29:657–664, 1967.

[36] K. W. Altman and R. Plonsey. Development of a model for point-source electrical fiber bundle stimulation. *Med Biol Eng Comput*, 26(5):466–475, 1988.

[37] F. Rattay. Analysis of models for external stimulation of axons. *IEEE Trans Biom Eng*, 33(10):974–977, 1986.

[38] F. Rattay. Modelling and simulation of electrically stimulated nerve and muscle fibers: A review. *Math Comput Simul*, 29:357–366, 1987.

[39] F. Rattay. Analysis of models for extracellular fiber stimulation. *IEEE Trans Biomed Eng*, 36(7):676–682, 1989.

[40] W. M. Grill and J. T. Mortimer. Inversion of the current-distance relationship by transient depolarization. *IEEE Trans Biom Eng*, 44(1):1–9, 1997.

[41] C. C. McIntyre and W. M. Grill. Selective microstimulation of central nervous system neurons. *Ann Biomed Eng*, 28(3):219–233, 2000.

[42] W.M. Grill, Jr. Modeling the effects of electric fields on nerve fibers: Influence of tissue electrical properties. *IEEE Trans Biom Eng*, 46(8):918–928, 1999.

[43] D. F. Stegeman, J. P. C. Deweerd, and E. G. J. Eijkman. Volume conductor study of compound action potentials of nerves insitu - forward problem. *Biol Cybern*, 33(2):97–111, 1979.

[44] P. H. Veltink, J. A. van Alste, and H. B. Boom. Simulation of intrafascicular and extraneural nerve stimulation. *IEEE Trans Biomed Eng*, 35(1):69–75, 1988.

[45] P. H. Veltink, B. K. van Veen, J. J. Struijk, J. Holsheimer, and H. B. Boom. A modeling study of nerve fascicle stimulation. *IEEE Trans Biomed Eng*, 36(7):683–92, 1989.

[46] R. B. Szlavik and H. de Bruin. The effect of stimulus current pulse width on nerve fiber size recruitment patterns. *Med Eng Phys*, 21(6-7):507–515, 1999.

[47] R. B. Szlavik and H. de Bruin. The effect of anisotropy on the potential distribution in biological tissue and its impact on nerve excitation simulations. *IEEE Trans Biom Eng*, 47(9):12021210, 2000.

[48] D. M. Whiten. Threshold predictions based on an electro-anatomical model of the cochlear implant. Master's thesis, Massachusetts Institute of Technology, 2003.

[49] F. Rattay, R. N. Leao, and H. Felix. A model of the electrically excited human cochlear neuron. II. Influence of the three-dimensional cochlear structure on neural excitability. *Hear Res*, 153(1-2):64–79, 2001.

[50] F. Rattay and S. Resatz. Effective electrode configuration for selective stimulation with inner eye prostheses. *IEEE Trans Biom Eng*, 51(9):1659–1664, 2004.

[51] T. Hanekom. Three-dimensional spiraling finite element model of the electrically stimulated cochlea. *Ear And Hearing*, 22(4):300–315, 2001.

[52] A. Q. Choi, J. K. Cavanaugh, and D. M. Durand. Selectivity of multiple-contact nerve cuff electrodes: a simulation analysis. *IEEE Trans Biom Eng*, 48(2):165–172, 2001.

[53] S. Parrini, J. Delbeke, V. Legat, and C. Veraart. Modelling analysis of human optic nerve fibre excitation based on experimental data. *Med Biol Eng Comput*, 38(4):454–464, 2000.

[54] R. J. Greenberg, T. J. Velte, M. S. Humayun, G. N. Scarlatis, and Jr. De Juan, E. A computational model of electrical stimulation of the retinal ganglion cell. *IEEE Trans Biom Eng*, 46(5):505–514, 1999.

[55] A. Vuckovic, N. J. M. Rijkhoff, and J. J. Struijk. Different pulse shapes to obtain small fiber selective activation by anodal blocking–a simulation study. *IEEE Trans Biom Eng*, 51(5):698–706, 2004.

[56] L.A. Geddes and L.E. Baker. The specific resistance of biological materials–a compendium of data for the biomedical engineer and physiologist. *Med Biol Eng*, 5(3):271–93, 1967.

[57] J.A. Kong. *Electromagnetic Wave Theory.* EMW Press, 6th edition, 2005.

[58] R. Plonsey and R. C. Barr. *Bioelectricity: A Quantitative Approach.* Plenum Press, New York, New York, 2nd edition, 2000.

[59] F. Rattay. *Electrical Nerve Stimulation: Theory, Experiments and Applications.* Springer-Verlag, New York, 1990.

[60] J. H. Frijns, J. Mooij, and J. H. ten Kate. A quantitative approach to modeling mammalian myelinated nerve fibers for electrical prosthesis design. *IEEE Trans Biomed Eng*, 41(6):556–66, 1994.

[61] J. R. Schwarz and G. Eikhof. Na Currents And Action-Potentials In Rat Myelinated Nerve-Fibers At 20 Degrees C and 37 Degrees C. *Pflugers Arch*, 409(6):569–577, 1987.

[62] M.L. Hines and N.T. Carnevale. The neuron simulation environment. In *The Handbook of Brain Theory and Neural Networks*, pages 769–773. MIT Press, Cambridge, MA, 2nd edition, 2003.

[63] W.F. Agnew and D.B. McCreary, editors. *Neural Prostheses: Fundamental Studies.* Prentice Hall Biophysics and Bioengineering Series. Prentice-Hall, Englewood Cliffs, 1990.

[64] C. Wall, III, J.P. Guyot, and I. Kos. Eye movements in response to electric stimulation of the human ampullary nerve. *Manuscript submitted for publication*, 2006.

[65] A.L. Hodgkin and A. F. Huxley. A quantitative description of membrane current and its application to conduction and excitation in nerve. *J Physiol*, 117:500–544, 1952.

[66] B. Frankenhaeuser and A. F. Huxley. The action potential in the myelinated nerve of xenopus laevis as computed on the basis of voltage clamp data. *J Physiol*, 171:302–315, 1964.

[67] S. Y. Chiu, J. M. Ritchie, R. B. Rogart, and D. Stagg. Quantitative description of membrane currents in rabbit myelinated nerve. *J Physiol*, 292:149–166, 1979.

[68] J. B. Ranck. Which elements are excited in electrical stimulation of mammalian central nervous system - review. *Brain Res*, 98:417–440, 1975.

[69] B. Coburn. Neural modeling in electrical-stimulation. *Crit Rev Biomed Eng*, 17(2):133–178, 1989.

[70] B. J. Roth. Mechanisms for electrical stimulation of excitable tissue. *Crit Rev Biomed Eng*, 22(3/4):253–305, 1994.